

1 **CONSTRAINTS ON THE GALACTIC POPULATION OF TEV**  
 2 **PULSAR WIND NEBULAE USING *Fermi* LARGE AREA**  
 3 **TELESCOPE OBSERVATIONS**

4 F. Acero<sup>1</sup>, M. Ackermann<sup>2</sup>, M. Ajello<sup>3</sup>, A. Allafort<sup>4</sup>, L. Baldini<sup>5</sup>, J. Ballet<sup>6</sup>,  
 5 G. Barbiellini<sup>7,8</sup>, D. Bastieri<sup>9,10</sup>, K. Bechtol<sup>4</sup>, R. Bellazzini<sup>11</sup>, R. D. Blandford<sup>4</sup>,  
 6 E. D. Bloom<sup>4</sup>, E. Bonamente<sup>12,13</sup>, E. Bottacini<sup>4</sup>, T. J. Brandt<sup>1</sup>, J. Bregeon<sup>11</sup>,  
 7 M. Brigida<sup>14,15</sup>, P. Bruel<sup>16</sup>, R. Buehler<sup>4</sup>, S. Buson<sup>9,10</sup>, G. A. Caliandro<sup>17</sup>, R. A. Cameron<sup>4</sup>,  
 8 P. A. Caraveo<sup>18</sup>, C. Cecchi<sup>12,13</sup>, E. Charles<sup>4</sup>, R.C.G. Chaves<sup>6</sup>, A. Chekhtman<sup>19</sup>, J. Chiang<sup>4</sup>,  
 9 G. Chiaro<sup>10</sup>, S. Ciprini<sup>20,21</sup>, R. Claus<sup>4</sup>, J. Cohen-Tanugi<sup>22</sup>, J. Conrad<sup>23,24,25,26</sup>, S. Cutini<sup>20,21</sup>,  
 10 M. Dalton<sup>27,43</sup>, F. D'Ammando<sup>28</sup>, F. de Palma<sup>14,15</sup>, C. D. Dermer<sup>29</sup>, L. Di Venere<sup>4</sup>,  
 11 E. do Couto e Silva<sup>4</sup>, P. S. Drell<sup>4</sup>, A. Drlica-Wagner<sup>4</sup>, L. Falletti<sup>22</sup>, C. Favuzzi<sup>14,15</sup>,  
 12 S. J. Fegan<sup>16</sup>, E. C. Ferrara<sup>1</sup>, W. B. Focke<sup>4</sup>, A. Franckowiak<sup>4</sup>, Y. Fukazawa<sup>30</sup>, S. Funk<sup>4,31</sup>,  
 13 P. Fusco<sup>14,15</sup>, F. Gargano<sup>15</sup>, D. Gasparri<sup>20,21</sup>, N. Giglietto<sup>14,15</sup>, F. Giordano<sup>14,15</sup>,  
 14 M. Giroletti<sup>28</sup>, T. Glanzman<sup>4</sup>, G. Godfrey<sup>4</sup>, T. Grégoire<sup>32,33</sup>, I. A. Grenier<sup>6</sup>,  
 15 M.-H. Grondin<sup>32,33</sup>, J. E. Grove<sup>29</sup>, S. Guiriec<sup>1</sup>, D. Hadasch<sup>17</sup>, Y. Hanabata<sup>30</sup>,  
 16 A. K. Harding<sup>1</sup>, M. Hayashida<sup>4,34</sup>, K. Hayashi<sup>30</sup>, E. Hays<sup>1</sup>, J. Hewitt<sup>1</sup>, A. B. Hill<sup>4,35,36</sup>,  
 17 D. Horan<sup>16</sup>, X. Hou<sup>27</sup>, R. E. Hughes<sup>37</sup>, Y. Inoue<sup>4</sup>, M. S. Jackson<sup>38,24</sup>, T. Jogler<sup>4</sup>,  
 18 G. Jóhannesson<sup>39</sup>, A. S. Johnson<sup>4</sup>, T. Kamae<sup>4</sup>, T. Kawano<sup>30</sup>, M. Kerr<sup>4</sup>, J. Knödseder<sup>32,33</sup>,  
 19 M. Kuss<sup>11</sup>, J. Lande<sup>4,40</sup>, S. Larsson<sup>23,24,41</sup>, L. Latronico<sup>42</sup>, M. Lemoine-Goumard<sup>27,43,44</sup>,  
 20 F. Longo<sup>7,8</sup>, F. Loparco<sup>14,15</sup>, M. N. Lovellette<sup>29</sup>, P. Lubrano<sup>12,13</sup>, M. Marelli<sup>18</sup>, F. Massaro<sup>4</sup>,  
 21 M. Mayer<sup>2</sup>, M. N. Mazziotta<sup>15</sup>, J. E. McEnery<sup>1,45</sup>, J. Mehault<sup>27,43</sup>, P. F. Michelson<sup>4</sup>,  
 22 W. Mitthumsiri<sup>4</sup>, T. Mizuno<sup>46</sup>, C. Monte<sup>14,15</sup>, M. E. Monzani<sup>4</sup>, A. Morselli<sup>47</sup>,  
 23 I. V. Moskalenko<sup>4</sup>, S. Murgia<sup>4</sup>, T. Nakamori<sup>48</sup>, R. Nemmen<sup>1</sup>, E. Nuss<sup>22</sup>, T. Ohsugi<sup>46</sup>,  
 24 A. Okumura<sup>4,49</sup>, M. Orienti<sup>28</sup>, E. Orlando<sup>4</sup>, J. F. Ormes<sup>50</sup>, D. Paneque<sup>51,4</sup>, J. H. Panetta<sup>4</sup>,  
 25 J. S. Perkins<sup>1,52,53,54</sup>, M. Pesce-Rollins<sup>11</sup>, F. Piron<sup>22</sup>, G. Pivato<sup>10</sup>, T. A. Porter<sup>4,4</sup>,  
 26 S. Rainò<sup>14,15</sup>, R. Rando<sup>9,10</sup>, M. Razzano<sup>11,55</sup>, A. Reimer<sup>56,4</sup>, O. Reimer<sup>56,4</sup>, T. Reposeur<sup>27</sup>,  
 27 S. Ritz<sup>55</sup>, M. Roth<sup>57</sup>, R. Rousseau<sup>27,43,58</sup>, P. M. Saz Parkinson<sup>55</sup>, A. Schulz<sup>2</sup>, C. Sgrò<sup>11</sup>,  
 28 E. J. Siskind<sup>59</sup>, D. A. Smith<sup>27</sup>, G. Spandre<sup>11</sup>, P. Spinelli<sup>14,15</sup>, D. J. Suson<sup>60</sup>, H. Takahashi<sup>30</sup>,  
 29 Y. Takeuchi<sup>48</sup>, J. G. Thayer<sup>4</sup>, J. B. Thayer<sup>4</sup>, D. J. Thompson<sup>1</sup>, L. Tibaldo<sup>4</sup>, O. Tibolla<sup>61</sup>,  
 30 M. Tinivella<sup>11</sup>, D. F. Torres<sup>17,62</sup>, G. Tosti<sup>12,13</sup>, E. Troja<sup>1,63</sup>, Y. Uchiyama<sup>4</sup>,  
 31 J. Vandenbroucke<sup>4</sup>, V. Vasileiou<sup>22</sup>, G. Vianello<sup>4,64</sup>, V. Vitale<sup>47,65</sup>, M. Werner<sup>56</sup>,  
 32 B. L. Winer<sup>37</sup>, K. S. Wood<sup>29</sup>, Z. Yang<sup>23,24</sup>

---

<sup>1</sup>NASA Goddard Space Flight Center, Greenbelt, MD 20771, USA

<sup>2</sup>Deutsches Elektronen Synchrotron DESY, D-15738 Zeuthen, Germany

<sup>3</sup>Space Sciences Laboratory, 7 Gauss Way, University of California, Berkeley, CA 94720-7450, USA, ,  
USA

<sup>4</sup>W. W. Hansen Experimental Physics Laboratory, Kavli Institute for Particle Astrophysics and Cosmology, Department of Physics and SLAC National Accelerator Laboratory, Stanford University, Stanford, CA 94305, USA

<sup>5</sup>Università di Pisa and Istituto Nazionale di Fisica Nucleare, Sezione di Pisa I-56127 Pisa, Italy

<sup>6</sup>Laboratoire AIM, CEA-IRFU/CNRS/Université Paris Diderot, Service d’Astrophysique, CEA Saclay, 91191 Gif sur Yvette, France

<sup>7</sup>Istituto Nazionale di Fisica Nucleare, Sezione di Trieste, I-34127 Trieste, Italy

<sup>8</sup>Dipartimento di Fisica, Università di Trieste, I-34127 Trieste, Italy

<sup>9</sup>Istituto Nazionale di Fisica Nucleare, Sezione di Padova, I-35131 Padova, Italy

<sup>10</sup>Dipartimento di Fisica e Astronomia ”G. Galilei”, Università di Padova, I-35131 Padova, Italy

<sup>11</sup>Istituto Nazionale di Fisica Nucleare, Sezione di Pisa, I-56127 Pisa, Italy

<sup>12</sup>Istituto Nazionale di Fisica Nucleare, Sezione di Perugia, I-06123 Perugia, Italy

<sup>13</sup>Dipartimento di Fisica, Università degli Studi di Perugia, I-06123 Perugia, Italy

<sup>14</sup>Dipartimento di Fisica “M. Merlin” dell’Università e del Politecnico di Bari, I-70126 Bari, Italy

<sup>15</sup>Istituto Nazionale di Fisica Nucleare, Sezione di Bari, 70126 Bari, Italy

<sup>16</sup>Laboratoire Leprince-Ringuet, École polytechnique, CNRS/IN2P3, Palaiseau, France

<sup>17</sup>Institut de Ciències de l’Espai (IEEE-CSIC), Campus UAB, 08193 Barcelona, Spain

<sup>18</sup>INAF-Istituto di Astrofisica Spaziale e Fisica Cosmica, I-20133 Milano, Italy

<sup>19</sup>Center for Earth Observing and Space Research, College of Science, George Mason University, Fairfax, VA 22030, resident at Naval Research Laboratory, Washington, DC 20375, USA

<sup>20</sup>Agenzia Spaziale Italiana (ASI) Science Data Center, I-00044 Frascati (Roma), Italy

<sup>21</sup>Istituto Nazionale di Astrofisica - Osservatorio Astronomico di Roma, I-00040 Monte Porzio Catone (Roma), Italy

<sup>22</sup>Laboratoire Univers et Particules de Montpellier, Université Montpellier 2, CNRS/IN2P3, Montpellier, France

<sup>23</sup>Department of Physics, Stockholm University, AlbaNova, SE-106 91 Stockholm, Sweden

<sup>24</sup>The Oskar Klein Centre for Cosmoparticle Physics, AlbaNova, SE-106 91 Stockholm, Sweden

<sup>25</sup>Royal Swedish Academy of Sciences Research Fellow, funded by a grant from the K. A. Wallenberg

---

Foundation

<sup>26</sup>The Royal Swedish Academy of Sciences, Box 50005, SE-104 05 Stockholm, Sweden

<sup>27</sup>Université Bordeaux 1, CNRS/IN2p3, Centre d'Études Nucléaires de Bordeaux Gradignan, 33175 Gradignan, France

<sup>28</sup>INAF Istituto di Radioastronomia, 40129 Bologna, Italy

<sup>29</sup>Space Science Division, Naval Research Laboratory, Washington, DC 20375-5352, USA

<sup>30</sup>Department of Physical Sciences, Hiroshima University, Higashi-Hiroshima, Hiroshima 739-8526, Japan

<sup>31</sup>email: funk@slac.stanford.edu

<sup>32</sup>CNRS, IRAP, F-31028 Toulouse cedex 4, France

<sup>33</sup>GAHEC, Université de Toulouse, UPS-OMP, IRAP, Toulouse, France

<sup>34</sup>Department of Astronomy, Graduate School of Science, Kyoto University, Sakyo-ku, Kyoto 606-8502, Japan

<sup>35</sup>School of Physics and Astronomy, University of Southampton, Highfield, Southampton, SO17 1BJ, UK

<sup>36</sup>Funded by a Marie Curie IOF, FP7/2007-2013 - Grant agreement no. 275861

<sup>37</sup>Department of Physics, Center for Cosmology and Astro-Particle Physics, The Ohio State University, Columbus, OH 43210, USA

<sup>38</sup>Department of Physics, Royal Institute of Technology (KTH), AlbaNova, SE-106 91 Stockholm, Sweden

<sup>39</sup>Science Institute, University of Iceland, IS-107 Reykjavik, Iceland

<sup>40</sup>email: joshualande@gmail.com

<sup>41</sup>Department of Astronomy, Stockholm University, SE-106 91 Stockholm, Sweden

<sup>42</sup>Istituto Nazionale di Fisica Nucleare, Sezione di Torino, I-10125 Torino, Italy

<sup>43</sup>Funded by contract ERC-StG-259391 from the European Community

<sup>44</sup>email: lemoine@cenbg.in2p3.fr

<sup>45</sup>Department of Physics and Department of Astronomy, University of Maryland, College Park, MD 20742, USA

<sup>46</sup>Hiroshima Astrophysical Science Center, Hiroshima University, Higashi-Hiroshima, Hiroshima 739-8526, Japan

<sup>47</sup>Istituto Nazionale di Fisica Nucleare, Sezione di Roma “Tor Vergata”, I-00133 Roma, Italy

<sup>48</sup>Research Institute for Science and Engineering, Waseda University, 3-4-1, Okubo, Shinjuku, Tokyo 169-8555, Japan

<sup>49</sup>Solar-Terrestrial Environment Laboratory, Nagoya University, Nagoya 464-8601, Japan

<sup>50</sup>Department of Physics and Astronomy, University of Denver, Denver, CO 80208, USA

## ABSTRACT

33

34

Pulsar wind nebulae (PWNe) have been established as the most populous class of TeV  $\gamma$ -ray emitters. Since launch, the *Fermi* Large Area Telescope (LAT) identified five high-energy ( $100 \text{ MeV} < E < 100 \text{ GeV}$ )  $\gamma$ -ray sources as PWNe, and detected a large number of PWNe candidates, all powered by young and energetic pulsars. The wealth of multi-wavelength data available and the new results provided by *Fermi*-LAT give us an opportunity to find new PWNe and to explore the radiative processes taking place in known ones. The TeV  $\gamma$ -ray unidentified sources (UNIDs) are the best candidates for finding new PWNe. Using 45 months of *Fermi*-LAT data for energies above 10 GeV, an analysis was performed near the position of 58 TeV PWNe and UNIDs within  $5^\circ$  of the Galactic Plane to establish new constraints on PWNe properties and find new clues on the nature of UNIDs. Of the 58 sources, 30 were detected, and this work provides their  $\gamma$ -ray fluxes for energies above 10 GeV. The spectral energy distributions (SED) and

---

<sup>51</sup>Max-Planck-Institut für Physik, D-80805 München, Germany

<sup>52</sup>Department of Physics and Center for Space Sciences and Technology, University of Maryland Baltimore County, Baltimore, MD 21250, USA

<sup>53</sup>Center for Research and Exploration in Space Science and Technology (CRESST) and NASA Goddard Space Flight Center, Greenbelt, MD 20771, USA

<sup>54</sup>Harvard-Smithsonian Center for Astrophysics, Cambridge, MA 02138, USA

<sup>55</sup>Santa Cruz Institute for Particle Physics, Department of Physics and Department of Astronomy and Astrophysics, University of California at Santa Cruz, Santa Cruz, CA 95064, USA

<sup>56</sup>Institut für Astro- und Teilchenphysik and Institut für Theoretische Physik, Leopold-Franzens-Universität Innsbruck, A-6020 Innsbruck, Austria

<sup>57</sup>Department of Physics, University of Washington, Seattle, WA 98195-1560, USA

<sup>58</sup>email: rousseau@cenbg.in2p3.fr

<sup>59</sup>NYCB Real-Time Computing Inc., Lattingtown, NY 11560-1025, USA

<sup>60</sup>Department of Chemistry and Physics, Purdue University Calumet, Hammond, IN 46323-2094, USA

<sup>61</sup>Institut für Theoretische Physik and Astrophysik, Universität Würzburg, D-97074 Würzburg, Germany

<sup>62</sup>Institució Catalana de Recerca i Estudis Avançats (ICREA), Barcelona, Spain

<sup>63</sup>NASA Postdoctoral Program Fellow, USA

<sup>64</sup>Consorzio Interuniversitario per la Fisica Spaziale (CIFS), I-10133 Torino, Italy

<sup>65</sup>Dipartimento di Fisica, Università di Roma “Tor Vergata”, I-00133 Roma, Italy

upper limits, in the multi-wavelength context, also provide new information on the source nature and can help distinguish between emission scenarios, i.e. between classification as a pulsar candidate or as a PWN candidate. Six new GeV PWNe candidates are described in detail and compared with existing models. A population study of GeV PWNe candidates as a function of the pulsar/PWN system characteristics is presented.

*Subject headings:* catalogs; gamma rays: general; methods: data analysis

## 1. INTRODUCTION

Since 2003, the extensive observations of the Galactic Plane by Cherenkov telescopes have detected more than 80 Galactic TeV sources (Hinton & Hofmann 2009). Pulsar wind nebulae (PWNe) are the dominant class with more than 30 firm identifications. A similar number of Galactic sources cannot be associated with a counterpart at any other wavelength; they form the unidentified (UNID) source class. The third largest class of Galactic sources are the supernova remnants (SNRs).

The Large Area Telescope (LAT) on board the *Fermi Gamma-ray Space Telescope* provides all-sky coverage of the  $\gamma$ -ray sky at energies from 20 MeV to more than 300 GeV. With 2 years of observations, the *Fermi*-LAT Second Source Catalog (2FGL, Nolan et al. 2012) reports the detection of 1873 sources, 1298 being identified and 575 without clear identification. 400 of them lie within  $5^\circ$  of the Galactic Plane.

Most of the LAT UNID sources are expected to be pulsars, SNRs, binary systems or PWNe. The  $\gamma$ -ray emission from these sources is expected to be either hadronic or leptonic. In the leptonic scenario,  $\gamma$ -ray photons are created by inverse Compton (IC) scattering of highly relativistic leptons from the source on the ambient photon fields such as Cosmic Microwave Background (CMB), stellar radiation or infrared emission from dust (e.g. de Jager et al. 2009; de Jager & Djannati-Ataï 2009). This leptonic approach could well explain several UNIDs (e.g. Tibolla 2011; Tibolla et al. 2012) and, moreover, one of its biggest advantages is that it provides a natural explanation for the UNIDs that lack a lower energy (radio and X-ray) counterpart (e.g. de Jager et al. 2009; H.E.S.S. Collaboration et al. 2012b), i.e. the so-called “dark sources”. In the hadronic scenario, hadrons accelerated by a source collide with the nuclei in the ambient medium (e.g. molecular cloud) and secondary neutral pions decay to  $\gamma$ -rays (e.g. Gabici et al. 2009).

The leptonic PWN scenario requires an energetic and young pulsar to be present. Pulsars are the largest class of Galactic sources detected above 100 MeV with the LAT. These

62 pulsars could make up part of the LAT UNID population. In the LAT energy range, pulsars  
 63 are point-like sources and exhibit power-law spectra with exponential cutoffs between 0.5  
 64 and 6 GeV (Abdo et al. 2010e), while PWNe have hard power-law spectra without cutoffs  
 65 in the GeV energy range and might be spatially resolved by the LAT. Middle-aged SNRs,  
 66 interacting with molecular clouds, detected by the LAT are generally bright and exhibit a  
 67 break at  $\sim 2$  GeV (Uchiyama 2011). Radio, X-ray and  $\gamma$ -ray photons probe the non-thermal  
 68 particle populations and therefore provide information to discriminate between scenarios in  
 69 which the  $\gamma$ -ray emission is dominated by leptonic or hadronic processes.

70 Here we report on the analysis of 58 PWNe and Galactic UNIDs detected at TeV  
 71 energies, using 45 months of *Fermi*-LAT data above 10 GeV. A complementary search for  
 72 PWNe in the off-peak phase ranges of pulsars for which the LAT sees  $\gamma$ -ray pulsations  
 73 (henceforth “LAT-detected pulsars”), updating the analysis of Ackermann et al. (2011), is  
 74 presented in the second *Fermi*-LAT catalog of  $\gamma$ -ray pulsars (Abdo et al. 2013), henceforth  
 75 “2PC”.

76 The objective of this work is to constrain some general characteristics of PWNe such as  
 77 their  $\gamma$ -ray efficiency. This study of TeV sources might also increase the number of PWNe  
 78 candidates detected at GeV energies by the LAT. Slane et al. (2010), Grondin et al. (2011)  
 79 and Rousseau et al. (2012) have demonstrated the potential of LAT observations to study  
 80 PWNe candidates. With the exception of Vela–X (Abdo et al. 2010c), the five PWNe firmly  
 81 identified by *Fermi* are associated with TeV counterparts. Furthermore, their spectra are  
 82 consistent with predictions from a leptonic PWN scenario where the IC spectra peak above  
 83 100 GeV (Abdo et al. 2010b; Grondin et al. 2011).

84 In Section 2, we establish a list of TeV sources potentially associated with PWNe. In  
 85 Section 3, we describe the methods and tools we used to analyze LAT data. In Section 4,  
 86 we describe the spectral and spatial analysis of the LAT data, and in Section 5, we perform  
 87 a population study based on these new  $\gamma$ -ray results.

## 88 2. TEV $\gamma$ -RAY SOURCE SAMPLE

89 We selected our PWNe candidates from the online catalog of TeV  $\gamma$ -ray sources, TeV-  
 90 Cat<sup>1</sup>. As of 2013 January 1, the catalog contained 143 sources observed with the Very High  
 91 Energy (VHE) experiments: H.E.S.S. (Aharonian et al. 2006c), VERITAS (Weekes et al.

---

<sup>1</sup>TeVCat is developed by the University of Chicago and can be obtained from:  
<http://tevcat.uchicago.edu>

92 2002), MAGIC (Aleksić et al. 2012), Milagro (Atkins et al. 2003) and others.

93 Except for N157 B (Komin et al. 2012), all PWNe detected by VHE experiments lie  
94 inside our Galaxy. A survey of the Galactic Plane was performed by H.E.S.S. and the  
95 current version (Gast et al. 2012) covers  $\pm 4^\circ$  in latitude and longitudes between  $l = 65^\circ$   
96 and  $l = 250^\circ$ . Another survey, specific to the Cygnus region, was performed by VERITAS  
97 (Weinstein 2009). Milagro surveyed the Northern hemisphere, covering the Galactic Plane  
98 from  $l = 30^\circ$  to  $l = 220^\circ$  (Abdo et al. 2007). To be conservative compared to the H.E.S.S.  
99 survey, we selected the 84 sources that lie within  $5^\circ$  of the Galactic Plane. The Galactic  
100 center is a complex region to investigate with *Fermi*-LAT, due to the confusion by the large  
101 density of sources and by the diffuse emission, so we removed the three VHE sources within  
102  $2^\circ$  of the Galactic center from our list. These sources, HESS J1745–303 (Aharonian et al.  
103 2008b), HESS J1741–302 (Tibolla et al. 2008) and SNR G0.9+0.1 (Aharonian et al. 2005d),  
104 will be presented separately.

105 We also excluded from our list the 21 TeV  $\gamma$ -ray sources associated with radio-detected  
106 SNRs. LAT observations of these objects will be presented in the *Fermi*-LAT catalog of  
107 SNRs, henceforth “SNR catalog”. Finally, we excluded the Crab Nebula and Vela–X, both  
108 already studied in detail (Abdo et al. 2010b; Buehler et al. 2012; Grondin et al. submitted).  
109 The final list of 58 TeV  $\gamma$ -ray sources that we selected is presented in Table 1 along with  
110 their best-fit morphologies measured by VHE experiments.

Table 1. List of analyzed VHE sources

Name	Class	$l$ (deg)	$b$ (deg)	TeV morphology	$\sigma_1$ (deg)	$\sigma_2$ (deg)	Reference
VER J0006+727	PWN	119.58	10.20	PS	...	...	McArthur (2011)
MGRO J0631+105	PWN	201.30	0.51	PS	...	...	Abdo et al. (2009e)
MGRO J0632+17	PWN	195.34	3.78	G	1.30	...	Abdo et al. (2009e)
HESS J1018–589	UNID	284.23	–1.72	PS	...	...	H.E.S.S. Collaboration et al. (2012a)
HESS J1023–575	MSC	284.22	–0.40	G	0.18	...	H.E.S.S. Collaboration et al. (2011e)
HESS J1026–582	PWN	284.80	–0.52	G	0.14	...	H.E.S.S. Collaboration et al. (2011e)
HESS J1119–614	PWN	292.10	–0.49	G	0.05	...	Presentation <sup>a</sup>
HESS J1303–631	PWN	304.24	–0.36	G	0.16	...	Aharonian et al. (2005c)
HESS J1356–645	PWN	309.81	–2.49	G	0.20	...	H.E.S.S. Collaboration et al. (2011d)
HESS J1418–609	PWN	313.25	0.15	EG	0.08	0.06	Aharonian et al. (2006a)
HESS J1420–607	PWN	313.56	0.27	G	0.06	...	Aharonian et al. (2006a)
HESS J1427–608	UNID	314.41	–0.14	EG	0.04	0.08	Aharonian et al. (2008c)
HESS J1458–608	PWN	317.75	–1.70	G	0.17	...	de los Reyes et al. (2012)
HESS J1503–582	UNID	319.62	0.29	G	0.26	...	Renaud et al. (2008)
HESS J1507–622	UNID	317.95	–3.49	G	0.15	...	H.E.S.S. Collaboration et al. (2011c)
HESS J1514–591	PWN	320.33	–1.19	EG	0.11	0.04	Aharonian et al. (2005b)
HESS J1554–550	PWN	327.16	–1.07	PS	...	...	Acero et al. (2012)
HESS J1614–518	MSC	331.52	–0.58	EG	0.23	0.15	Aharonian et al. (2006d)
HESS J1616–508	PWN	332.39	–0.14	G	0.14	...	Aharonian et al. (2006d)
HESS J1626–490	UNID	334.77	0.05	EG	0.07	0.10	Aharonian et al. (2008c)
HESS J1632–478	PWN	336.38	0.19	EG	0.21	0.06	Aharonian et al. (2006d)
HESS J1634–472	UNID	337.11	0.22	G	0.11	...	Aharonian et al. (2006d)
HESS J1640–465	PWN	338.32	–0.02	G	0.04	...	Aharonian et al. (2006d)
HESS J1646–458A	MSC	339.57	–0.02	G	0.35	...	Abramowski et al. (2012)
HESS J1646–458B	MSC	339.01	–0.79	G	0.25	...	Abramowski et al. (2012)
HESS J1702–420	UNID	344.30	–0.18	EG	0.30	0.15	Aharonian et al. (2006d)
HESS J1708–443	PWN	343.06	–2.38	G	0.29	...	H.E.S.S. Collaboration et al. (2011b)
HESS J1718–385	PWN	348.83	–0.49	EG	0.15	0.07	Aharonian et al. (2007)
HESS J1729–345	UNID	353.44	–0.13	G	0.14	...	H.E.S.S. Collaboration et al. (2011a)
HESS J1804–216	UNID	8.40	–0.03	EG	0.16	0.27	Aharonian et al. (2006d)
HESS J1809–193	PWN	11.18	–0.09	EG	0.53	0.25	Aharonian et al. (2007)
HESS J1813–178	PWN	12.81	–0.03	G	0.04	...	Aharonian et al. (2006d)
HESS J1818–154	PWN	15.41	0.17	G	0.14	...	Hofverberg et al. (2011)
HESS J1825–137	PWN	17.71	–0.70	EG	0.13	0.12	Aharonian et al. (2006b)
HESS J1831–098	PWN	21.85	–0.11	G	0.15	...	Sheidaei (2011)
HESS J1833–105	PWN	21.51	–0.88	PS	...	...	Djannati-Ataï et al. (2008)
HESS J1834–087	UNID	23.24	–0.31	G	0.09	...	Aharonian et al. (2006d)
HESS J1837–069	UNID	25.18	–0.12	EG	0.12	0.05	Aharonian et al. (2006d)
HESS J1841–055	UNID	26.80	–0.20	EG	0.41	0.25	Aharonian et al. (2008c)
HESS J1843–033	UNID	29.30	0.51	PS	...	...	Hoppe (2008)
MGRO J1844–035	UNID	28.91	–0.02	PS	...	...	Abdo et al. (2009e)
HESS J1846–029	PWN	29.70	–0.24	PS	...	...	Djannati-Ataï et al. (2008)
HESS J1848–018	UNID	31.00	–0.16	G	0.32	...	Chaves et al. (2008)
HESS J1849–000	PWN	32.64	0.53	PS	...	...	Terrier et al. (2008)
HESS J1857+026	UNID	35.96	–0.06	EG	0.11	0.08	Aharonian et al. (2008c)

Table 1—Continued

Name	Class	$l$ (deg)	$b$ (deg)	TeV morphology	$\sigma_1$ (deg)	$\sigma_2$ (deg)	Reference
HESS J1858+020	UNID	35.58	−0.58	EG	0.08	0.02	Aharonian et al. (2008c)
MGRO J1900+039	UNID	37.42	−0.11	PS	...	...	Abdo et al. (2009e)
MGRO J1908+06	UNID	40.39	−0.79	G	0.34	...	Aharonian et al. (2009)
HESS J1912+101	PWN	44.39	−0.07	G	0.26	...	Aharonian et al. (2008a)
VER J1930+188	PWN	54.10	0.26	PS	...	...	Acciari et al. (2010)
MGRO J1958+2848	PWN	65.85	−0.23	PS	...	...	Abdo et al. (2009e)
VER J1959+208	PSR	59.20	−4.70	PS	...	...	Hall et al. (2003)
VER J2016+372	UNID	74.94	1.15	PS	...	...	Aliu (2011)
MGRO J2019+37	PWN	75.00	0.39	G	0.55	...	Abdo et al. (2007)
MGRO J2031+41A	UNID	79.53	0.64	G	1.50	...	Abdo et al. (2007)
MGRO J2031+41B	UNID	80.25	1.07	G	0.10	...	Bartoli et al. (2012)
MGRO J2228+61	PWN	106.57	2.91	PS	...	...	Abdo et al. (2009e)
W49A	SFR	43.27	−0.00	PS	...	...	Brun et al. (2011)

a- This work was presented at the "Supernova Remnants and Pulsar Wind Nebulae in the Chandra Era", 2009. See [http://cxc.harvard.edu/cdo/snr09/pres/DjannatiAtai\\_Arache\\_v2.pdf](http://cxc.harvard.edu/cdo/snr09/pres/DjannatiAtai_Arache_v2.pdf).

Note. — VHE sources analyzed with LAT observations. The first two columns list the VHE source names and classifications as defined in the TeV catalog (see Section 2): PWN for Pulsar Wind Nebulae, PSR for Pulsars, UNID for Unidentified sources, MSC for Massive Star Clusters and SFR for Star Forming Regions. The third and fourth column give the Galactic longitude and latitude for each source. The fifth column presents the best-fit morphology of the source when observed by VHE experiments: PS, G and EG respectively stand for point-source, Gaussian and elliptical Gaussian. The sixth and seventh columns present the Gaussian and elliptical Gaussian extension. A reference is cited in the eighth column.

### 3. CONVENTIONS AND METHODS

111

112 The LAT is a  $\gamma$ -ray telescope that detects photons by conversion into electron-positron  
 113 pairs. It operates in the energy range between 20 MeV and more than 300 GeV. Details of the  
 114 instrument and data processing are given in Atwood et al. (2009). The on-orbit calibration  
 115 is described in Abdo et al. (2009d) and Ackermann et al. (2012). This Section will present  
 116 the data set and the method used to analyze LAT data.

117

#### 3.1. Dataset

118 This paper uses 45 months of data collected from 2008 August 4 to 2012 April 18  
 119 (Mission Elapsed Time: 239557440-356439741 s) for regions centered on the positions of  
 120 each VHE source. We excluded  $\gamma$ -rays coming from a zenith angle larger than  $100^\circ$ . We  
 121 used the Pass 7 Clean event class that has substantially less instrumental background above  
 122 10 GeV with only a marginal loss in effective area, compared to the Pass 7 Source event  
 123 class (Ackermann et al. 2012).

124 We analyzed LAT data only between 10 and 316 GeV to avoid systematics associated  
 125 with the modeling of adjacent sources with soft spectra. It also reduces systematics asso-  
 126 ciated with imperfect modeling of the Galactic diffuse emission. The maximum energy of  
 127 316 GeV increases the overlap between the energy range covered by the VHE experiments  
 128 and the LAT. The 100 to 316 GeV energy range was also shown to be crucial in previous  
 129 analyses like Rousseau et al. (2012).

130 Figure 1 shows a background-subtracted count map of the Galactic Plane ob-  
 131 served by the LAT above 10 GeV. The bright Vela ( $l, b = 263^\circ 55, -2^\circ 79$ ) and Geminga  
 132 ( $l, b = 195^\circ 13, 4^\circ 27$ ) pulsars, and the SNR IC 443 ( $l, b = 189^\circ 06, 3^\circ 23$ ) clearly stand out. In  
 133 addition to these well-known objects, a large number of other sources are apparent. Several  
 134 are coincident with sources detected by VHE experiments, such as HESS J1614–518 and  
 135 HESS J1616–508 (Lande et al. 2012), and will be discussed in Section 4. The large number  
 136 of other sources visible in the map highlights the LAT sensitivity at high energies.

137

#### 3.2. Modeling the Regions of Interest

138 Two different software packages for maximum-likelihood fitting were used to analyze  
 139 LAT data: `gtlike` and `pointlike`. These tools fit LAT data with a parametrized model  
 140 of the sky, including models for the instrumental, extragalactic and Galactic components of

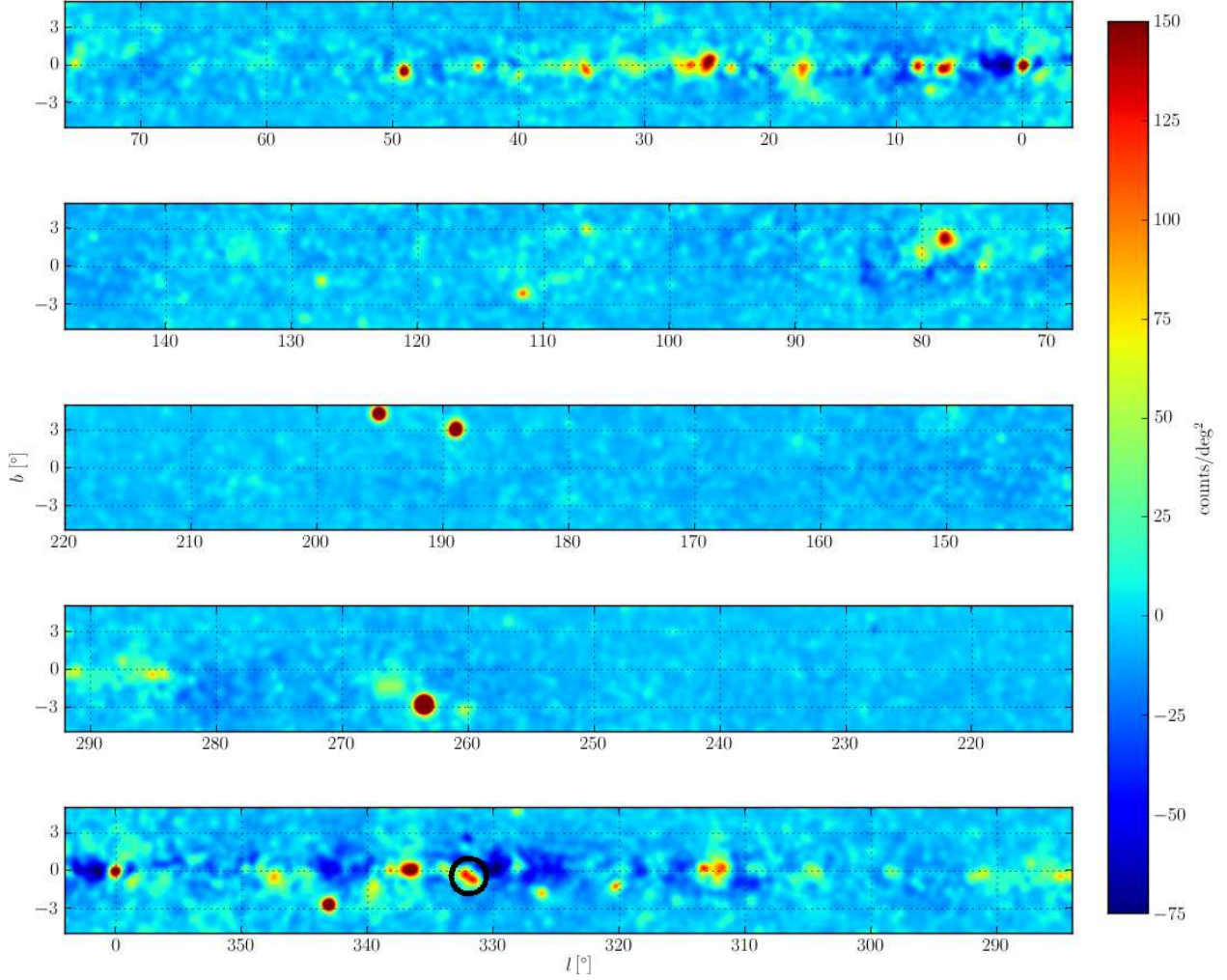


Fig. 1.— Count map of the Galactic plane in the energy range between 10 GeV and 316 GeV with the contribution of the Galactic diffuse, isotropic diffuse, and identified blazars subtracted. All sources associated to blazars are subtracted using the spectral parameters listed in 1FHL. Most of the large positive residuals in the map are Galactic sources, while a few could be unassociated blazars. The count map is smoothed with a Gaussian of  $0^{\circ}27$ . The black circle shows the positions of HESS J1614–518 and HESS J1616–508.

141 the background.

142 The first one, `gtlike`, is a maximum-likelihood method distributed in the *Fermi* Science  
 143 Tools by the FSSC<sup>2</sup>. We used version 09-28-00 of the package in binned mode. `pointlike` is

---

<sup>2</sup>*Fermi* Science Support Center: <http://fermi.gsfc.nasa.gov/ssc/>

144 an alternate software package that we used to fit the positions of point-like sources and fit the  
 145 spatial parameters of spatially-extended sources. Kerr (2011) describes the implementation  
 146 of `pointlike`, and Lande et al. (2012) validates `pointlike`’s extension-fitting functionality.  
 147 In `pointlike`, the data are binned spatially, using a HEALPix pixellization<sup>3</sup> (Górski et al.  
 148 2005), and spectrally, and the likelihood is maximized over all bins in a region.

149 We used `pointlike` to evaluate a position and extension estimate in the LAT data for  
 150 each source of our sample. Using those morphologies, we used `gtlike` to obtain the best-  
 151 fit spectral parameters and statistical significances. `gtlike` makes fewer approximations in  
 152 calculating the likelihood for spectra than `pointlike`. Both methods agree with each other  
 153 within 10% for all derived quantities, but all spectral parameters quoted in the following  
 154 were obtained using `gtlike`.

155 Since `pointlike` and `gtlike` use two different shapes for the regions of the sky modeled  
 156 for each source, we included photons within a radius of  $5^\circ$  centered on our source of interest  
 157 when using `pointlike` and within a  $7^\circ \times 7^\circ$  square region aligned with Galactic coordinates  
 158 when using `gtlike`. We tried to keep the two methods as close as possible by using the  
 159 same conventions, i.e. same energy binning of 8 energy bins per decade between 10 GeV and  
 160 316 GeV, and the same optimizer: MINUIT (James & Roos 1975).

161 The Galactic diffuse emission was modeled by the standard LAT interstellar emission  
 162 model `ring_2yearp7v6_v0.fits`. The residual cosmic-ray background and extragalactic  
 163 radiation are described by a single isotropic component with a spectral shape described by  
 164 the file `isotrop_2year_P76_clean_v0.txt`. The models have been released and described  
 165 by the *Fermi*-LAT Collaboration through the FSSC<sup>4</sup>. In the following, we fit the Galactic  
 166 diffuse normalization. Since the isotropic diffuse component is not well constrained over the  
 167 small regions of interest used in this work, we fixed its normalization to 1.

168 We included in our sky model all cataloged LAT sources within a radius of  $10^\circ$  of each  
 169 source of interest and listed in the hard source list (Paneque et al. 2013), henceforth “1FHL”.  
 170 The 1FHL catalog is a forthcoming catalog of sources using three years of LAT data above  
 171 10 GeV. The data selection used clean events as done in this work. The spectral parameters  
 172 of sources closer than  $2^\circ$  to the source of interest were fit, while the spectra of all other 1FHL  
 173 sources were fixed.

174  $\gamma$ -ray pulsars are found near many of the VHE sources. Table 2 summarizes the sources  
 175 analyzed in this paper that are near a LAT-detected pulsar. In the LAT energy range,

---

<sup>3</sup>The HEALPix libraries can be obtained from: <http://healpix.jpl.nasa.gov/>

<sup>4</sup>Background models are available at: <http://fermi.gsfc.nasa.gov/ssc/data/access/lat/BackgroundModels.html>

Table 2. VHE sources with a LAT detected pulsar within  $0^\circ5$

Name	Pulsar Name	distance (deg)	2FGL name	In the model	Justification
VER J0006+727	PSR J0007+7303	0.26	2FGL J0007.0+7303	N	a
MGRO J0631+105	PSR J0631+1036	0.10	2FGL J0631.5+ 1035	N	a
MGRO J0632+17	PSR J0633+1746	0.00	2FGL J0633.9+1746	N	a
HESS J1018–589	PSR J1016–5857	0.22	2FGL J1016.5–5858	N	a
HESS J1023–575	PSR J1023–5746	0.05	2FGL J1022.7–5741	N	b
HESS J1026–582	PSR J1028–5819	0.27	2FGL J1028.5–5819	Y	...
HESS J1119–614	PSR J1119–6127	0.07	2FGL J1118.8–6128	N	a
HESS J1356–645	PSR J1357–6429	0.12	2FGL J1356.0–6436	N	a
HESS J1418–609	PSR J1418–6058	0.05	2FGL J1418.7–6058	N	b
HESS J1420–607	PSR J1420–6048	0.05	2FGL J1420.1–6047	N	b
HESS J1458–608	PSR J1459–6053	0.17	2FGL J1459.4–6054	N	a
HESS J1514–591	PSR J1513–5908	0.03	...	N	b
HESS J1646–458B	PSR J1648–4611	0.42	2FGL J1646–4611	N	c
HESS J1702–420	PSR J1702–4128	0.53	...	N	c
HESS J1708–443	PSR J1709–4429	0.25	2FGL J1709.7–4429	N	b
HESS J1718–385	PSR J1718–3825	0.13	2FGL J1718.3–3827	N	a
HESS J1804–216	PSR J1803–2149	0.27	2FGL J1803.3–2148	N	b
HESS J1833–105	PSR J1833–1034	0.01	2FGL J1833.6–1032	N	a
HESS J1841–055	PSR J1838–0537	0.48	2FGL J1839.0–0539	Y	...
MGRO J1908+06	PSR J1907+0602	0.23	2FGL J1907.9+0602	N	a
MGRO J1958+2848	PSR J1958+2846	0.12	2FGL J1958.6+2845	N	a
VER J1959+208	PSR J1959+2048	0.02	2FGL J1959.5+2047	N	a
MGRO J2019+37	PSR J2021+3651	0.36	2FGL J2021.0+3651	N	b
MGRO J2031+41B	PSR J2032+4127	0.05	2FGL J2032.2+4126	N	b
MGRO J2228+61	PSR J2229+6114	0.09	2FGL J2229+6114	N	a

- a- The distance between the pulsar and the source is closer than  $0^\circ27$ .
- b- The pulsar is located inside the edge of the shape observed by VHE experiments.
- c- Not a and not b, but no significant excess above 10 GeV at the position of the pulsar.

Note. — Sources with a LAT-detected  $\gamma$ -ray pulsar within  $0^\circ5$ . The first two columns list the names of the VHE sources and their associated pulsars. The third column is the angular distance between the center of the VHE source and the LAT pulsar. The pulsar position comes from 2PC. The fourth column gives the pulsar 2FGL name. The fifth column says if the emission from the pulsar was included in the model of the background emission. “Y” means the emission was included and “N” means that it was not. The sixth column gives the justification when the pulsar is not included in the model.

176 pulsars tend to be brighter than their associated PWNe (Ackermann et al. 2011). During  
 177 the fit, the observed photon sample is shared by all modeled sources. The high energy range  
 178 used in this work prevents a reasonable fit of a pulsar component modeled by a power law  
 179 with an exponential cut-off spectrum. If a pulsar’s model overestimates its emission above  
 180 10 GeV, a putative PWN emission would be underestimated. This effect could obscure  
 181 the detection of a faint PWN. On the contrary, not including an existing source, such as  
 182 a pulsar, would artificially increase the flux attributed to a putative PWN at low energy.  
 183 Therefore, we decided to keep as separate sources in the model all pulsars located outside  
 184 the VHE experiment template and more than 0°:27 away from the source of interest. The  
 185 0°:27 radius corresponds to the 68% containment radius of the Point Spread Function (PSF)  
 186 averaged over energies above 10 GeV (Ackermann et al. 2012). For VHE sources less than  
 187 0°:27 from a LAT-detected pulsar, we analyzed the sources twice. Removing the pulsar from  
 188 the background model amounts to neglecting it, while leaving it in the background model  
 189 amounts to subtracting the underlying pulsar contribution from each putative PWN. In all  
 190 cases the parameters of the pulsar models have been fixed to those obtained in the 2FGL  
 191 catalog (Nolan et al. 2012). If contamination from the pulsar is a concern, it is possible to  
 192 phase-fold photons and analyze the data in the off-peak phase intervals of the pulsar. This  
 193 will be performed in 2PC. Here we analyze data at all phases to have the largest possible  
 194 statistics and therefore better sensitivity to faint PWNe.

195 Due to the 45-months integration time of our analysis compared to the 36 months of  
 196 the forthcoming 1FHL catalog, we expected to find new statistically-significant background  
 197 sources. To prevent bias from these sources, we included in our model any nearby background  
 198 sources with a significance above  $4\sigma$  ( $TS > 25$  with four degrees of freedom, d.o.f.). We fit  
 199 their spectra with power laws. The locations and spectra of the six such sources found in  
 200 our analysis are described in Table 3.

### 201 3.3. Analysis Procedure

We developed a uniform procedure for analyzing any potential emission in the 58 regions listed in Table 1. The small statistics above 10 GeV and the narrow energy range (1.5 decade) prevent any spectral curvature to be significant as will be discussed in the 1FHL catalog. Therefore, in the following we derived the spectra assuming a power-law spectral model:

$$\frac{dF}{dE} = N_0 \left( \frac{E}{E_0} \right)^{-\Gamma} \quad (1)$$

202 where  $N_0$  is the normalization,  $\Gamma$  is the spectral index, and  $E_0$  is the scale parameter. To  
 203 minimize the covariance between  $N_0$  and  $\Gamma$ , we ran the analysis twice. In the first iteration,

204 we fitted the source assuming a power-law model depending on the integral flux  $F$  and  $\Gamma$ ,

$$\frac{dF}{dE} = \frac{F(-\Gamma + 1)E^{-\Gamma}}{E_{\max}^{-\Gamma+1} - E_{\min}^{-\Gamma+1}}. \quad (2)$$

205 Using the covariance matrix of the fit parameters, we derived the pivot energy  $E_p$ ,  
 206 computed as the energy at which the relative uncertainty on the normalization  $N_0$  was  
 207 minimal (Nolan et al. 2012). In a second iteration, we refitted the spectrum of the source  
 208 assuming a power-law spectral model (Eq. 1) with the scale parameter  $E_0$  fixed to  $E_p$ . For  
 209 sources not significantly detected, we computed a 99% confidence level (c.l.) Bayesian upper  
 210 limit on the flux of the source assuming the published VHE morphology and a power-law  
 211 photon spectral index of 2.

212 We performed the spatial analysis in two steps. As a first step, we assumed that the  
 213 LAT emission originates from the same population of emitting particles cooling by the same  
 214 radiation process as the VHE emission. These assumptions mean that there should be a  
 215 correlation between the spatial morphology of a source at LAT and VHE energies. While it is  
 216 possible for the  $\gamma$ -ray emission from PWNe to have both the synchrotron and IC components  
 217 visible in the LAT energy range (as in the case of the Crab nebula, Abdo et al. 2010b), this  
 218 scenario is unlikely for observations above 10 GeV since electrons of energy around 1 PeV  
 219 should radiate in a magnetic field  $\sim 0.3$  G to emit photons above 10 GeV. This value is  
 220 unrealistic for a PWN. A second exception would appear if the LAT and VHE emissions  
 221 originate from two different populations of electrons (as in the case of Vela–X, Abdo et al.  
 222 2010c). However, most PWNe observed by the LAT show only IC emission from the same  
 223 population responsible for the VHE emission (e.g., Abdo et al. 2010a; Grondin et al. 2011;  
 224 Rousseau et al. 2012) supporting our assumption in this first step.

225 We assumed that any LAT emission would have the same morphology as the best-fit  
 226 VHE morphology. Therefore, we modeled the spatial distribution of the emission as Gaussian  
 227 with a position and extension fixed at the value of the spatial best-fit performed in the VHE  
 228 energy range. To homogenize the analysis, if the source was modeled with an elliptical  
 229 Gaussian at VHE, the Gaussian was fixed to the averaged extension. We tested for the  
 230 significance of the source at LAT energies using a likelihood-ratio test:  $\text{TS} = 2 \times \log(\mathcal{L}_1/\mathcal{L}_0)$   
 231 where  $\mathcal{L}$  is the Poisson likelihood of obtaining the observed data given the assumed model,  
 232  $\mathcal{L}_1$  corresponds to the likelihood obtained by fitting a model of the source of interest and the  
 233 background model, and  $\mathcal{L}_0$  corresponds to the likelihood obtained by fitting the background  
 234 model only. In the following, we refer to the TS assuming the VHE shape as  $\text{TS}_{\text{TeV}}$ . By  
 235 assuming a fixed spatial model, our test has fewer d.o.f. which makes our test more sensitive  
 236 to the LAT emission, assuming that the VHE spatial model reproduces the LAT observation.

237 The formal statistical significance of this test can be obtained from Wilks theorem  
238 (Wilks 1938). In the null hypothesis, TS follows a  $\chi^2$  distribution with  $n$  d.o.f. where  $n$  is  
239 the number of additional parameters in the model. We consider a source to be significantly  
240 detected when  $\text{TS}_{\text{TeV}} \geq 16$ . Our test has only two d.o.f. (the flux and the spectral index) so  
241 our threshold corresponds to a formal significance of  $3.6 \sigma$ . For significantly detected sources,  
242  $\text{TS}_{\text{TeV}}$  is presented in Table 4.

Table 3. Additional background sources

Name	$l$ (deg)	$b$ (deg)	TS	Prefactor ( $\text{cm}^{-2} \text{s}^{-1} \text{MeV}^{-1}$ )	Spectral index
2FGL J1405.5–6121	311.81	0.30	31	$(1.2 \pm 0.4) \times 10^{-15}$	$1.8 \pm 0.3$
Background Source 1	333.59	–0.31	29	$(6.5 \pm 2.5) \times 10^{-17}$	$4.3 \pm 0.9$
Background Source 2	336.96	–0.07	25	$(1.2 \pm 0.4) \times 10^{-15}$	$1.9 \pm 0.4$
2FGL J1823.1–1338c	17.51	–0.12	30	$(4.9 \pm 1.9) \times 10^{-15}$	$2.9 \pm 0.7$
2FGL J1836.8–0623c	25.41	0.42	25	$(9.4 \pm 3.9) \times 10^{-16}$	$2.0 \pm 0.4$
PSR J1838–0536	26.28	0.62	16	$(5.0 \pm 1.8) \times 10^{-17}$	$4.1 \pm 1.0$

Note. — New background sources found in our analysis for energies above 10 GeV that are not included in 1FHL. The first three columns are their name, Galactic longitude, and Galactic latitude. The TS values for the sources are provided in the fourth column. The spectral results are presented in columns 5 and 6 assuming a power-law spectral model (Equation 1) with a scale parameter  $E_0 = 56.2$  GeV (corresponding to the mid-value of the energy range in logarithmic scale). PSR J1838–0536 improves the morphology fit of the diffuse source HESS J1841–055. The spectral fit is consistent with the pulsar component (spectral index of  $\sim 4$ ). Additional sources appearing to be spatially consistent with a 2FGL source are labeled with the name of the associated 2FGL source.

Table 4. Spatial results for detected sources

Name	ID	TS <sub>TeV</sub>	TS <sub>GeV</sub>	TS <sub>ext</sub>	$l$ (deg)	$b$ (deg)	Unc <sub>GeV</sub> (deg)	$\sigma$
VER J0006+727	PSR	655	1206	0	119.68	10.47	0.01, 0.01	< 0.07
<sup>a</sup>		2	...	...	...	...	...	...
MGRO J0632+17	PSR	699	2056	1	195.13	4.28	0.01, 0.01	< 0.08
<sup>a</sup>		5	...	...	...	...	...	...
HESS J1018–589	O	29	29	0	284.33	–1.66	0.04, 0.02	< 0.87
<sup>a</sup>		25	25	2	284.34	–1.65	0.04, 0.02	< 0.87
HESS J1023–575	PWNc	52	58	8	284.13	–0.45	0.03, 0.02	< 0.77
<sup>a</sup>		52	58	8	284.13	–0.45	0.03, 0.02	< 0.77
HESS J1119–614	PWNc	27	27	9	292.16	–0.56	0.05, 0.02	< 0.31
<sup>a</sup>		16	16	9	292.18	–0.57	0.05, 0.02	< 0.32
HESS J1303–631	PWNc	37	58	29	304.56	–0.11	0.04, 0.03	0.45 ± 0.09 ± 0.10
HESS J1356–645	PWN	24	26	3	309.71	–2.33	0.05, 0.01	< 0.39
<sup>a</sup>		24	26	3	309.71	–2.32	0.05, 0.01	< 0.39
HESS J1418–609	PSR	31	32	0	313.28	0.13	0.03, 0.01	< 0.32
<sup>a</sup>		15	...	...	...	...	...	...
HESS J1420–607	PWNc	42	42	0	313.55	0.27	0.04, 0.02	< 0.38
<sup>a</sup>		36	36	0	313.55	0.28	0.04, 0.02	< 0.39
HESS J1507–622	O	21	23	7	317.77	–3.60	0.05, 0.03	< 1.04
<sup>a</sup>		21	23	7	317.76	–3.61	0.05, 0.03	< 1.04
HESS J1514–591	PWN	156	147	10	320.35	–1.25	0.03, 0.01	< 0.16
<sup>a</sup>		156	147	10	320.35	–1.25	0.03, 0.01	< 0.16
HESS J1614–518	O	110	133	47	331.62	–0.74	0.04, 0.03	0.28 ± 0.03 ± 0.05
HESS J1616–508	PWNc	75	94	31	332.39	–0.27	0.04, 0.02	0.25 ± 0.03 ± 0.05
HESS J1632–478	PWNc	137	161	56	336.50	0.10	0.03, 0.02	0.30 ± 0.06 ± 0.06
HESS J1634–472	O	33	34	1	337.23	0.35	0.03, 0.01	< 1.21
HESS J1640–465	PWNc	47	42	9	338.33	0.05	0.05, 0.01	< 1.17
HESS J1708–443	PSR	722	1153	0	343.11	–2.70	0.01, 0.01	< 0.05
<sup>a</sup>		33	64	0	343.12	–2.70	0.01, 0.01	< 0.09
HESS J1804–216	O	138	141	37	8.40	–0.09	0.04, 0.01	0.25 ± 0.03 ± 0.04
<sup>a</sup>		124	128	30	8.42	–0.10	0.04, 0.01	0.24 ± 0.03 ± 0.04
HESS J1825–137	PWN	56	82	30	17.55	–0.47	0.05, 0.03	0.44 ± 0.08 ± 0.09
HESS J1834–087	O	27	36	4	23.20	–0.26	0.05, 0.01	< 0.22
HESS J1837–069	PWNc	73	119	46	25.17	0.00	0.05, 0.03	0.36 ± 0.06 ± 0.04
HESS J1841–055	PWNc	64	70	32	27.01	–0.15	0.05, 0.03	0.38 ± 0.06 ± 0.06
HESS J1848–018	PWNc	19	19	0	30.90	–0.20	0.04, 0.01	< 1.50
HESS J1857+026	PWNc	53	55	8	36.08	0.02	0.04, 0.01	< 0.28
MGRO J1908+06	PSR	16	37	2	40.11	–0.84	0.03, 0.01	< 0.19
<sup>a</sup>		9	...	...	...	...	...	...
MGRO J1958+2848	PSR	21	24	0	65.88	–0.34	0.04, 0.01	< 0.56
<sup>a</sup>		8	...	...	...	...	...	...
VER J2016+372	O	31	33	1	74.86	1.22	0.05, 0.02	< 1.16
MGRO J2019+37	PSR	31	100	1	75.23	0.13	0.02, 0.01	< 0.07
<sup>a</sup>		5	...	...	...	...	...	...
MGRO J2031+41B	PSR	58	66	5	80.20	1.03	0.05, 0.01	< 2.47
<sup>a</sup>		12	...	...	...	...	...	...

Table 4—Continued

Name	ID	TS <sub>TeV</sub>	TS <sub>GeV</sub>	TS <sub>ext</sub>	$l$ (deg)	$b$ (deg)	Unc <sub>GeV</sub> (deg)	$\sigma$
MGRO J2228+61	PSR	94	113	0	106.65	2.94	0.02, 0.01	< 0.10
<sup>a</sup>		15	...	...	...	...	...	...

Note. — Results of the maximum likelihood spatial fits for LAT-detected VHE sources. “a” in the first column corresponds to the results with contribution of the pulsar associated in Table 2 subtracted from the emission of the source just above. Column 2 lists the classification for the LAT emission: either “PWN” for clearly identified PWNe, “PWNe” for PWNe candidates, “PSR” for pulsar emission, and “O” for anything else. Column 3 is the TS when the source is modeled with the spatial model obtained from VHE data. Column 4 is the TS when the source is modeled assuming it is point-like, and column 5 is the TS of the source assuming it is spatially-extended with a Gaussian spatial model. Columns 6 and 7 give the position of the source fit in our LAT analysis. Column 8 gives the statistical (68% confidence radius) and systematic uncertainties on the position. The methods for determining systematic uncertainties on the spatial parameters are described in Section 3.4. Column 9 gives the extension fit in the LAT energy range if TS<sub>ext</sub> > 16 or a 99 % c.l. upper limit on the extension otherwise.

243 As a second step, for significantly-detected sources, we then independently character-  
244 ized the best-fit morphology obtained from the LAT emission. Following the method of  
245 Nolan et al. (2012), we assumed the source to be point-like and fit its position. Following the  
246 method adopted in Lande et al. (2012), we then assumed the source to be spatially-extended  
247 with a Gaussian spatial model and fit its position and extension. From this, we obtained  
248  $TS_{\text{point}}$  and  $TS_{\text{Gaussian}}$ . We then defined the extension significance  $TS_{\text{ext}} = TS_{\text{Gaussian}} - TS_{\text{point}}$   
249 following the method of Lande et al. (2012) and set the threshold for claiming the source to be  
250 spatially extended as  $TS_{\text{ext}} > 16$ , corresponding to a significance of  $4\sigma$ .  $TS_{\text{GeV}} = TS_{\text{Gaussian}}$   
251 when  $TS_{\text{ext}} > 16$  and  $TS_{\text{GeV}} = TS_{\text{point}}$  otherwise. Table 4 lists eight significantly extended  
252 sources and 22 point sources. If the source was not significantly extended, we derived a 99%  
253 c.l. Bayesian upper limit on the extension.

Table 5. Spectral results for detected sources

Name	TS	$F_{10\text{ GeV}}^{316\text{ GeV}}$ ( $10^{-10}\text{ cm}^{-2}\text{ s}^{-1}$ )	$\Gamma$	$TS_{10\text{ GeV}}^{31\text{ GeV}}$	$F_{10\text{ GeV}}^{31\text{ GeV}}$ ( $10^{-10}\text{ cm}^{-2}\text{ s}^{-1}$ )	$TS_{31\text{ GeV}}^{100\text{ GeV}}$	$F_{31\text{ GeV}}^{100\text{ GeV}}$ ( $10^{-10}\text{ cm}^{-2}\text{ s}^{-1}$ )	$TS_{100\text{ GeV}}^{316\text{ GeV}}$	$F_{100\text{ GeV}}^{316\text{ GeV}}$ ( $10^{-10}\text{ cm}^{-2}\text{ s}^{-1}$ )
VER J0006+727	655	$11.3 \pm 0.9 \pm 1.2$	$3.96 \pm 0.25 \pm 0.36$	647	$11.2 \pm 0.9 \pm 2.0$	11	$0.4 \pm 0.2 \pm 0.2$	0	< 0.3
<sup>a</sup>	2	< 1.2	...	3	< 1.2	0	< 0.4	0	< 0.3
MGRO J0632+17	699	$34.9 \pm 2.1 \pm 10.2$	$4.53 \pm 0.25 \pm 0.51$	695	$36.8 \pm 2.0 \pm 10.1$	6	< 1.6	1	< 0.7
<sup>a</sup>	5	< 5.1	...	9	< 5.5	1	< 1.1	0	< 0.6
HESS J1018-589	29	$1.7 \pm 0.5 \pm 0.7$	$2.41 \pm 0.49 \pm 0.49$	25	$1.4 \pm 0.5 \pm 0.6$	0	< 0.6	6	< 0.6
<sup>a</sup>	25	$1.5 \pm 0.5 \pm 0.7$	$2.31 \pm 0.50 \pm 0.49$	20	$1.3 \pm 0.4 \pm 0.6$	0	< 0.6	6	< 0.6
HESS J1023-575	52	$4.6 \pm 0.9 \pm 1.2$	$1.99 \pm 0.24 \pm 0.32$	40	$3.8 \pm 0.8 \pm 1.8$	2	< 0.9	9	< 1.2
<sup>a</sup>	52	$4.6 \pm 0.9 \pm 1.2$	$1.99 \pm 0.24 \pm 0.32$	40	$3.8 \pm 0.8 \pm 1.8$	2	< 0.9	9	< 1.2
HESS J1119-614	27	$2.1 \pm 0.6 \pm 0.8$	$2.15 \pm 0.37 \pm 0.36$	17	$1.5 \pm 0.5 \pm 0.5$	1	< 0.7	11	$0.2 \pm 0.1 \pm 0.1$
<sup>a</sup>	16	$2.0 \pm 0.6 \pm 0.8$	$1.83 \pm 0.41 \pm 0.36$	5	< 2.1	1	< 0.8	11	$0.2 \pm 0.1 \pm 0.1$
HESS J1303-631	37	$3.6 \pm 0.9 \pm 2.1$	$1.53 \pm 0.23 \pm 0.37$	10	$1.6 \pm 0.7 \pm 1.5$	25	$1.6 \pm 0.5 \pm 0.7$	3	< 0.7
HESS J1356-645	24	$1.1 \pm 0.4 \pm 0.5$	$0.95 \pm 0.40 \pm 0.40$	0	< 0.9	14	$0.6 \pm 0.3 \pm 0.3$	10	$0.3 \pm 0.2 \pm 0.2$
<sup>a</sup>	24	$1.1 \pm 0.4 \pm 0.5$	$0.94 \pm 0.40 \pm 0.40$	0	< 0.9	14	$0.6 \pm 0.3 \pm 0.3$	10	$0.3 \pm 0.2 \pm 0.2$
HESS J1418-609	31	$4.0 \pm 1.0 \pm 1.3$	$3.52 \pm 0.81 \pm 0.61$	29	$3.6 \pm 0.9 \pm 1.2$	2	< 1.0	0	< 0.6
<sup>a</sup>	15	< 4.3	...	13	$2.6 \pm 0.9 \pm 1.2$	2	< 1.0	0	< 0.6
HESS J1420-607	42	$3.7 \pm 0.9 \pm 1.1$	$1.89 \pm 0.28 \pm 0.31$	19	$2.4 \pm 0.7 \pm 0.7$	13	$0.8 \pm 0.3 \pm 0.3$	12	$0.5 \pm 0.2 \pm 0.2$
<sup>a</sup>	36	$3.4 \pm 0.9 \pm 1.1$	$1.81 \pm 0.29 \pm 0.31$	15	$2.2 \pm 0.7 \pm 0.7$	13	$0.8 \pm 0.3 \pm 0.3$	12	$0.5 \pm 0.2 \pm 0.2$
HESS J1507-622	21	$1.5 \pm 0.5 \pm 0.5$	$2.33 \pm 0.48 \pm 0.48$	18	$1.2 \pm 0.4 \pm 0.4$	3	< 0.7	0	< 0.4
HESS J1514-591	156	$6.2 \pm 0.9 \pm 1.3$	$1.72 \pm 0.16 \pm 0.17$	69	$3.9 \pm 0.7 \pm 1.1$	54	$1.7 \pm 0.4 \pm 0.4$	36	$0.7 \pm 0.3 \pm 0.4$
HESS J1614-518	110	$9.9 \pm 1.4 \pm 3.1$	$1.75 \pm 0.15 \pm 0.18$	47	$6.1 \pm 1.1 \pm 2.7$	37	$2.6 \pm 0.6 \pm 0.8$	31	$1.1 \pm 0.4 \pm 0.3$
HESS J1616-508	75	$9.3 \pm 1.4 \pm 2.3$	$2.18 \pm 0.19 \pm 0.20$	46	$6.5 \pm 1.2 \pm 2.1$	29	$2.3 \pm 0.6 \pm 0.6$	3	< 1.0
HESS J1632-478	137	$11.8 \pm 1.5 \pm 5.3$	$1.82 \pm 0.14 \pm 0.19$	69	$7.8 \pm 1.2 \pm 4.2$	37	$2.6 \pm 0.6 \pm 0.9$	39	$1.5 \pm 0.4 \pm 0.5$
HESS J1634-472	33	$5.6 \pm 1.3 \pm 2.5$	$1.96 \pm 0.25 \pm 0.29$	20	$3.6 \pm 1.0 \pm 2.1$	12	$1.3 \pm 0.5 \pm 0.5$	2	< 0.8
HESS J1640-465	47	$5.0 \pm 1.0 \pm 1.7$	$1.95 \pm 0.23 \pm 0.20$	24	$3.4 \pm 0.9 \pm 1.3$	28	$1.7 \pm 0.5 \pm 0.5$	0	< 0.5
HESS J1708-443	722	$24.5 \pm 1.7 \pm 3.5$	$3.80 \pm 0.24 \pm 0.33$	714	$23.9 \pm 1.6 \pm 3.0$	14	$1.1 \pm 0.4 \pm 0.5$	6	< 1.0
<sup>a</sup>	33	$5.5 \pm 1.3 \pm 3.5$	$2.13 \pm 0.31 \pm 0.33$	17	$4.0 \pm 1.2 \pm 3.0$	11	$1.0 \pm 0.4 \pm 0.5$	6	< 1.0
HESS J1804-216	138	$14.2 \pm 1.6 \pm 3.1$	$2.10 \pm 0.16 \pm 0.24$	91	$10.1 \pm 1.4 \pm 2.3$	38	$2.9 \pm 0.7 \pm 0.6$	21	$1.2 \pm 0.4 \pm 0.4$
<sup>a</sup>	124	$13.4 \pm 1.6 \pm 3.1$	$2.04 \pm 0.16 \pm 0.24$	77	$9.3 \pm 1.4 \pm 2.3$	36	$2.8 \pm 0.7 \pm 0.6$	21	$1.2 \pm 0.4 \pm 0.4$
HESS J1825-137	56	$5.6 \pm 1.2 \pm 9.0$	$1.32 \pm 0.20 \pm 0.39$	10	$1.7 \pm 0.9 \pm 1.5$	30	$2.9 \pm 0.7 \pm 1.6$	17	$0.8 \pm 0.3 \pm 0.8$
HESS J1834-087	27	$5.5 \pm 1.2 \pm 2.5$	$2.24 \pm 0.34 \pm 0.42$	19	$4.2 \pm 1.1 \pm 1.9$	7	< 1.9	3	< 1.0
HESS J1837-069	73	$7.5 \pm 1.3 \pm 4.2$	$1.47 \pm 0.18 \pm 0.30$	28	$4.3 \pm 1.1 \pm 3.5$	21	$1.9 \pm 0.6 \pm 0.9$	27	$1.4 \pm 0.5 \pm 0.5$
HESS J1841-055	64	$10.9 \pm 0.8 \pm 4.1$	$1.60 \pm 0.27 \pm 0.33$	20	$7.4 \pm 1.6 \pm 2.9$	13	$2.1 \pm 0.7 \pm 1.0$	31	$1.8 \pm 0.5 \pm 0.7$
HESS J1848-018	19	$7.4 \pm 1.9 \pm 2.7$	$2.46 \pm 0.50 \pm 0.51$	16	$5.8 \pm 1.6 \pm 2.9$	4	< 2.6	0	< 1.0
HESS J1857+026	53	$4.2 \pm 0.3 \pm 1.3$	$1.01 \pm 0.24 \pm 0.25$	6	< 2.9	19	$1.2 \pm 0.4 \pm 0.4$	31	$1.5 \pm 0.4 \pm 0.4$

Table 5—Continued

Name	TS	$F_{10\text{ GeV}}^{316\text{ GeV}}$ ( $10^{-10}\text{ cm}^{-2}\text{ s}^{-1}$ )	$\Gamma$	$\text{TS}_{10\text{ GeV}}^{31\text{ GeV}}$	$F_{10\text{ GeV}}^{31\text{ GeV}}$ ( $10^{-10}\text{ cm}^{-2}\text{ s}^{-1}$ )	$\text{TS}_{31\text{ GeV}}^{100\text{ GeV}}$	$F_{31\text{ GeV}}^{100\text{ GeV}}$ ( $10^{-10}\text{ cm}^{-2}\text{ s}^{-1}$ )	$\text{TS}_{100\text{ GeV}}^{316\text{ GeV}}$	$F_{100\text{ GeV}}^{316\text{ GeV}}$ ( $10^{-10}\text{ cm}^{-2}\text{ s}^{-1}$ )
MGRO J1908+06	16	$4.6 \pm 1.3 \pm 1.5$	$3.50 \pm 1.11 \pm 1.60$	11	$3.4 \pm 1.2 \pm 1.2$	2	< 1.6	7	< 1.5
<sup>a</sup>	9	< 5.6	...	3	< 3.9	2	< 1.6	7	< 1.5
MGRO J1958+2848	21	$1.3 \pm 0.4 \pm 0.7$	$4.36 \pm 1.09 \pm 1.21$	19	$1.3 \pm 0.5 \pm 0.5$	0	< 0.3	0	< 0.3
<sup>a</sup>	8	< 1.8	...	15	$1.2 \pm 0.5 \pm 0.5$	0	< 0.3	0	< 0.3
VER J2016+372	31	$1.8 \pm 0.5 \pm 0.8$	$2.45 \pm 0.44 \pm 0.49$	26	$1.6 \pm 0.5 \pm 0.5$	3	< 0.6	3	< 0.5
MGRO J2019+37	31	$4.4 \pm 1.7 \pm 1.1$	$6.37 \pm 3.04 \pm 1.21$	26	$5.4 \pm 1.2 \pm 1.8$	0	< 0.7	1	< 0.8
<sup>a</sup>	5	< 4.7	...	9	< 5.3	0	< 0.8	1	< 0.8
MGRO J2031+41B	58	$6.4 \pm 1.0 \pm 1.1$	$3.07 \pm 0.33 \pm 0.37$	58	$6.2 \pm 1.0 \pm 1.3$	3	< 1.0	0	< 0.4
<sup>a</sup>	12	< 4.4	...	11	$3.0 \pm 0.9 \pm 1.0$	1	< 0.9	0	< 0.4
MGRO J2228+61	94	$2.8 \pm 0.5 \pm 0.5$	$3.06 \pm 0.41 \pm 0.42$	87	$2.5 \pm 0.5 \pm 0.5$	7	< 0.8	0	< 0.2
<sup>a</sup>	15	< 2.0	...	9	< 1.8	7	< 0.8	0	< 0.2

Note. — Results of the maximum likelihood spectral fits for LAT-detected VHE sources. These results are obtained assuming the sources have the same morphology as was measured by VHE experiments. “a” in the first column corresponds to the results with the contribution of pulsars associated in Table 2 subtracted from the SED for the source just above. Columns 2 to 4 respectively give the TS, the integrated flux and the spectral index of the source fit in the energy range from 10 GeV to 316 GeV. Columns 5 to 10 give the TS and the integrated flux fit in three logarithmically-spaced energy ranges: 10-31 GeV, 31-100 GeV, 100-316 GeV. When the TS in the energy bin is < 10 a 99% c.l. upper limit on the flux is given instead. The two uncertainties respectively correspond to the statistical and systematic uncertainties.

Table 6. Spectral results for undetected sources

Name	TS	$F_{10\text{ GeV}}^{316\text{ GeV}}$ ( $10^{-10}\text{ cm}^{-2}\text{ s}^{-1}$ )	$TS_{10\text{ GeV}}^{31\text{ GeV}}$	$F_{10\text{ GeV}}^{31\text{ GeV}}$ ( $10^{-10}\text{ cm}^{-2}\text{ s}^{-1}$ )	$TS_{31\text{ GeV}}^{100\text{ GeV}}$	$F_{31\text{ GeV}}^{100\text{ GeV}}$ ( $10^{-10}\text{ cm}^{-2}\text{ s}^{-1}$ )	$TS_{100\text{ GeV}}^{316\text{ GeV}}$	$F_{100\text{ GeV}}^{316\text{ GeV}}$ ( $10^{-10}\text{ cm}^{-2}\text{ s}^{-1}$ )
MGRO J0631+105	6	< 1.4	4	< 1.2	3	< 0.6	0	< 0.4
<sup>a</sup>	2	< 1.0	0	< 0.8	3	< 0.6	0	< 0.4
HESS J1026–582	1	< 1.6	0	< 1.6	0	< 0.4	6	< 0.7
<sup>a</sup>	1	< 1.6	0	< 1.6	0	< 0.4	6	< 0.7
HESS J1427–608	5	< 1.9	0	< 1.2	2	< 0.8	4	< 0.6
HESS J1458–608	13	< 2.6	13	$1.7 \pm 0.5 \pm 0.7$	0	< 0.5	0	< 0.3
<sup>a</sup>	13	< 2.6	13	$1.7 \pm 0.5 \pm 0.7$	0	< 0.5	0	< 0.3
HESS J1503–582	10	< 3.9	1	< 2.2	4	< 1.5	9	< 1.0
HESS J1554–550	0	< 0.5	0	< 0.6	0	< 0.3	0	< 0.3
HESS J1626–490	1	< 2.3	1	< 2.0	1	< 1.0	0	< 0.6
HESS J1646–458A	0	< 2.8	0	< 1.7	1	< 1.9	1	< 1.0
<sup>a</sup>	0	< 2.7	0	< 1.7	1	< 1.9	1	< 1.0
HESS J1646–458B	6	< 4.7	0	< 2.6	4	< 1.9	5	< 1.2
<sup>a</sup>	4	< 4.3	0	< 2.2	4	< 1.9	5	< 1.3
HESS J1702–420	6	< 4.7	0	< 2.6	8	< 2.4	1	< 0.8
<sup>a</sup>	6	< 4.5	0	< 2.5	8	< 2.4	1	< 0.8
HESS J1718–385	3	< 2.1	0	< 1.5	0	< 0.8	6	< 0.9
<sup>a</sup>	3	< 2.1	0	< 1.5	0	< 0.8	6	< 0.9
HESS J1729–345	0	< 1.4	0	< 1.4	0	< 0.8	0	< 0.5
HESS J1809–193	15	< 8.5	11	$4.7 \pm 1.5 \pm 2.1$	3	< 2.3	1	< 1.0
HESS J1813–178	3	< 2.5	0	< 1.4	5	< 1.6	1	< 0.7
HESS J1818–154	0	< 1.6	0	< 1.6	0	< 0.8	0	< 0.4
HESS J1831–098	0	< 1.9	0	< 1.5	0	< 1.0	0	< 0.6
HESS J1833–105	4	< 2.1	3	< 1.9	1	< 0.7	0	< 0.7
<sup>a</sup>	4	< 2.1	3	< 1.9	1	< 0.7	0	< 0.7
HESS J1843–033	0	< 0.9	0	< 1.0	0	< 0.5	0	< 0.5
MGRO J1844–035	0	< 1.4	0	< 1.2	0	< 0.9	0	< 0.5
HESS J1846–029	2	< 2.0	5	< 2.4	0	< 0.5	0	< 0.4
HESS J1849–000	0	< 1.3	1	< 1.5	0	< 0.5	0	< 0.5
HESS J1858+020	0	< 1.1	0	< 1.2	0	< 0.5	0	< 0.4
MGRO J1900+039	0	< 1.2	0	< 1.3	0	< 0.6	0	< 0.4
HESS J1912+101	10	< 4.6	2	< 2.7	8	< 2.0	4	< 1.1
VER J1930+188	0	< 1.0	1	< 1.1	0	< 0.4	0	< 0.3
VER J1959+208	0	< 0.3	0	< 0.3	0	< 0.3	0	< 0.4

Table 6—Continued

Name	TS	$F_{10\text{ GeV}}^{316\text{ GeV}}$ ( $10^{-10}\text{ cm}^{-2}\text{ s}^{-1}$ )	$TS_{10\text{ GeV}}^{31\text{ GeV}}$	$F_{10\text{ GeV}}^{31\text{ GeV}}$ ( $10^{-10}\text{ cm}^{-2}\text{ s}^{-1}$ )	$TS_{31\text{ GeV}}^{100\text{ GeV}}$	$F_{31\text{ GeV}}^{100\text{ GeV}}$ ( $10^{-10}\text{ cm}^{-2}\text{ s}^{-1}$ )	$TS_{100\text{ GeV}}^{316\text{ GeV}}$	$F_{100\text{ GeV}}^{316\text{ GeV}}$ ( $10^{-10}\text{ cm}^{-2}\text{ s}^{-1}$ )
MGRO J2031+41A	14	< 29.6	9	< 22.6	3	< 8.4	4	< 2.3
W49A	3	< 2.4	0	< 1.6	3	< 1.0	3	< 0.8

Note. — Results of the maximum likelihood spectral fits for sources not detected in our LAT analysis. These results are obtained assuming the sources have the same morphology as was measured by VHE. “a” in the first column corresponds to the results with the contribution of pulsars associated in Table 2 subtracted from the SED for the source just above. Columns 2 and 3 respectively give the TS and a 99% c.l. upper limit on the integrated flux in the 10 to 316 GeV energy range. Columns 4 to 9 give the TS and the integrated flux in three logarithmically-spaced energy ranges: 10-31 GeV, 31-100 GeV and 100-316 GeV. When the TS in the energy bin is < 10 a 99% c.l. upper limit on the flux is given. The two uncertainties respectively correspond to the statistical and systematic uncertainties.

254 The LAT spectra of the sources have been derived assuming the published VHE mor-  
255 phology. In addition to performing a spectral fit over the entire energy range, we computed  
256 a SED by fitting the flux of the source independently in 3 energy bins spaced uniformly in  
257 log from 10 GeV to 316 GeV. During this fit, we fixed the spectral index of the source at 2 as  
258 well as the model of background sources to the best-fit obtained in the whole energy range.  
259 We define a detection in the energy bin when  $TS \geq 10$  and otherwise compute a flux upper  
260 limit using the same method as for the fit in the full energy range. All spectral results are  
261 presented in Tables 5 and 6.

### 262 3.4. Systematics

263 Two main systematic uncertainties can affect the extension fit: uncertainties in our  
264 model of the Galactic diffuse emission and uncertainties in our knowledge of the LAT PSF.  
265 We used the procedure described in Lande et al. (2012) and obtained the total systematic  
266 error on the source extension by adding the two errors in quadrature.

267 Three main systematic uncertainties can affect the LAT flux estimate for an extended  
268 source: uncertainties on the Galactic diffuse background, on the effective area and on the  
269 shape of the source. We combined these errors in quadrature to obtain an estimate of the  
270 total systematic uncertainty on spectral parameters.

271 The dominant uncertainty comes from the Galactic diffuse emission and was estimated  
272 by using the alternative model for Galactic diffuse emission described in Lande et al. (2012).  
273 The systematic due to the effective area was determined by using modified instrument re-  
274 sponse functions as explained in Ackermann et al. (2012).

275 The imperfect knowledge of the true  $\gamma$ -ray morphology introduces a last source of error.  
276 We derived an estimate of the uncertainty on the spectral parameters due to the uncertainty  
277 on the  $\gamma$ -ray morphology by computing the difference between the values obtained assuming  
278 the published VHE spatial model and those obtained assuming the best-fit GeV extension  
279 obtained in this analysis.

280 As discussed in Section 3.2, for the sources near LAT-detected pulsars, a fourth source  
281 of systematic uncertainties can affect the LAT flux estimate : the pulsar model. For these  
282 sources, we studied any potential contamination of the putative LAT  $\gamma$ -ray sources by pulsars  
283 by performing a second fit of the regions including the pulsars in our background models.  
284 The results are also included in Tables 4, 5 and 6 and are flagged with an “a”. The effects  
285 of pulsar contamination are discussed for individual sources in Section 4.

286 We caution that some LAT-detected pulsars may have spectra at LAT energies that  
 287 deviate from the simple exponential cutoff power law model assumed in the 2FGL catalog,  
 288 for energies above 10 GeV. Aliu et al. (2011) show this to be the case for the Crab pulsar.  
 289 In such cases, our fit could still be contaminated by the pulsar, especially in the lowest  
 290 energy bin between 10 GeV and 31.6 GeV. For instance, in the case of Geminga for which  
 291 this analysis detected no significant PWN like emission, the comparison of the energy flux  
 292 above 10 GeV between the 2FGL and the 1FHL catalogs shows a factor  $\sim 2$  smaller flux for  
 293 2FGL.

294 Table 5 shows that HESS J1825–137 and MGRO J0632+17 have large systematic un-  
 295 certainties. The uncertainty on HESS J1825–137 mainly comes from the term corresponding  
 296 to the source morphology. As can be seen in Tables 1 and 4, the LAT best-fit Gaussian has  
 297  $\sigma = 0^\circ.44$  while the VHE symmetric Gaussian has  $\sigma = 0^\circ.125$ . This difference of morphology  
 298 yields a difference in maximum likelihood flux of +155%.

299 The large systematic uncertainty on MGRO J0632+17 is not surprising since the VHE  
 300 source has an extension of more than  $1^\circ$ , while the LAT morphology is best-fit as a point  
 301 source located at the pulsar’s position.

#### 302 4. ANALYSIS RESULTS

303 We detected 30 statistically-significant LAT  $\gamma$ -ray sources among the 58 VHE sources.  
 304 The results of the spatial and spectral analyses are shown in Tables 4 and 5. In addition to  
 305 describing the LAT data analysis, we attempt to classify the origin of the GeV emission using  
 306 the spatial and spectral information from LAT data as well as multi-wavelength information.  
 307 We labeled each source as “PWN” when there is a clear PWN identification, “PWNC” when  
 308 the source is a PWN candidate, “PSR” when the emission is likely coming from the pulsar  
 309 only and “O” for other emission.

Table 7. Pulsar and PWN characteristics.

Name	PSR	$\dot{E}$ (ergs $^{-1}$ )	$\tau_C$ (kyr)	Distance (kpc)	Refs	$\gamma$ -ray pulsar
VER J0006+727	PSR J0007+7303	4.5e+35	13.9	1.4±0.3	(1)	Y
Crab	PSR J0534+2200	4.6e+38	1.2	2.0±0.5	(2)	Y
MGRO J0631+105	PSR J0631+1036	1.7e+35	43.6	1.0±0.2	(3)	Y
MGRO J0632+17	PSR J0633+1746	3.2e+34	342	0.2 $^{+0.2}_{-0.1}$	(4)	Y
Vela-X	PSR J0835-4510	6.9e+36	11.3	0.29±0.02	(5)	Y
HESS J1018-589	PSR J1016-5857	2.6e+36	21	2.9 $^{+0.6}_{-1.9}$ a	(6,7)	Y
HESS J1023-575	PSR J1023-5746	1.1e+37	4.6	2.8 <sup>b</sup>	(8)	Y
HESS J1026-582	PSR J1028-5819	8.4e+35	90	2.3±0.3	(9)	Y
HESS J1119-614	PSR J1119-6127	2.3e+36	1.6	8.4±0.4	(10)	Y
HESS J1303-631	PSR J1301-6305	1.7e+36	11	6.7 $^{+1.1}_{-1.2}$	(11, 12)	N
HESS J1356-645	PSR J1357-6429	3.1e+36	7.3	2.5 $^{+0.5}_{-0.4}$	(13)	Y
HESS J1418-609	PSR J1418-6058	4.9e+36	1.0	1.6±0.7	(14)	Y
HESS J1420-607	PSR J1420-6048	1.0e+37	13	5.6±0.9	(11,15)	Y
HESS J1458-608	PSR J1459-6053	9.1e+35	64.7	4 <sup>d</sup>	(16)	Y
HESS J1514-591	PSR J1513-5908	1.7e+37	1.56	4.2±0.6	(12)	Y
HESS J1554-550	...	...	18 <sup>c</sup>	7.8±1.3 <sup>e</sup>	(17, 18, 19)	N
HESS J1616-508	PSR J1617-5055	1.6e+37	8.13	6.8±0.7 <sup>f</sup>	(12)	N
HESS J1632-478	...	3.0e+36 <sup>g</sup>	20	3.0 <sup>d</sup>	(20)	N
HESS J1640-465	...	4.0e+36 <sup>g</sup>	...	...	(22, 23)	N
HESS J1646-458B	PSR J1648-4611	2.1e+35	110	5.0 ± 0.7	(21)	Y
HESS J1702-420	PSR J1702-4128	3.4e+35	55	4.8±0.6	(24)	Y
HESS J1708-443	PSR J1709-4429	3.4e+36	17.5	2.3±0.3	(25)	Y
HESS J1718-385	PSR J1718-3825	1.3e+36	89.5	3.6±0.4	(26, 12)	Y
HESS J1804-216	PSR J1803-2137	2.2e+36	16	3.8 $^{+0.4}_{-0.5}$	(12)	N
HESS J1809-193	PSR J1809-1917	1.8e+36	51.3	3.5±0.4 <sup>f</sup>	(12)	N
HESS J1813-178	PSR J1813-1749	6.8e+37	5.4	4.7 <sup>h</sup>	(12, 27)	N
HESS J1818-154	PSR J1818-1541	2.3e+33	9 <sup>i</sup>	7.8 $^{+1.6}_{-1.4}$ f	(28)	N
HESS J1825-137	PSR J1826-1334	2.8e+36	21	3.9±0.4	(12, 29)	N
HESS J1831-098	PSR J1831-0952	1.1e+36	128	4.0±0.4 <sup>f</sup>	(12, 30)	N
HESS J1833-105	PSR J1833-1034	3.4e+37	4.85	4.7±0.4	(31)	Y
HESS J1837-069	PSR J1838-0655	5.5e+36	2.23	6.6 ± 0.9	(32)	N
HESS J1841-055	PSR J1838-0537	5.9e+36	4.97	1.3 <sup>b</sup>	(33)	Y
HESS J1846-029	PSR J1846-0258	8.1e+36	0.73	5.1 <sup>b</sup>	(12)	N
HESS J1848-018	...	...	...	6 <sup>d</sup>	(34)	N
HESS J1849-000	PSR J1849-0001	9.8e+36	42.9	7 <sup>d</sup>	(35)	N
HESS J1857+026	PSR J1856+0245	4.6e+36	20.6	9.0±1.2 <sup>f</sup>	(12)	N
MGRO J1908+06	PSR J1907+0602	2.8e+36	19.5	3.2 ± 0.3	(36)	Y
HESS J1912+101	PSR J1913+1011	2.9e+36	169	4.8 $^{+0.5}_{-0.7}$ f	(12)	N
VER J1930+188	PSR J1930+1852	1.2e+37	2.89	9 $^{+7}_{-2}$ 1 <sup>f</sup>	(37)	N
MGRO J1958+2848	PSR J1958+2846	3.4e+35	21.7	...	(12)	Y
VER J1959+208	PSR J1959+2048	1.6e+35	...	2.5 ± 0.1	(38, 39)	Y
MGRO J2019+37	PSR J2021+3651	3.4e+36	17.2	10 $^{+2}_{-4}$	(40, 41)	Y
MGRO J2228+61	PSR J2229+6114	2.2e+37	10.5	0.8±0.2	(42, 43)	Y

a- SNR distance.

b- Pseudo distance based on the observed correlation between the 0.1 – 100 GeV  $\gamma$ -ray luminosity and  $\dot{E}$  (Saz Parkinson et al. 2010). This relation suffers various caveats which translates to large uncertainties in the derived distance value and is therefore replaced by a conservative upper limit in 2PC.

c- Sedov model, see (31).

d- No available uncertainty given in the reference.

e- Relation between the hydrogen column density ( $N_H$ ) and E(B-V) and between E(B-V) and the distance.

f- Distance estimated using the pulsar dispersion measure and the NE2001 model (Cordes & Lazio 2002) which is available as off-line code as done in 2PC. To estimate the distance errors we apply a 20% Dispersion Measure uncertainty as is used in the online DM-distance estimator tool.

g- X-ray vs spin-down luminosity correlation, see (41).

h- Distance derived from HI absorption.

i- Sedov age, see (16).

has been detected but the parameters of an assumed pulsar can be estimated. Columns 3, 4, and 5 show the pulsar’s spin down power, characteristic age and distance respectively. Footnotes indicate cases when the distance is not estimated from the pulsar dispersion measure or cases when the age estimate is not the pulsar’s characteristic age. Column 7 says if the pulsar has been detected in  $\gamma$ -rays: “Y” means that it has and “N” means that it has not according to 2PC.

References: (1) Pineault et al. (1993), (2) Trimble (1973), (3) Weltevrede et al. (2010), (4) Verbiest et al. (2012), (5) Dodson et al. (2003), (6) Camilo et al. (2001), (7) Ruiz & May (1986), (8) Saz Parkinson et al. (2010), (9) Keith et al. (2008), (10) Caswell et al. (2004), (11) H.E.S.S. Collaboration et al. (2012b), (12) Manchester et al. (2005a), (13) Lorimer et al. (2006), (14) Yadigaroglu & Romani (1997), (15) Kishishita et al. (2012), (16) de los Reyes et al. (2012), (17) Seward et al. (1996), (18) Sun et al. (1999), (19) Temim et al. (2009), (20) Balbo et al. (2010), (21) Manchester et al. (2005b), (22) Funk et al. (2007a), (23) Lemièrè et al. (2009), (24) Kramer et al. (2003), (25) Johnston et al. (1995), (26) Manchester et al. (2001), (27) Funk et al. (2007b), (28) Hofverberg (2011), (29) Grondin et al. (2011), (30) Sheidaei (2011), (31) Camilo et al. (2006), (32) Gotthelf & Halpern (2008), (33) Pletsch et al. (2012), (34) Chaves et al. (2008), (35) Gotthelf et al. (2011), (36) Abdo et al. (2010d), (37) Leahy et al. (2008), (38) Guillemot et al. (2012), (39) Huang et al. (2012), (40) Yadigaroglu & Romani (1997), (41) Hessels et al. (2004), (42) Abdo et al. (2009c), (43) Kothes et al. (2001).

310 Table 7 summarizes the PSR/PWN systems’ characteristics such as the age or the  
 311 distance. The characteristic age of the pulsar is given by  $\tau_C = P/2\dot{P}$  where P is the pulsar’s  
 312 rotational period. This formula is obtained assuming that the pulsar is a dipole and that the  
 313 initial period of the pulsar is negligible compared to its current value. The putative pulsars  
 314 powering HESS J1554–550, HESS J1632–478, HESS J1640–465, HESS J1818–154 and  
 315 HESS J1848–018 are not yet detected. However, Table 7 gives the system age or distance  
 316 estimated using another method than the pulsar dispersion measure, e.g. distance measure  
 317 derived by H<sub>I</sub> absorption or using a statistical relation between the hydrogen column density  
 318 ( $N_H$ ) and E(B–V) (Ryter et al. 1975) and a relation between E(B–V) and the distance  
 319 (Lucke 1978).

#### 320 4.1. Spatial Results

321 Assigning an association between a LAT source and an VHE source depends on two  
 322 considerations: the spatial and spectral consistency with the counterpart. Spatial consistency  
 323 has two aspects: centroid coincidence and extension compatibility. For assessing the degree  
 324 of spatial coincidence, we considered a LAT emission to be spatially coincident with the  
 325 VHE source if the distance between the LAT and VHE experiments best-fit positions was  
 326 inside a circle whose radius is the quadratic sum of: 1) the 68% c.l. uncertainty on the  
 327 LAT best-fit position, 2) the 68% c.l. position uncertainty of the VHE source, and 3) the  
 328 99% containment radius of the source based on the VHE fitted angular extent. These data  
 329 are summarized in Table 8. Only one source is not spatially coincident using this criterion:  
 330 HESS J1018–589. We removed from this table the sources likely to be associated to pulsar  
 331 emission. These sources will be discussed in Section 4.2.

332 Although VER J2016+372 is spatially extended as announced in Aliu (2011), neither  
 333 the extension nor the uncertainties of the spatial parameters are yet available. There is little  
 334 doubt that these parameters will show that the VERITAS and LAT emission are spatially  
 335 coincident. This case will be discussed in Section 4.4.

336 A finite measured extension of a  $\gamma$ -ray source is a direct way to discriminate be-  
 337 tween a pulsar and a PWN. Therefore, we searched for significant angular extensions of  
 338 the LAT sources. Of the 21 sources not labeled as PSR in Section 4.2, eight are signifi-  
 339 cantly extended: HESS J1303–631, HESS J1614–518, HESS J1616–508, HESS J1632–478,  
 340 HESS J1804–216, HESS J1825–137, HESS J1837–069 and HESS J1841–055. Six of them  
 341 were already detected by Lande et al. (2012). Only HESS J1632–478 has an extension in-  
 342 consistent with that work. For this source, Lande et al. (2012) measured an extension of

Table 8. Comparison between the LAT and VHE positions.

Name	Unc <sub>GeV</sub> (deg)	Unc <sub>TeV</sub> (deg)	$r_{99\%}$ TeV (deg)	Distance (deg)
HESS J1018–589	0.04	0.02	0.00	0.12
HESS J1023–575	0.04	0.09	0.55	0.10
HESS J1119–614	0.05	...	0.15	0.09
HESS J1303–631	0.05	0.01	0.49	0.41
HESS J1356–645	0.05	0.03	0.61	0.19
HESS J1420–607	0.04	0.02	0.18	0.01
HESS J1507–622	0.06	0.04	0.46	0.21
HESS J1514–591	0.03	0.07	0.23	0.06
HESS J1614–518	0.05	0.03	0.58	0.19
HESS J1616–508	0.04	0.01	0.42	0.16
HESS J1632–478	0.04	0.04	0.41	0.15
HESS J1634–472	0.03	0.05	0.33	0.18
HESS J1640–465	0.05	0.01	0.12	0.07
HESS J1804–216	0.04	0.02	0.65	0.06
HESS J1825–137	0.06	0.03	0.38	0.28
HESS J1834–087	0.05	0.02	0.27	0.06
HESS J1837–069	0.06	0.02	0.26	0.12
HESS J1841–055	0.06	0.05	1.00	0.22
HESS J1848–018	0.04	...	0.97	0.11
HESS J1857+026	0.04	0.05	0.29	0.14
VER J2016+372	0.05	...	...	0.11

Note. — Comparison of the localization and localization uncertainty for the sources observed at LAT and VHE energies and classified as “PWN”, “PWNC” or “O”. Columns 2, 3, 4 and 5 respectively give the averaged uncertainty on the position obtained using *Fermi*-LAT data and assuming a point source if  $TS_{\text{ext}} < 16$  or a Gaussian if  $TS_{\text{ext}} > 16$ , the quadratic sum of the statistical (68% confidence radius) and systematic uncertainties on the VHE position given in Table 1, the 99% containment radius of the VHE emission assuming the extension listed in Table 1 and the distance between the position of the source fit at LAT and VHE energies.

343 ( $0^{\circ}35 \pm 0^{\circ}06$ ) assuming a disk, while we obtained ( $0^{\circ}30 \pm 0^{\circ}04$ ) for a Gaussian. Compari-  
 344 son between 68% containment radius of a disk and a Gaussian yields  $\sigma_{Disk} \sim 1.84\sigma_{Gaussian}$   
 345 (Lande et al. 2012), where  $\sigma_{Disk}$  and  $\sigma_{Gaussian}$  respectively represent the disk radius and  
 346 the Gaussian standard deviation. Therefore, for HESS J1632–478, our analysis led to an  
 347 extension bigger than that obtained in Lande et al. (2012). This difference certainly comes  
 348 from the three additional 2FGL sources (2FGL J1631.7–4720c, 2FGL J1630.2–4752 and  
 349 2FGL J1632.4–4820c) included in the model used by Lande et al. (2012). These sources  
 350 are not included in the 1FHL catalog and are below the pre-defined TS >25 threshold for  
 351 additional sources. Since they are unidentified, we chose to not add them.

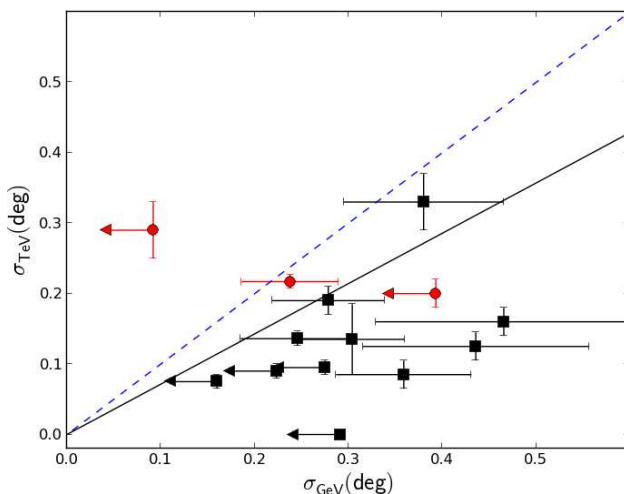


Fig. 2.— Comparison of the sizes of the sources observed at LAT and VHE energies. Contributions of pulsars listed in Table 2 were taken into account by modeling them as point sources with spectral parameters fixed at their values in the 2FGL catalog. For sources not significantly extended at LAT energies, a 99% c.l. upper limit on the extension is shown. The red circles represent the sources within  $0^{\circ}5$  of a  $\gamma$ -ray pulsar and the black squares represent the other sources. This plot shows a zoom on  $\sigma_{TeV}$  and  $\sigma_{GeV} \in [0^{\circ}, 0^{\circ}6]$ . The dashed line shows  $\sigma_{TeV} = \sigma_{GeV}$ . The solid line shows the  $\sigma_{GeV} = 1.4 \times \sigma_{TeV}$  fit result (see Section 4.1).

352 Figure 2 compares the sizes measured by the LAT and VHE. The only source with  
 353  $\sigma_{GeV} < \sigma_{TeV}$  is HESS J1708–443 whose LAT emission is likely coming from the pulsar. As  
 354 we discussed above and in Section 4.5, we suspect that the extensions of HESS J1303–631  
 355 and HESS J1632–478 are overestimated. We assumed a linear relation between the VHE  
 356 experiment and the LAT extension ( $\sigma_{GeV} = \alpha \times \sigma_{TeV}$ ) and fit the data points, obtaining  
 357  $\alpha = 1.4 \pm 0.2$  with a  $\chi^2/\text{d.o.f.} = 15/7$ . In the case in which we fixed  $\alpha = 1$  we obtained  
 358 a  $\chi^2/\text{d.o.f.} = 24/8$ . This implies that, with the current statistics, the LAT extension is  
 359 larger than the one measured by VHE experiments at the  $2.8\sigma$  level. Additional expo-

360 sure and a more precise analysis of crowded regions (e.g. the regions of HESS J1303–631,  
 361 HESS J1632–478, HESS J1837–069 or HESS J1841–055) are needed to draw any conclu-  
 362 sion. Indeed, in these regions the  $\gamma$ -ray emission could be due to more than one source,  
 363 as discussed below in the case of HESS J1841–055 or as discussed in Gotthelf & Halpern  
 364 (2008) for the case of HESS J1837–069.

## 365 4.2. Pulsars Detected Above 10 GeV

366 In the LAT energy range, 22 sources are found to be point-like, i.e. not significantly  
 367 extended. Table 5 demonstrates that among these 22 point-like sources, nine have a  
 368 soft spectral index ( $\Gamma > 3$ ): HESS J1418–609, HESS J1708–443, MGRO J0632+17,  
 369 MGRO J1908+06, MGRO J1958+2848, MGRO J2019+37, MGRO J2228+61,  
 370 MGRO J2031+41B and VER J0006+727. Tables 2 and 9 demonstrate that all of  
 371 them are located close to a LAT-detected pulsar. Table 5 shows that their  $\gamma$ -ray emission  
 372 significantly decreases when the contribution of the associated LAT-detected pulsar is  
 373 included. Furthermore, the spectra obtained above 10 GeV for these sources agree with the  
 374 nearby pulsars’ spectra given in the 2FGL catalog as shown in Figures 3, 4, 5 and 6. These  
 375 figures only show SEDs for sources with no X-ray and radio information available. The  
 376 spectra for the other sources will be discussed in Section 4.5.

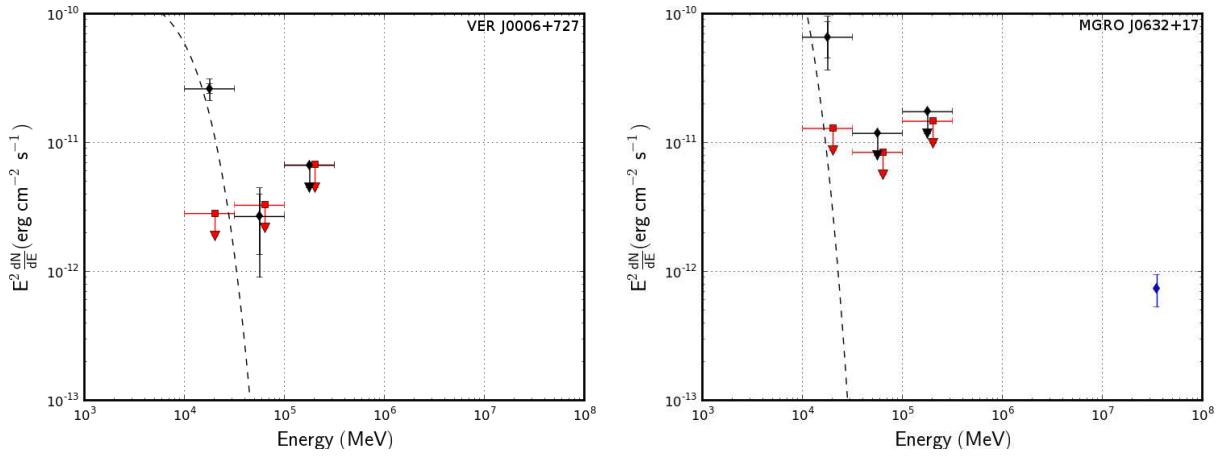


Fig. 3.— Multi-wavelength SEDs of VER J0006+727 and MGRO J0632+17. The black diamonds represent the SED of the source obtained at LAT energies. For sources with an associated LAT-detected pulsar, the red squares represent the SED with any potential emission from the LAT-detected pulsar subtracted using the spectral parameters from the 2FGL catalog. To enhance readability, we offset the square markers in energy by a factor of 13%. Finally, the blue diamond markers represent the SED obtained by VHE experiments. Table 2 lists the references for the VHE SED of each source. For sources with an associated LAT-detected pulsar, the best-fit spectrum of the pulsar from 2FGL is included as a dashed line.

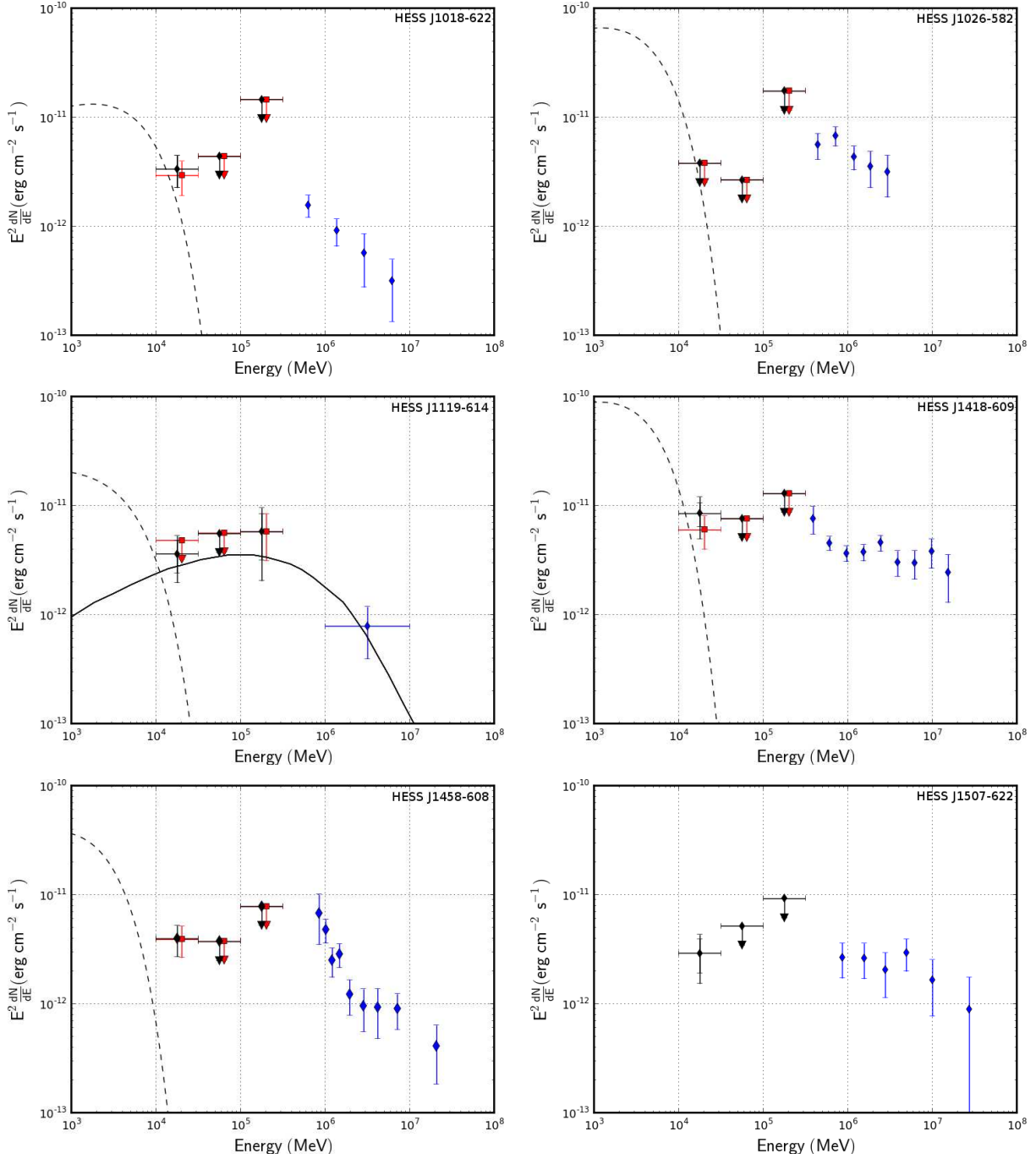


Fig. 4.— The LAT and VHE SEDs of HESS J1018–589, HESS J1119–614, HESS J1418–609, HESS J1458–608 and HESS J1507–622 following conventions of Figure 3. The solid line corresponds to the model proposed by Mayer (2010) for HESS J1119–614. In the case of HESS J1119–614, the spectral point has been computed using the integral flux given in (Kargaltsev & Pavlov 2010, see Section 4.5 for details). The horizontal error bars show the energy range of the used integral flux.

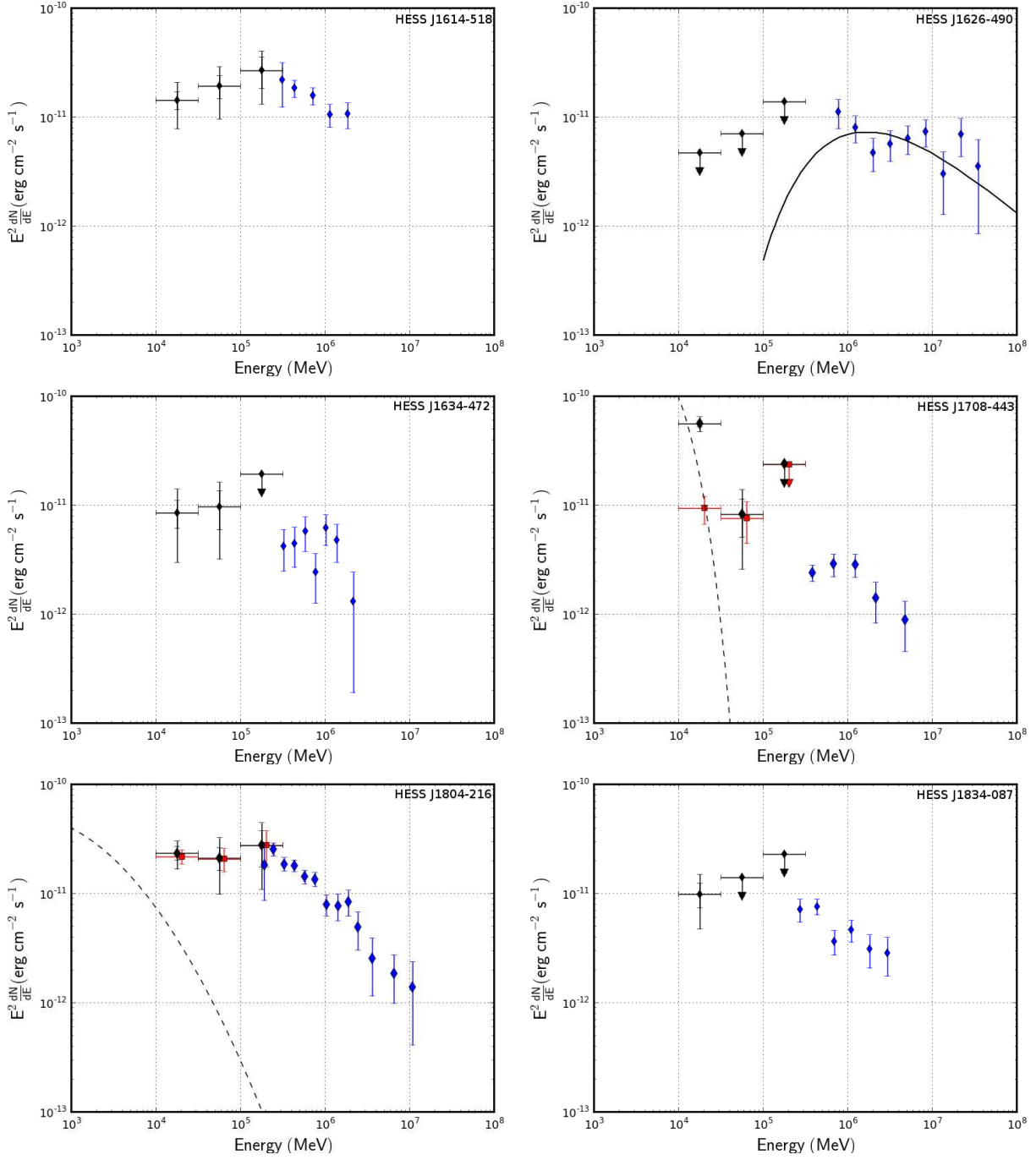


Fig. 5.— The LAT and VHE SEDs of HESS J1614–518, HESS J1626–490, HESS J1634–472, HESS J1708–443, HESS J1804–216 and HESS J1834–087 following the conventions of Figure 3. The solid line corresponds to the model proposed by Eger (2011) for HESS J1626–490.

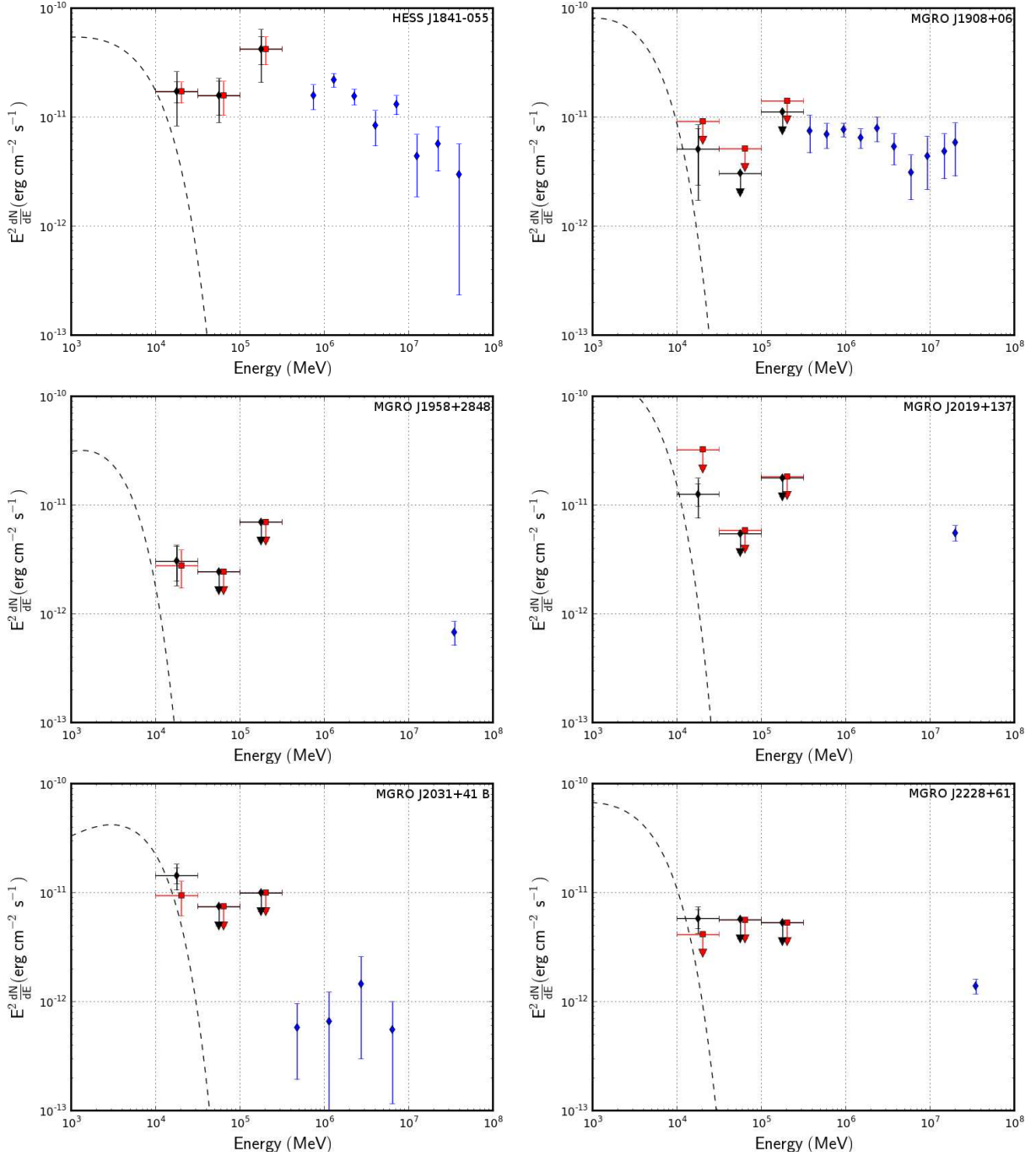


Fig. 6.— The LAT and VHE SEDs of HESS J1841–055, MGRO J1908+06, MGRO J1958+2848, MGRO J2019+137, MGRO J2031+41B and MGRO J2228+61 following the conventions of Figure 3.

377 To study the contamination of the LAT data for the VHE sources by these pulsars, we  
 378 accounted for the pulsar contribution to photons in the region as explained in Section 3.2.  
 379 Tables 4 and 5 and Figures 3, 4, 5 and 6 show the results of this new fit using the 2FGL  
 380 models of the pulsars. For these nine sources, in Figures 3, 4, 5 and 6 the low-energy part  
 381 of the emission ( $<30$  GeV) tends to disappear, suggesting that we primarily detected pulsar  
 382 emission. For these reasons, we infer that the observed LAT emission coming from these  
 383 sources is likely due to the pulsars themselves. We labeled these nine sources as “PSR” in  
 384 Table 4.

### 385 4.3. PWNe and PWNe Candidates

386 The hardness of the  $\gamma$ -ray spectrum and the presence of a pulsar energetic enough to  
 387 power a potential PWN are important criteria for source classification as a PWN. In addition  
 388 to these criteria, to label a source as a “PWN” or a “PWNe” for PWN candidate, we  
 389 required that its LAT spectrum connects with the VHE spectrum, i.e. that the differential  
 390 fluxes at the highest LAT energies and in the VHE low energy range be approximately  
 391 equivalent, such that they can be interpreted as a continuous multi-wavelength spectrum. An  
 392 exception has been made for HESS J1848–018, which is classified as “PWNe” as explained  
 393 in Section 4.5.6. Based on multi-wavelength analyses, we labeled 3 sources as “PWN”:  
 394 HESS J1356–645, HESS J1514–591 and HESS J1825–137. HESS J1356–645 is considered  
 395 as “PWN” based upon the morphology of the source observed in the radio and X-ray domain  
 396 (H.E.S.S. Collaboration et al. 2011d). HESS J1514–591 is considered as a “PWN” because  
 397 of the correlation observed between the H.E.S.S. and X-ray emissions and the observation  
 398 of pulsar jets in the X-ray domain (Aharonian et al. 2005b). And finally, HESS J1825–137  
 399 is considered to be a “PWN” since Aharonian et al. (2006b) have shown that it has an  
 400 energy-dependent morphology in the H.E.S.S. energy range.

401 Detections of 7 of the PWNe candidates have been previously published.  
 402 For HESS J1023–575 (Ackermann et al. 2011), HESS J1640–465 (Slane et al. 2010),  
 403 HESS J1857+026 (Rousseau et al. 2012), HESS J1616–508, HESS J1632–478 and  
 404 HESS J1837–069 (Lande et al. 2012) and HESS J1848–018 (Tam et al. 2010), the LAT  
 405 emission has been discussed in previous work and proposed to be of PWN origin.

406 We detected 4 new PWNe candidates (HESS J1119–614, HESS J1303–631,  
 407 HESS J1420–607 and HESS J1841–055) and 1 new PWN (HESS J1356–645). These sources  
 408 are spatially consistent with pulsars able to power them (respectively PSR J1119–6127,  
 409 PSR J1301–6305, PSR J1420–6048, PSR J1838–0537 and PSR J1357–6429). Moreover,  
 410 their LAT emissions are best modeled by hard spectra and are compatible with the VHE

Table 9. Comparison between the LAT emission and pulsar positions.

Name	Unc <sub>GeV</sub> (arcmin)	Unc <sub>PSR</sub> (arcmin)	distance (arcmin)
VER J0006+727	1.2	0.4	1.2
MGRO J0632+17	0.6	0.2	0.6
HESS J1418–609	1.8	0.8	2.0
HESS J1708–443	0.6	0.3	0.6
MGRO J1908+06	2.4	0.8	2.5
MGRO J1958+2848	2.4	1.1	1.2
MGRO J2019+37	1.8	0.5	1.2
MGRO J2031+41B	3.6	0.8	1.2
MGRO J2228+61	1.8	0.6	0.6

Note. — For the nine sources classified as "PSR", a comparison of the localization of the source in the 10 GeV to 316 GeV energy range with the localization in 2FGL from 100 MeV to 100 GeV. Columns 2, 3 and 4 respectively give the 68% uncertainty on the point source position obtained in this work, the averaged 68% uncertainty on the 2FGL position and the distance between the 2FGL position and the position obtained in this work. The average on the 2FGL position uncertainty is obtained as  $\sqrt{a \times b}$  where  $a$  and  $b$  are the length of the semi-minor and semi-major axes of the 68% confidence ellipse defined in 2FGL.

411 SEDs. The new LAT sources and PWNe candidates are described in Section 4.5.

412

#### 4.4. “O”-Type Sources

413

414

415

416

The 7 sources that cannot be associated to a PWN or a pulsar are labeled ”O” for Other. These sources cannot be associated because either no sufficiently energetic pulsar is known at that location or the spectral connection from the LAT to the VHE measurements does not support a PWN interpretation.

417

418

419

420

421

422

423

424

425

426

427

3 sources have relatively hard spectra at LAT energies that connect spectrally to the associated VHE source: HESS J1614–518, HESS J1634–472 and HESS J1804–216. These sources are not classified as PWNe due to previous multi-wavelength analyses. The former is spatially coincident with 5 detected pulsars, but none is luminous enough to power a PWN that would explain the  $\gamma$ -ray emission (Rowell et al. 2008). Sakai et al. (2011) found two X-ray counterparts to the H.E.S.S. source and proposed an SNR identification. As discussed in Lande et al. (2012), the nature of the source remains unclear. HESS J1634–472 does not have any counterpart pulsars energetic enough to power it. Finally, Ajello et al. (2012) studied the link between the H.E.S.S. and the LAT emission coming from the region of HESS J1804–216 and concluded that the emission is more likely due to the energy-dependent scattering of particles accelerated in a SNR than to a PWN.

428

429

430

431

432

433

434

435

436

437

438

439

440

The remaining 4 sources are HESS J1018–589, HESS J1507–622, HESS J1834–087 and VER J2016+372. In the LAT energy range, they are point-like with relatively soft spectra ( $3 > \Gamma > 2$ ). Therefore, the association of the LAT emission with their VHE counterparts is uncertain. HESS J1018–589 is close to both the  $\gamma$ -ray binary 1FGL J1018.6–5856 (Coe et al. 2012) and the nearby SNR G284.3–1.8. The LAT source appears to be spatially coincident with SNR G284.3–1.8. SNR G284.3–1.8 is not included in our list of candidates and will be analyzed in the SNR catalog. Domainko & Ohm (2012) were not able to conclusively determine the origin of the  $\gamma$ -ray emission of HESS J1507–622 and confirm the result of H.E.S.S. Collaboration et al. (2011c): a leptonic scenario seems favored, while a hadronic one seems unlikely. HESS J1834–087 and VER J2016+372 lack a pulsar energetic enough to power their emission. But Albert et al. (2006b) have suggested that the interaction of SNR W41 with a nearby molecular cloud could explain HESS J1834–087. Another analysis of LAT and H.E.S.S. observations of HESS J1834–087 will be presented elsewhere.

441 **4.5. Descriptions of New LAT PWNe Candidates**

442 In this section, we compare source spectra with previously published models (the ref-  
 443 erences to those models are provided below for each case). We do not refit those models  
 444 incorporating the LAT data. Therefore, disagreements between the published models and  
 445 the LAT data do not necessarily imply that the models are ruled out as it may be possible  
 446 to accommodate our results under these models with a different set of parameters.

447 *4.5.1. HESS J1119–614*

448 During the Parkes multibeam pulsar survey, Camilo et al. (2000) discovered  
 449 PSR J1119–6127, a young ( $\tau_C = 1.6$  kyr) pulsar with a high spin-down power  $\dot{E} =$   
 450  $2.3 \times 10^{36}$  erg s $^{-1}$  within the composite SNR G292.2–0.5. This pulsar was also detected by  
 451 the LAT (Parent et al. 2011). Using *Chandra* observations, Gonzalez & Safi-Harb (2003) and  
 452 Safi-Harb & Kumar (2008) reported the presence of a faint and compact PWN close to this  
 453 pulsar. More recently, a H.E.S.S. source coincident with PSR J1119–6127 and G292.2–0.5  
 454 was announced<sup>5</sup>.

455 Using the method described above, a signal is detected at the position of  
 456 HESS J1119–614 with a TS of 27 ( $4.9\sigma$  with two d.o.f.). Nevertheless, as can be seen  
 457 on Figure 4 and in Table 5, the spectrum is contaminated by a low-energy component asso-  
 458 ciated with PSR J1119–6127. We assess the contamination from the pulsar by subtracting  
 459 the emission from 2FGL J1118.8–6128 associated with PSR J1119–6127. This decreases the  
 460 significance of the detection to TS=16 ( $3.6\sigma$  with 2 d.o.f.), which is just above the thresh-  
 461 old from Section 3.3. Subtracting the pulsar emission affects the spectrum of our source  
 462 by making it harder and changing the lowest energy point to become an upper limit (see  
 463 Figure 4).

464 Figure 4 shows the SED of HESS J1119–614. Because only an integral flux between 1  
 465 and 10 TeV is available for this source (Kargaltsev & Pavlov 2010), we computed a spectral  
 466 point at 3.16 TeV assuming a fiducial spectral index of 2.4 in the H.E.S.S. energy range.  
 467 We represented this point on the figure. The leptonic model proposed by Mayer (2010) is  
 468 a one-zone model in which accelerated electrons cool radiatively by IC scattering on CMB  
 469 photons, stellar photons from the vicinity and photons radiated by dust, and by synchrotron  
 470 losses. It implies an initial period of the pulsar  $P_0 = 21.4$  ms, an initial magnetic field inside  
 471 the PWN  $B_0 \sim 400 \mu\text{G}$  (leading to a current magnetic field of  $B \sim 32 \mu\text{G}$ ), a braking index of

---

<sup>5</sup>[http://cxc.harvard.edu/cdo/snr09/pres/DjannatiAtai\\_Arache\\_v2.pdf](http://cxc.harvard.edu/cdo/snr09/pres/DjannatiAtai_Arache_v2.pdf)

472  $n = 2.91$  (Camilo et al. 2000) and a conversion efficiency of rotational energy into relativistic  
 473 particles of  $\eta = 0.3$ . The leptonic model matches the new LAT data points.

474 The energetics of PSR J1119–6127, the detection of a compact PWN in X-rays and the  
 475 leptonic model proposed by Mayer (2010) support the hypothesis in which the LAT-H.E.S.S.  
 476 emission originates in the PWN inside G292.2–0.5. Furthermore, the parameters derived in  
 477 Mayer (2010) and the jet-like morphology in the X-ray data are reminiscent of the case of  
 478 MSH 15–52 (Abdo et al. 2010a; Tamura et al. 1996).

#### 479 4.5.2. HESS J1303–631

480 HESS J1303–631 was serendipitously discovered in 2004 (Aharonian et al. 2005c) dur-  
 481 ing an observation campaign of the binary system PSR B1259–63. It is the first H.E.S.S.  
 482 source classified as a UNID due to the lack of detected counterparts in radio and X-rays with  
 483 *Chandra* (Mukherjee & Halpern 2005). H.E.S.S. Collaboration et al. (2012b) found only one  
 484 plausible counterpart in the vicinity of HESS J1303–631: PSR J1301–6305 with a spin down  
 485 power of  $\dot{E} = 1.70 \times 10^{36} \text{ erg s}^{-1}$ . The authors also presented the detection of a very weak  
 486 X-ray PWN using *XMM-Newton* observations. This, with the energy dependent morphology  
 487 observed by H.E.S.S. led to the conclusion that HESS J1303–631 is an old PWN offset from  
 488 the pulsar powering it.

489 Wu et al. (2011) found no significant emission from HESS J1303–631 using 30 months  
 490 of *Fermi*-LAT data between 1 and 20 GeV. With 15 months of additional data and a higher  
 491 energy threshold, our analysis now provides a first detection of LAT emission coincident  
 492 with the HESS source. Nevertheless, Figure 7 shows that the detected emission might be  
 493 contaminated by  $\gamma$ -ray emission from the nearby SNR Kes 17. Since we cannot separate  
 494 these two sources using our strategy with the current statistics, we decided to include the  
 495 effect of source confusion in our estimate of systematic uncertainties for HESS J1303–631.  
 496 Therefore, we ran the analysis again, adding a source at the position of Kes 17. We quantify  
 497 the systematic error as the differences in parameter values resulting from fitting with the  
 498 two background models. The maximal variation is in the lowest energy bin of the SED.

499 For our best LAT morphology of a Gaussian of dispersion  $0^\circ.45$  (see Table 4), we obtained  
 500 an index of  $\Gamma = 1.71 \pm 0.26 \pm 0.37$  (we obtained  $\Gamma = 1.53 \pm 0.23 \pm 0.37$  assuming the H.E.S.S.  
 501 best fit Gaussian, Table 5). This hard index is in the range of values obtained for LAT  
 502 detected PWNe and is inconsistent with the spectral index of  $\sim 2.4$  derived by Wu et al.  
 503 (2011) for Kes 17. This is an evidence that the  $\gamma$ -ray emission above 10 GeV is dominated  
 504 by the PWNe candidate. As can be seen in Figure 8, even though the connection between

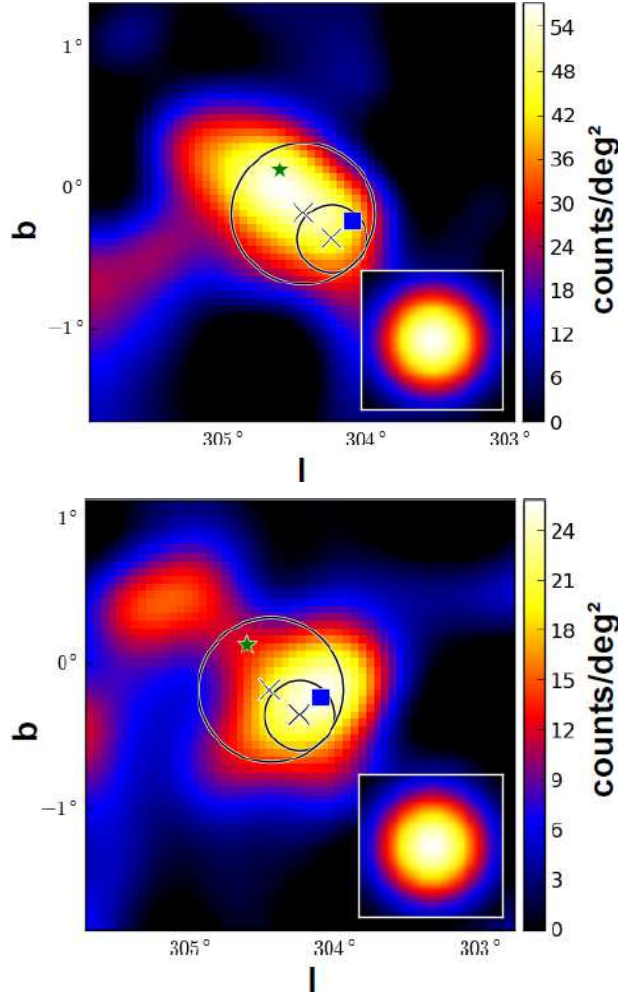


Fig. 7.— Count map of the region of HESS J1303–631 above 10 GeV (top) and above 31 GeV (bottom). We subtracted the Galactic and isotropic diffuse emission. The count map is smoothed by a Gaussian of  $0^{\circ}27$  corresponding to the PSF above 10 GeV. The green star indicates the position of the SNR Kes 17 and the blue square represents the position of PSR J1301–6305. The small and big circles respectively show the extension of the H.E.S.S. Gaussian proposed by Aharonian et al. (2005c) and the extension of the Gaussian derived in this work. The lower right inset is the model predicted emission from a point-like source with the same spectrum as HESS J1303–631 smoothed by the same kernel.

505 the LAT and the H.E.S.S. energy range is not perfect, LAT and H.E.S.S. spectra are not  
 506 inconsistent, suggesting a potential physical relationship.

507 Figure 8 shows the SED of HESS J1303–631 together with the one-zone leptonic model  
 508 proposed by H.E.S.S. Collaboration et al. (2012b). In this model, VHE  $\gamma$ -rays are created

509 via IC scattering of electrons on the CMB photons. Infrared and optical target photons  
 510 are neglected. The model reproduces the radio, X-ray and H.E.S.S. data with an electron  
 511 spectral index of  $1.8 \pm 0.1$ , a cut-off energy of  $31_{-4}^{+5}$  TeV, and an average magnetic field of  
 512  $1.4 \pm 0.2 \mu\text{G}$ . However, the flux predicted in the LAT energy range is well below the flux  
 513 detected by the *Fermi*-LAT. This may be due to the absence of infrared and optical photon  
 514 fields in the model described above or to the contamination produced by Kes 17. A specific  
 515 analysis is needed to make conclusions about the constraints that the *Fermi*-LAT could yield  
 516 on the  $\gamma$ -ray emission of this source.

#### 517 4.5.3. *HESS J1356–645*

518 HESS J1356–645 is an extended source detected by H.E.S.S. during the Galactic Plane  
 519 Survey (H.E.S.S. Collaboration et al. 2011d). It lies close to the pulsar PSR J1357–6429  
 520 discovered during the Parkes multibeam survey of the Galactic Plane (Camilo et al.  
 521 2004). Its high spin-down power of  $\dot{E} = 3.1 \times 10^{36} \text{ erg s}^{-1}$  makes it a good candidate  
 522 to power a PWN. Analysis of archival radio and X-ray data from *ROSAT/PSPC* and  
 523 *XMM/Newton* have revealed a faint extended structure coincident with the VHE emis-  
 524 sion (H.E.S.S. Collaboration et al. 2011d) providing another argument in favor of the PWN  
 525 scenario. In parallel, Lemoine-Goumard et al. (2011b) announced the detection of a pulsed  
 526 signal from PSR J1357–6429 in the  $\gamma$ -ray and X-ray energy ranges using *Fermi*-LAT and  
 527 *XMM-Newton* data. However, using 29 months of LAT data between 0.1 and 100 GeV, no  
 528 counterpart to the H.E.S.S. emission was found in the off-pulse window of the pulsar.

529 The 16 additional months of observations by *Fermi*-LAT and the higher maximum  
 530 energy used (316 GeV instead of 100 GeV) in our dataset now enables the detection of a  
 531 faint counterpart to the H.E.S.S. emission with a  $\text{TS} = 24$  ( $4.7\sigma$  assuming two d.o.f.).

532 With its spectral cutoff at low energy,  $\sim 800 \text{ MeV}$  (Lemoine-Goumard et al. 2011b),  
 533 PSR J1357–6429 is not significant in the 10 GeV to 316 GeV energy range. Therefore, we  
 534 do not expect to see any changes in the spectral parameters when adding PSR J1357–6429  
 535 to the model of the region. This is verified in Table 5 as well as in Figure 8.

536 The combined LAT-H.E.S.S. data in Figure 8 provide new information concerning the  
 537 spectral shape of the  $\gamma$ -ray emission. The spatial and spectral consistency between the LAT  
 538 and H.E.S.S. emission suggests a physical relationship, leading to the assumption that the  
 539 LAT and the H.E.S.S. emission are due to the same object. Assuming that the  $\gamma$ -ray signal  
 540 comes from the PWN powered by PSR J1357–6429, H.E.S.S. Collaboration et al. (2011d)  
 541 proposed a leptonic scenario (black curve) which provides an excellent fit of the new multi-

542 wavelength data. This one-zone model is based on the evolution of an electron population  
 543 injected with an exponentially cutoff power-law spectrum of index 2.5 and cut-off energy  
 544 of 350 TeV. These electrons cool radiatively through IC scattering on the CMB, Galactic  
 545 infrared ( $T \sim 35$  K and 350 K) and optical ( $T \sim 4600$  K) photons and through synchrotron  
 546 emission in a magnetic field  $\sim 3.5 \mu\text{G}$ .

547 The similarities between PSR J1357–6429 and the Vela pulsar and between their PWNe  
 548 led H.E.S.S. Collaboration et al. (2011d) to discuss two leptonic emission components. In  
 549 the case of Vela–X, the “halo” is seen in the LAT and radio energy ranges and the “cocoon”  
 550 in the H.E.S.S. and X-ray energy ranges, while in the case of HESS J1356–645, a single  
 551 lepton population explains the broad-band spectrum with reasonable parameters. Unlike  
 552 Vela–X, PSR J1357–6429 is very faint in radio and X-ray, and observations in these bands  
 553 do not provide morphological constraints. Future multi-wavelength data are greatly needed  
 554 to better describe this source.

#### 555 4.5.4. HESS J1420–607

556 The complex of compact and extended radio/X-ray sources, called Kook-  
 557 aburra (Roberts et al. 1999), spans over one square degree along the Galactic Plane. It has  
 558 been extensively studied to explain the EGRET source 3EG J1420–6038/GEV J1417–6100  
 559 (Hartman et al. 1999; Lamb & Macomb 1997). Within its North-East excess, designated  
 560 ‘K3’, the young and energetic pulsar PSR J1420–6048 with period 68 ms, characteristic age  
 561  $\tau_C = 13$  kyr, and spin down power  $10^{37} \text{ erg s}^{-1}$  was discovered (D’Amico et al. 2001). X-ray  
 562 observations by *ASCA* and later by *Chandra* and *XMM-Newton* revealed extended X-ray  
 563 emission surrounding this pulsar and identified as a potential PWN (Roberts et al. 2001;  
 564 Ng et al. 2005). On the South-West side of the Kookaburra complex lies a bright nebula ex-  
 565 hibiting extended hard X-ray emission, G313.1+0.1 (aka the “Rabbit”, Roberts et al. 1999).  
 566 This X-ray excess was also proposed as a PWN contributing to the  $\gamma$ -ray emission detected  
 567 by EGRET.

568 The H.E.S.S. Galactic Plane survey revealed two VHE sources in this region:  
 569 HESS J1420–607 and HESS J1418–609 (Aharonian et al. 2006a). HESS J1420–607  
 570 is centered north of PSR J1420–6048 (near K3), while HESS J1418–609 is coincident  
 571 with the Rabbit nebula. More recently, *Fermi*-LAT detected pulsed  $\gamma$ -ray emission from  
 572 PSR J1420–6048 and PSR J1418–6058, the latter being a new  $\gamma$ -ray pulsar found through  
 573 blind frequency searches (Abdo et al. 2010e, 2009a). PSR J1418–6058 is coincident with  
 574 an X-ray source in the Rabbit PWN and has a spin-down power high enough to power the  
 575 PWN candidate HESS J1418–609.

576 Figure 9 shows two smoothed count maps centered on the location of the K3 nebula.  
 577 The Galactic and the isotropic diffuse emission were subtracted to show the excesses com-  
 578 ing from HESS J1420–607 and HESS J1418–609. Above 10 GeV, HESS J1418–609 and  
 579 HESS J1420–607 are confused, due to the size of the LAT PSF and to the limited statistics.  
 580 However, on the count map above 31 GeV, the emission from HESS J1418–609 disappears,  
 581 confirming the soft spectrum and the pulsar-like emission coming from HESS J1418–609  
 582 and the harder spectrum of HESS J1420–607.

583 Van Etten & Romani (2010) used a two-zone time dependent numerical model with  
 584 constant injection luminosity to investigate the physical properties of HESS J1420–607. The  
 585 authors injected relativistic particles following a power-law spectrum into the inner nebula  
 586 zone; they evolved this spectrum over time and injected the resultant spectrum into the  
 587 outer nebula zone. Figure 8 shows the results obtained for a hadronic + leptonic model on  
 588 the assumption of a low density environment ( $n \sim 1 \text{ cm}^{-3}$ ) and magnetic fields of  $12 \mu\text{G}$  and  
 589  $9 \mu\text{G}$  respectively in the inner and outer nebula. The same figure presents a leptonic scenario  
 590 assuming magnetic fields of  $12 \mu\text{G}$  and  $8 \mu\text{G}$  respectively in the inner and outer nebula. The  
 591 strength of this magnetic field implies a lepton spectral break at  $\sim 100 \text{ TeV}$  after evolution in  
 592 the inner nebula. More recently, Kishishita et al. (2012) proposed a one-zone leptonic model  
 593 assuming a power-law injection spectrum with an index of 2.3 with a cut-off at  $\sim 40 \text{ TeV}$  and  
 594 a magnetic field of  $\sim 3 \mu\text{G}$ ; the model SED is shown in the same figure.

595 As explained in Section 3, the model used for PSR J1420–6048 was fixed to the 2FGL  
 596 spectrum. Therefore, if this model does not perfectly reproduce the data with 21 additional  
 597 months, the LAT spectral points of HESS J1420–608 might still be contaminated by the  
 598 pulsar’s emission. With the current statistics, all models reproduce the LAT and H.E.S.S.  
 599 data reasonably well. A future off-pulse analysis of LAT data for this pulsar performed with  
 600 more statistics could help discriminate between the models.

#### 601 4.5.5. HESS J1841–055

602 HESS J1841–055 was discovered during the H.E.S.S. Galactic Plane Survey  
 603 (Aharonian et al. 2008c) and remained unidentified. The emission is highly extended  
 604 and shows possibly three peaks, and more than one possible counterparts, suggesting  
 605 that the H.E.S.S. emission is composed of more than one source. Using *INTEGRAL*  
 606 data, Sguera et al. (2009) proposed the high-mass X-ray binary system AX J1841.0–0536  
 607 as a potential counterpart, at least for part of the emission. Nolan et al. (2012) and  
 608 Neronov & Semikoz (2012) detected three sources coincident with HESS J1841–055. Tibolla  
 609 (2011) proposed the association of HESS J1841–055 to an ancient PWN powered by

610 PSR J1841–0524, PSR J1838–0549 or both as each pulsar taken independently would need  
 611 an efficiency greater than 100% to solely power a potential PWN associated with the H.E.S.S.  
 612 source. More recently, the blind search detection of the new  $\gamma$ -ray pulsar PSR J1838–0537  
 613 with *Fermi*-LAT provided another potential counterpart of the H.E.S.S. source. Indeed,  
 614 assuming a distance of 2 kpc, Pletsch et al. (2012) estimated that PSR J1838–0537 is suf-  
 615 ficiently energetic to power the whole H.E.S.S. source with a conversion efficiency of 0.5%,  
 616 similar to other suggested pulsar/PWN associations (Hessels et al. 2008).

617 In this work, HESS J1841–055 is detected as a significantly extended source ( $TS_{ext}=32$ )  
 618 at a position consistent with the H.E.S.S. source. The LAT extension of  $0^\circ.38 \pm 0^\circ.09$  compa-  
 619 rable with the  $0^\circ.33 \pm 0^\circ.04$  of the H.E.S.S. source.

620 As can be seen in Figure 6, the *Fermi*-LAT spectral points connect to the H.E.S.S. ones.  
 621 The spatial consistency and spectral connection between H.E.S.S. and LAT emissions suggest  
 622 a physical relationship. The hard *Fermi*-LAT spectrum detected implies that a curvature  
 623 must arise between the H.E.S.S. energy range and the LAT energy range. This is typical of  
 624 most PWNe detected by *Fermi*-LAT and H.E.S.S. that present IC emission peaking at a few  
 625 hundreds of GeV and would favor the PWN scenario. However, this source is very extended  
 626 at both wavelengths and could be composed of several  $\gamma$ -ray sources. Follow-up observations  
 627 with VHE experiments and continued observation with *Fermi*-LAT are needed to unveil the  
 628 real nature of HESS J1841–055.

#### 629 4.5.6. HESS J1848–018

630 HESS J1848–018 was discovered during the extended H.E.S.S. Galactic Plane Survey  
 631 (Chaves et al. 2008), in the direction of, but slightly offset from, the star-forming region W43  
 632 (aka G30.8–0.2). The H.E.S.S. emission is characterized by significant extension ( $0^\circ.32 \pm$   
 633  $0^\circ.02$ ), a power-law spectrum of index  $\sim 2.8$  and an integrated flux above 1 TeV  $\sim 2 \times$   
 634  $10^{-12} \text{ cm}^{-2} \text{ s}^{-1}$ . The absence of an energetic pulsar or SNR within  $0^\circ.5$  from HESS J1848–018  
 635 favors an association with the star-forming region W43. The only potential counterpart for  
 636 this source found in radio and X-rays is the Wolf-Rayet star WR 121a.

637 Located  $0^\circ.2$  from the centroid of HESS J1848–018, WR 121a is a WN7 subtype star,  
 638 in a binary system (Luque-Escamilla et al. 2011), associated with W43 and characterized by  
 639 extreme mass loss rates. Chaves et al. (2008) also proposed an association of the H.E.S.S.  
 640 emission with the molecular clouds contained in W43. These molecular clouds could lead to  
 641 the production of high-energy  $\gamma$ -rays from the neutral pion decays following  $p$ - $p$  collisions in  
 642 the ambient gas.

643 In the LAT energy range, Tam et al. (2010) proposed an association with a spatially co-  
 644 incident source 0FGL J1848.6–0138. Lemoine-Goumard et al. (2011a) analyzed the *Fermi*-  
 645 LAT data around HESS J1848–018 and detected a source with a  $3.7\sigma$  evidence for an  
 646 extension ( $\sigma \sim 0.3$ ). This disfavors models in which the LAT emission would be produced  
 647 by a pulsar alone. However, statistics were not large enough to discriminate between one  
 648 extended source and several point sources. Moreover, the spectrum was well described by  
 649 a log normal representation (Eq. 3) and the SED was very similar to those obtained for  
 650 most pulsars detected by *Fermi*-LAT. Therefore, the emission could be a composite of a  
 651 radio-faint pulsar and an additional source.

652 In our analysis, HESS J1848–018 is detected as a faint point-like source but consistent  
 653 with the extension reported by Lemoine-Goumard et al. (2011a). Figure 8 includes the  
 654 H.E.S.S. spectral points from Chaves et al. (2008) and the radio points corresponding to the  
 655 W43 central cluster from Luque-Escamilla et al. (2011). We note that the point obtained in  
 656 our analysis is consistent with the dashed curve, which represents the spectrum derived by  
 657 Lemoine-Goumard et al. (2011a). It is not absolutely clear from this figure whether the LAT  
 658 and H.E.S.S. spectra have a common or a distinct origin, and future multi-wavelength data  
 659 would be needed to discriminate between the pulsar/PWN and the massive star formation  
 660 region hypotheses.

## 661 4.6. Constraints Obtained from Non-Detections

662 This section presents the sources for which no  $\gamma$ -ray emission is detected but the corre-  
 663 sponding upper limits constrain the models.

### 664 4.6.1. HESS J1026–582

665 HESS J1026–582 was discovered by H.E.S.S. during an improved analysis of the region  
 666 of HESS J1023–575 (H.E.S.S. Collaboration et al. 2011e). While HESS J1023–575 is close  
 667 to the energetic pulsar PSR J1023–5746 ( $\dot{E} = 10^{37} \text{ erg s}^{-1}$ ) discovered by the LAT using  
 668 blind search algorithms (Saz Parkinson et al. 2010), the authors proposed an association  
 669 between HESS J1026–582 and PSR J1028–5819 discovered by the Parkes 64-m telescope  
 670 (Keith et al. 2008) and also detected by the LAT (Abdo et al. 2009b). The proximity of  
 671 the pulsar suggested a PWN scenario to explain the VHE emission. This hypothesis is  
 672 supported by the spin-down power of PSR J1028–5819,  $\dot{E} = 8.43 \times 10^{35} \text{ erg s}^{-1}$  (Abdo et al.  
 673 2009b), typical of observed PWNe. Mignani et al. (2012) observed marginal X-ray emission

674 but could not definitely classify the emission as being characteristic of a PWN. Follow-up  
675 observations with *XMM-Newton* and *Chandra* are needed to confirm this detection.

676 No significant LAT emission coming from the location of the H.E.S.S. excess is detected  
677 in our analysis. The very low TS value of 1.0 with an integrated flux less than  $1.6 \times$   
678  $10^{-10}$  ph cm $^{-2}$  s $^{-1}$  (see Table 6) gives little hope for a future detection by the LAT. The  
679 upper limits in Figure 4 show that a rising spectrum is needed in the LAT energy range.  
680 This suggests an IC peak at energies higher than 100 GeV consistent with *Fermi*-LAT  
681 observations of other PWNe. However, the lack of multi-wavelength data (especially in  
682 radio and X-rays) prevents clear identification of this source.

#### 683 4.6.2. *HESS J1458–608*

684 PSR J1459–6053, discovered in  $\gamma$ -rays, is an energetic and older pulsar with a spin-down  
685 power of  $\dot{E} = 9.2 \times 10^{35}$  erg s $^{-1}$ , and a characteristic age of  $\tau_C = 64$  kyr (Abdo et al. 2010e).  
686 An X-ray counterpart to PSR J1459–6053 was discovered by *Swift* (Ray et al. 2011) and  
687 *Suzaku* (Kanai 2007). *HESS J1458–608* was discovered 9.6' away from PSR J1459–6053  
688 after a dedicated observation (de los Reyes et al. 2012). The proximity to the pulsar and the  
689 extension of *HESS J1458–608* suggested that both objects could be related in a PSR/PWN  
690 scenario. In this case, the lack of or the faint X-ray emission could be explained by the  
691 system's age.

692 In our work *HESS J1458–608* was not significantly detected above 10 GeV. Table 6  
693 shows that the observed marginal emission comes from the energy bin between 10 and  
694 31 GeV. Figure 4 shows that subtracting the pulsar's contribution does not change the SED.  
695 This comes from the fact that the spectrum of the pulsar in the 2FGL catalog above 10 GeV  
696 is negligible compared to the SED. The upper limits computed in the energy bins between  
697 31 and 316 GeV, where no pulsar emission is expected, show that a change in the slope of  
698 the spectrum is needed between the H.E.S.S. and the LAT component. This is consistent  
699 with an IC peak above 100 GeV in the range observed for the PWNe detected with the  
700 *Fermi*-LAT. However, the H.E.S.S. spectrum of *HESS J1458–608* differs from other PWNe,  
701 since it seems to show a hardening at high energy.

#### 702 4.6.3. *HESS J1626–490*

703 *HESS J1626–490* is another unidentified source detected during the H.E.S.S. Galactic  
704 Plane Survey (Aharonian et al. 2008c). According to a leptonic model, Eger (2011) found

705 no X-ray source bright enough to be consistent with the H.E.S.S. emission using *XMM-*  
 706 *Newton* observations. However, the authors suggested that a hadronic scenario based on the  
 707 interaction of SNR G335.2+00.1 with a molecular cloud could explain the H.E.S.S. emission.  
 708 This hypothesis is supported by a density depression in H<sub>I</sub> that could be explained by a  
 709 recent event such as a supernova.

710 With a TS of 1.5, HESS J1626–490 is not detected in our analysis. The model presented  
 711 in Eger (2011) and shown in Figure 5 reproduces the H.E.S.S. SED and predicts emission  
 712 below the LAT upper limits. A radio or/and X-ray detection of synchrotron emission from  
 713 a PWN or the detection of a pulsar could call this model into question.

#### 714 4.6.4. HESS J1813–178

715 HESS J1813–178 was discovered during the H.E.S.S. survey of the Inner Galaxy  
 716 (Aharonian et al. 2005a) and also detected by MAGIC (Albert et al. 2006a). The source  
 717 was identified as being SNR G12.8–0.0 following its radio detection by Brogan et al. (2005).  
 718 Using *XMM-Newton* observations, Funk et al. (2007b) detected a complex morphology com-  
 719 posed of a point-like source and an extended nebula. The morphological and spectral simi-  
 720 larities of the central object with a PWN led Funk et al. (2007b) to propose a PWN/SNR  
 721 scenario to describe the X-ray sources. This hypothesis was strengthened by the discovery  
 722 of PSR J1813–1749 (Gotthelf & Halpern 2009). This pulsar is one of the most energetic  
 723 pulsars in our Galaxy with a spin-down power of  $\dot{E} = 5.6 \times 10^{37}$  erg s<sup>-1</sup> but has not yet been  
 724 detected by the LAT. However, the nature of the H.E.S.S. emission remains unclear as either  
 725 the SNR or the PWN could produce emission at these energies.

726 Our analysis yielded a TS of 2.5 with an upper limit on the integrated flux of  $2.4 \times$   
 727  $10^{-10}$  ph cm<sup>-2</sup> s<sup>-1</sup> assuming the H.E.S.S. morphology as spatial shape. Figure 8 shows the  
 728 multi-wavelength SED of HESS J1813–178. The upper limits derived using the procedure  
 729 described in Section 3 show that the spectrum of HESS J1813–178 cannot be flat between  
 730 the H.E.S.S. and the LAT energy ranges and suggest a peak with an energy cutoff located  
 731 between the two energy ranges.

732 Funk et al. (2007b) and Fang & Zhang (2010) investigated a leptonic model in which  
 733 the X-ray core and VHE  $\gamma$ -ray emission are associated. Both take into account IC scattering  
 734 on CMB, infrared and near infrared photon fields and synchrotron emission produced with  
 735 a rather low magnetic field ( $B \sim 7 \mu\text{G}$ ). The main difference between these two models lies  
 736 in the injected electron population, which follows a power-law spectrum with an index of 2.0  
 737 in Funk et al. (2007b) and a Maxwellian + power-law tail spectrum (Spitkovsky 2008) with

738 an index of 2.4 in Fang & Zhang (2010).

739 Both also investigated the possibility for the H.E.S.S. signal to be created by the SNR  
 740 shell. We overlaid on Figure 8 the models proposed by Funk et al. (2007b) and Fang & Zhang  
 741 (2010). The main differences between these two models lies in the injected proton and  
 742 electron populations which follow power-law spectra with an index of 2.1 in Funk et al.  
 743 (2007b) and is computed in a semi-analytical nonlinear model in Fang & Zhang (2010).

744 The upper limits derived in our analysis rejected one of the two models proposed in each  
 745 hypothesis. Therefore, no conclusion can be reached on the nature of the H.E.S.S. emission  
 746 being a PWN or a SNR. However, in light of the different models discussed one can exclude a  
 747 model assuming a Maxwellian + power-law tail injection spectrum with an index of 2.4 with  
 748 the parameters derived in Fang & Zhang (2010) in the PWN scenario. These upper limits  
 749 also constrain the hadronic model by rejecting a power-law injection spectrum of 2.1 with  
 750 the parameters proposed by Funk et al. (2007b). Therefore, whatever the origin of the  $\gamma$ -ray  
 751 emission, the injected spectrum of the primary electrons and protons needs to be relatively  
 752 hard in order to stay below the *Fermi*-LAT upper limits ( $\Gamma \leq 2.1$ ).

## 753 5. DISCUSSION

754 In this section, we investigate the correlations of pulsar age and spin-down power with  
 755 the flux of the associated PWN in the keV, GeV and TeV bands. Table 7 lists the ages, spin-  
 756 down luminosities, and distances for the associated pulsars or other distance information,  
 757 and Table 10 lists the X-ray, GeV and TeV flux (or flux upper limit) for the associated  
 758 PWNe. As a first step, we studied the relation between the spectra in the VHE energy  
 759 range and the LAT energy range. We assumed that the emission measured in the TeV and  
 760 GeV bands comes from the falling and rising edges, respectively, of the IC peak in the SED  
 761 produced by the same population of electrons and we studied the spectral shape of this IC  
 762 peak. Mayer et al. (2012) have shown that a negative correlation between the energy of the  
 763 peak and the pulsar characteristic age would be expected from the evolution of the cooling  
 764 time with energy. We attempted to find this relation starting from the LAT and VHE data.

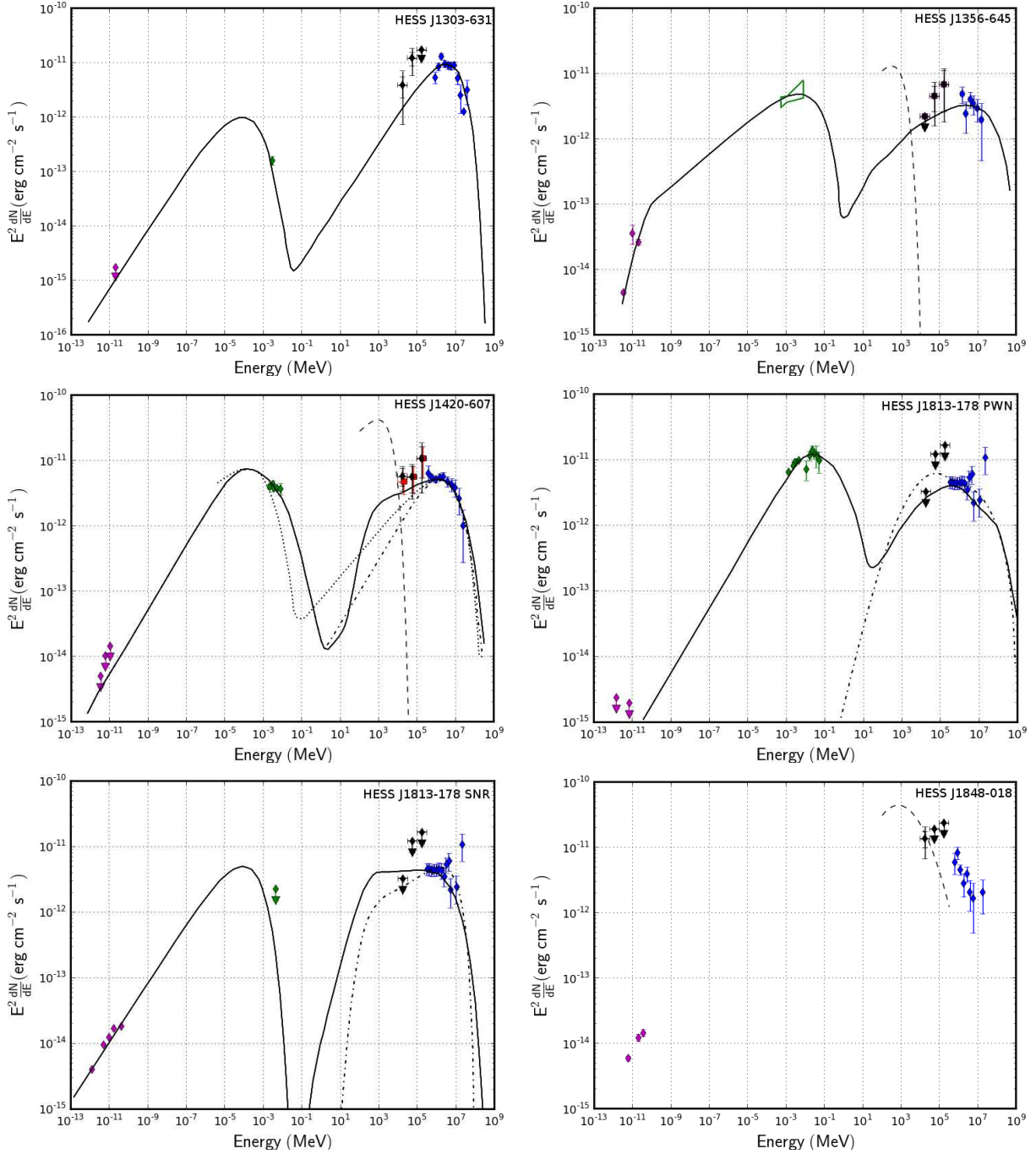


Fig. 8.— Multi-wavelength SEDs of HESS J1303–631, HESS J1356–645, HESS J1420–607, HESS J1813–178 and HESS J1848–018. The blue, green and magenta points represent the H.E.S.S., X-ray and radio spectra respectively. The conventions used for the LAT spectral points are the same as in Figure 5. The dashed line corresponds to the model of associated pulsars. Details on the models are given in the text. The solid, dotted and dashed-dotted lines represent multi-wavelength models from other publications. Models and references: HESS J1303–631: leptonic model proposed by H.E.S.S. Collaboration et al. (2012b). HESS J1356–645: leptonic model proposed by H.E.S.S. Collaboration et al. (2011d). HESS J1420–607: the solid and dashed lines show the hadronic+leptonic and leptonic models proposed by Van Etten & Romani (2010) and the dotted line represents the leptonic model proposed by Kishishita et al. (2012). HESS J1813–178 PWN: the solid and dashed lines respectively show the leptonic models proposed by Funk et al. (2007b) and Fang & Zhang (2010). HESS J1813–178 SNR: the solid and dashed lines respectively show the hadronic models proposed by Funk et al. (2007b) and Fang & Zhang (2010).

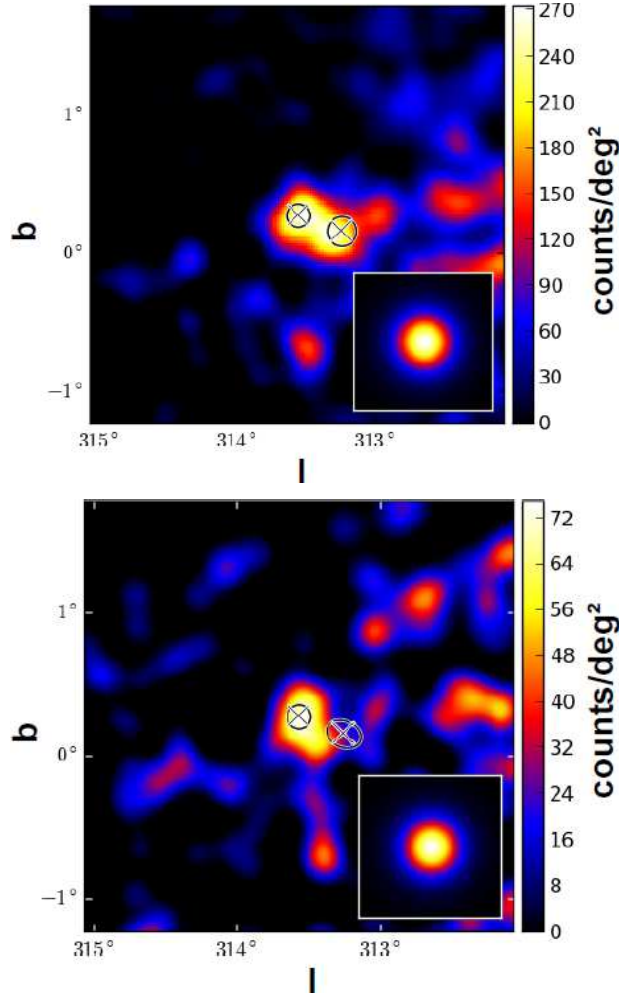


Fig. 9.— Smoothed count map of the region of the Kookaburra complex observed by *Fermi* above 10 GeV (top) and 31 GeV (bottom). The Galactic and isotropic diffuse emissions are subtracted. The left and right circles show the best fit obtained by VHE experiments respectively for the K3 nebula and the Rabbit nebula. The lower right inset is the model predicted emission from a point-like source with the same spectrum as HESS J1420–607 smoothed by the same kernel. There is significant emission from both regions for energies above 10 GeV but there is only significant emission from HESS J1420–607 for energies above 30 GeV.

Table 10. PWNe properties.

Name	$G_{10\text{ GeV}}^{316\text{ GeV}}$ ( $10^{-12}\text{ erg cm}^{-2}\text{ s}^{-1}$ )	$G_{1\text{ TeV}}^{30\text{ TeV}}$ ( $10^{-12}\text{ erg cm}^{-2}\text{ s}^{-1}$ )	$G_{2\text{ keV}}^{10\text{ keV}}$ ( $10^{-12}\text{ erg cm}^{-2}\text{ s}^{-1}$ )	$L_{10\text{ GeV}}^{316\text{ GeV}}$ ( $10^{34}\text{ erg s}^{-1}$ )	Refs
VER J0006+727	< 6.9	...	...	< 0.2	...
Crab	$486 \pm 188$	$80 \pm 17$	$21000 \pm 4200$	$23 \pm 15$	(1)
MGRO J0631+105	< 6.0	...	...	< 0.1	...
MGRO J0632+17	< 29	...	...	< 0.01	...
Vela-X	$134 \pm 11$	$79 \pm 22$	$54 \pm 11$	$0.14 \pm 0.02$	(1)
HESS J1018-589	$6.8 \pm 6.3$	$0.9 \pm 0.4$	...	$0.7 \pm 1.0$	(2)
HESS J1023-575	$27 \pm 12$	$4.8 \pm 1.7$	...	$2.5 \pm 1.1$	(3)
HESS J1026-582	< 9.4	$5.9 \pm 4.4$	...	< 0.6	(3)
HESS J1119-614	$9.1 \pm 5.2$	$2.3 \pm 1.2^a$	...	$7.7 \pm 4.4$	(4)
HESS J1303-631	$16 \pm 11$	$27 \pm 1$	$0.16 \pm 0.03$	$8.3 \pm 6.6$	(5)
HESS J1356-645	$16 \pm 10$	$6.7 \pm 3.7$	$0.06 \pm 0.01$	$1.2 \pm 0.9$	(6)
HESS J1418-609	< 25	$3.4 \pm 1.8$	$3.1 \pm 0.2$	< 0.8	(7,4,8)
HESS J1420-607	$23 \pm 9$	$15 \pm 3$	$1.3 \pm 0.3$	$8.6 \pm 4.5$	(1,7,8)
HESS J1458-608	< 15	$3.9 \pm 2.4$	...	< 2.8	(9)
HESS J1514-591	$46 \pm 13$	$20 \pm 4$	$29 \pm 6$	$10 \pm 4$	(1)
HESS J1554-550	< 3	$1.6 \pm 0.5$	$3 \pm 1$	< 2	(10,11)
HESS J1616-508	$46 \pm 14$	$21 \pm 5$	$4.2 \pm 0.8$	$26 \pm 9$	(1)
HESS J1632-478	$79 \pm 19$	$15 \pm 5$	$0.43 \pm 0.08$	$8.5 \pm 2.1$	(12)
HESS J1640-465	$30 \pm 11$	$5.5 \pm 1.2$	$0.5 \pm 0.1$	$26 \pm 10$	(13)
HESS J1646-458B	< 24	$5 \pm 2$	...	< 10	(14)
HESS J1702-420	< 26	$9 \pm 3$	$0.01 \pm 0.00$	< 7	(15)
HESS J1708-443	$29 \pm 13$	$23 \pm 7$	...	$2 \pm 1$	(16)
HESS J1718-385	< 12	$4 \pm 2$	$0.14 \pm 0.03$	< 3	(1)
HESS J1804-216	$74 \pm 21$	$12 \pm 2$	$0.07 \pm 0.01$	$13 \pm 5$	(17)
HESS J1809-193	< 48	$19 \pm 6$	$0.23 \pm 0.05$	< 7	(1)
HESS J1813-178	< 14	$5.0 \pm 0.6$	...	< 3.7	(18, 19)
HESS J1818-154	< 8.9	$1.3 \pm 0.9$	...	< 6.5	(20)
HESS J1825-137	$59 \pm 77$	$61 \pm 14$	$0.4 \pm 0.1$	$12 \pm 16$	(1)
HESS J1831-098	< 11	$5.1 \pm 0.6$	...	< 2.2	(21)
HESS J1833-105	< 12	$2.4 \pm 1.2$	$40 \pm 0$	< 3.2	(1)
HESS J1837-069	$70 \pm 23$	$22 \pm 9$	$0.6 \pm 0.2$	$36 \pm 12$	(4)
HESS J1841-055	$89 \pm 20$	$24 \pm 3$	...	$1.8 \pm 0.4$	(22)
HESS J1846-029	< 11	$9 \pm 2$	$29 \pm 1$	< 0.2	(4)
HESS J1848-018	$30 \pm 17$	$4 \pm 1$	...	$13 \pm 7$	(23)
HESS J1849-000	< 7	$2.1 \pm 0.4$	$0.9 \pm 0.2$	< 4	(24)
HESS J1857+026	$58 \pm 10$	$18 \pm 3$	...	$57 \pm 18$	(22)
MGRO J1908+06	< 32	$12 \pm 5$	...	< 4	(25)
HESS J1912+101	< 27	$7 \pm 4$	...	< 6	(26)
VER J1930+188	< 5.5	$2.3 \pm 1.3$	$5.2 \pm 0.1$	< 5.4	(4, 27)
VER J1959+208	< 1.9	...	...	< 0.1	(1)
MGRO J2019+37	< 27	...	...	< 21	...
MGRO J2228+61	< 12	...	$0.88 \pm 0.02$	< 7.4	(4)

a- This flux has been computed from the luminosity given in (15). Since no H.E.S.S. spectral index is available, we assumed a fiducial index of 2.4.

Note. — The flux of the PWNe candidates measured by the LAT (10-316 GeV, column 2), by VHE experiments (1-30 TeV, column 3), and in the 2-10 keV X-ray energy range. Column 5 is the luminosity computed assuming the pulsar distances from

Table 7.

References : (1) Mattana et al. (2009) and references therein, (2) (McArthur 2011), (3) H.E.S.S. Collaboration et al. (2011e), (4) Kargaltsev & Pavlov (2010), (5) H.E.S.S. Collaboration et al. (2012b), (6) H.E.S.S. Collaboration et al. (2011d), (7) Kishishita et al. (2012), (8) Aharonian et al. (2006a), (9) de los Reyes et al. (2012), (10) Temim et al. (2009), (11) Acero et al. (2012), (12) Balbo et al. (2010), (13) Aharonian et al. (2006d), (14) (Abramowski et al. 2012), (15) (Aharonian et al. 2006d), (16) H.E.S.S. Collaboration et al. (2011b), (17) (Aharonian et al. 2006d), (18) Funk et al. (2007b), (19) Fang & Zhang (2010), (20) Hofverberg et al. (2011), (21) (Sheidaei 2011), (22) Aharonian et al. (2008c), (23) Chaves et al. (2008), (24) Terrier et al. (2008), (25) (Aharonian et al. 2009), (26) Aharonian et al. (2008a) and (27) Acciari et al. (2010).

765 Among the 58 sources analyzed, 36 sources have an associated pulsar. We selected the  
 766 14 sources flagged as PWN or PWNe in Table 4 as they are likely due to IC emission.

767 We searched for a correlation between the peak energy and the characteristic age of a  
 768 pulsar by estimating the peak energy of the assumed IC component. To characterize the IC  
 769 peak we used the log-normal representation,

$$\frac{dN}{dE} = N_0 \times \left( \frac{E}{E_0} \right)^{-[\alpha + \beta \times \log_{10}(\frac{E}{E_0})]} \quad (3)$$

770 First, we checked if a log-normal spectral model was a possible representation of the  
 771 spectrum of the sources observed at LAT and VHE energies. If the data were well-reproduced  
 772 by a log-normal representation, then there should be a correlation between the energy-flux  
 773 ratio and the VHE experiment spectral index. We fixed  $E_0$  at 300 GeV and  $\beta$  at 0.2 (since  
 774  $\beta$  corresponds to the typical curvature seen in the spectra) and fit the prefactor  $N_0$  and the  
 775 index  $\alpha$  using our LAT and VHE spectral points. Figure 10 plots the LAT to VHE energy  
 776 flux ratios measured assuming a power-law spectrum in each energy range as a function  
 777 of their spectral indices measured by VHE experiments and the relation expected for a  
 778 log-normal model. To derive this relation, we randomly generated a thousand uniformly  
 779 distributed sets of  $\alpha$  providing a thousand different log-normal representations. For each  
 780 log-normal model we derived the associated spectral points in  $dN/dE$ , assuming Poisson  
 781 statistics with zero background counts, and used them to obtain the corresponding power-  
 782 law index  $\Gamma_{\text{TeV}}$  between 1 and 30 TeV. Then the log-normal model is used to compute the  
 783 energy flux ratio and derive a relation between  $\Gamma_{\text{TeV}}$  and this flux ratio. HESS J1303–631 and  
 784 HESS J1632–478 are known to be contaminated by neighboring sources and were therefore  
 785 removed from this figure. The energy flux ratio and the VHE index are correlated with  
 786 a correlation coefficient of  $+0.72 \pm 0.11$ . Therefore, the log-normal model seems to be  
 787 acceptable to reproduce the spectra between 10 GeV and 30 TeV.

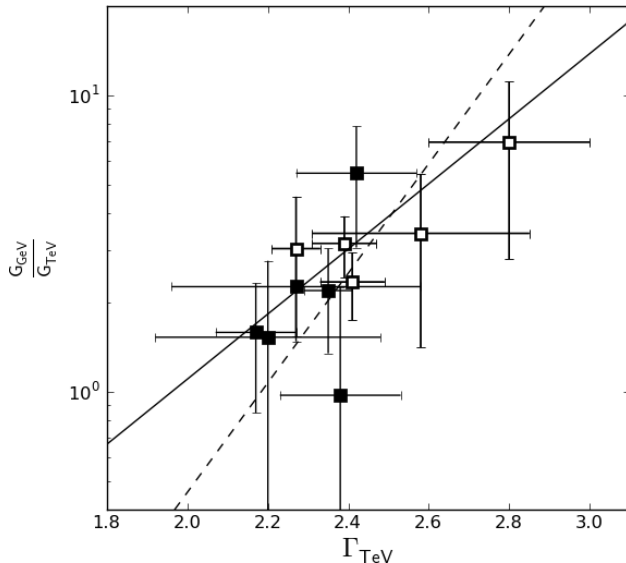


Fig. 10.— Ratio of the LAT to the VHE energy flux as a function of the VHE spectral index for sources classified as “PWN” or “PWNc”. The LAT flux is in the 10 GeV to 316 GeV energy range and the VHE flux is in the 1 TeV to 30 TeV energy range. The fluxes were obtained using power-law fits in each energy range. Sources classified in the TeVCat as “PWN” are represented by full markers and sources classified as “UNIDs” by hollow markers. The LAT fluxes were obtained subtracting any potential pulsar emission. The black line corresponds to a fit of a linear function to the points :  $(1.10 \pm 0.48) \times \Gamma_{TeV} - (2.15 \pm 1.14)$  with  $\chi^2/d.o.f = 11.2/9$ . The dashed line corresponds to the correlation expected for a log-normal representation of  $\beta = 0.2$  and  $E_0 = 300$  GeV. HESS J1303–631 and HESS J1632–478 are not included in this figure, because their energy fluxes are known to be contaminated by neighboring sources in the LAT energy range (see Section 4). HESS J1119–614 is not plotted since its TeV spectral index is not known.

788 We removed HESS J1119–614 from the sample of sources since only the integrated flux  
 789 above 1 TeV is available for this source and we required at least 3 spectral points to perform  
 790 a fit. Then we defined the energy of the peak ( $E_{peak}$ ) as the energy at which the modeled  
 791 SED in  $\nu F_\nu$  is maximal. This also corresponds to

$$\alpha + 2\beta \times \log_{10} \left( \frac{E_{peak}}{E_0} \right) = 2. \quad (4)$$

792 Since LAT spectral points typically suffer larger uncertainty and are less numerous than  
 793 the VHE ones, this method is biased by the greater weight given to the VHE side of the  
 794 log-normal representation. The fit results as well as the peak position are presented in

795 Table 11.

796 We plotted the resulting  $E_{\text{peak}}$  as a function of the age in Figure 11. These values  
 797 of  $E_{\text{peak}}$  and the age yielded a correlation coefficient of  $-0.06 \pm 0.28$ . Furthermore, a fit  
 798 of the value assuming a linear function yielded  $\log_{10}(E_{\text{peak}}/1 \text{ GeV}) = (-0.13 \pm 0.09) \times$   
 799  $(\log_{10}(\tau_C/1 \text{ kyr}) - \overline{\log_{10}(\tau_C/1 \text{ kyr})}) + (2.41 \pm 0.04)$  with  $\chi^2/dof = 15.9/7$ , while a simple  
 800 model assuming a constant yielded  $\log_{10}(E_{\text{peak}}/1 \text{ GeV}) = 2.38 \pm 0.04$  with  $\chi^2/dof = 16.9/8$ .  
 801 This means that the linear function improves the fit at only the  $1 \sigma$  level. This coefficient and  
 802 this comparison show that, contrary to the expectation (Mayer et al. 2012), no downward  
 803 correlation is observed. However, this correlation might be obscured by the usage of the  
 804 characteristic age of the pulsar which may not be a good age estimator for the PWN. For  
 805 instance, MSH 15–52 is a known case for which two ages are proposed, either the charac-  
 806 teristic age of the pulsar, 1.7 kyr or an age between 20 and 40 kyr as suggested by the size  
 807 and general appearance of the SNR (Gvaramadze 2001).

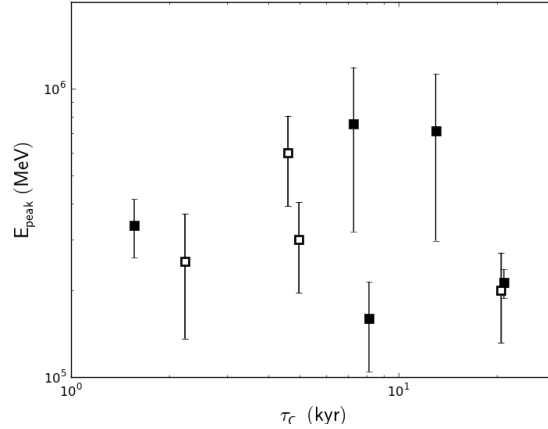


Fig. 11.— Energy of the maximum of the IC peak as a function of the characteristic age of the pulsar for sources labelled as PWN or PWNc in Table 4. Full markers represent sources with a clear PWN association at VHE while hollow markers correspond to sources for which the association is less clear. The fitted SED corresponds to spectra in which contributions of pulsars summarized in Table 2 are subtracted. HESS J1640–465 and HESS J1848–018 are not plotted since the age of their putative pulsar is not known. As in Figure 10, HESS J1303–631, HESS J1632–478 and HESS J1119–614 are not plotted.

808 Using the log-normal fit presented in Table 11 we derived the mean parameters  $\bar{\alpha} =$   
 809  $2.06 \pm 0.02$  and  $10^{\overline{\log_{10}(E_{\text{peak}})}} = 215_{-23}^{+25}$  GeV. To find a putative correlation between luminosity  
 810 ratio and the pulsar characteristics, we plot the GeV to TeV luminosity ratio as a function

Table 11. IC peak fit results

Name	$\Gamma_{TeV}$	$\alpha$	$E_{\text{peak}}$ (GeV)	$\chi^2/\text{d.o.f}$
HESS J1023–575	$2.58 \pm 0.27$	$2.17 \pm 0.07$	$113 \pm 45$	9.3/6
HESS J1303–631 <sup>a</sup>	$2.44 \pm 0.03$	$1.83 \pm 0.10$	$798 \pm 459$	8.2/9
HESS J1356–645	$2.20 \pm 0.28$	$1.84 \pm 0.10$	$754 \pm 434$	7.7/6
HESS J1420–607	$2.17 \pm 0.10$	$1.88 \pm 0.06$	$599 \pm 206$	8.2/10
HESS J1514–591	$2.27 \pm 0.31$	$1.98 \pm 0.04$	$337 \pm 178$	12.8/15
HESS J1616–508	$2.35 \pm 0.06$	$2.11 \pm 0.06$	$159 \pm 55$	4.4/7
HESS J1632–478 <sup>a</sup>	$2.12 \pm 0.20$	$2.18 \pm 0.12$	$106 \pm 74$	11.6/5
HESS J1640–465	$2.42 \pm 0.15$	$2.27 \pm 0.08$	$63 \pm 29$	4.9/6
HESS J1825–137	$2.45 \pm 0.30$	$2.06 \pm 0.02$	$212 \pm 24$	10.2/12
HESS J1837–069	$2.27 \pm 0.06$	$2.03 \pm 0.08$	$252 \pm 116$	11.5/13
HESS J1841–055	$2.41 \pm 0.08$	$2.00 \pm 0.06$	$300 \pm 103$	10.5/9
HESS J1848–018	$2.8 \pm 0.20$	$2.23 \pm 0.15$	$204 \pm 112$	6.9/8
HESS J1857+026	$2.39 \pm 0.05$	$2.07 \pm 0.06$	$201 \pm 69$	9.4/12

a- Since these sources are known to be contaminated by neighboring sources the corresponding rows were not used in Section 5.

Note. — The fit parameters of the log-normal fit to the LAT and VHE data. Column 2 gives the spectral index of the power law fit by VHE experiments. Columns 3 and 4 give the index  $\alpha$  at  $E_0 = 300$  GeV and the peak position of the log-normal model as defined in Section 5. Column 6 gives the reduced  $\chi^2$  of the fit. The log-normal model was fit to the VHE and LAT SED with the pulsar’s contribution subtracted.

811 of the pulsar’s characteristic age and spin-down energy in Figure 12. To determine if the  
 812 correlation of the luminosity ratio with the characteristic age and the pulsar spin-down  
 813 power is due to one of the components, this figure also presents luminosities derived in the  
 814 GeV, TeV and keV domains. We overlaid the mean ratio,  $\bar{R} = 10^{\overline{\log_{10}(R)}} = 2.7_{-1.4}^{+2.7}$ , found  
 815 between the LAT and VHE energy ranges using the 14 sources flagged as PWNe and PWNe  
 816 in Table 4. We included in this figure and the figures that follow all sources analyzed in  
 817 this work including pulsar-like sources, providing an upper-limit on the PWN emission and  
 818 sources flagged as “O”. This figure shows that no source is located at more than  $2\sigma$  from  
 819 this mean ratio except HESS J1804–216, which is not a PWN candidate as explained in  
 820 section 4.3.

821 As a second step, we investigated the relation between the spectra in the X-ray energy  
 822 range and the LAT energy range. Mattana et al. (2009) have shown a correlation between  
 823 the X-ray flux of a PWN and the physical properties of the pulsar assuming the emission  
 824 of the PWN to be composed of synchrotron emission in the keV domain. As described  
 825 in Mattana et al. (2009), the  $\gamma$ -ray and the X-ray luminosities of PWNe are expected to  
 826 decrease with time and the cooling time of electrons emitting synchrotron X-rays is smaller  
 827 than the cooling time of the electrons emitting IC  $\gamma$ -rays. Therefore, the X-ray emission  
 828 traces the recent evolution of a PWN while the  $\gamma$ -ray photons trace a longer period. Since  
 829 the pulsar spin-down power driving the electron injection decreases with time, the ratio of  
 830 the IC emission to the synchrotron emission is expected to increase over time.

831 Figure 12 and Table 10 give the ratio of the  $\gamma$ -ray luminosity to the X-ray luminosity  
 832 as a function of the age and as a function of the pulsar spin-down power. As reported for  
 833 VHE experiments (Mattana et al. 2009), no clear correlation is found between the  $\gamma$ -ray flux  
 834 and spin-down power or between the  $\gamma$ -ray flux and the characteristic age. This can also be  
 835 seen on Figure 13. On the other hand, there is a correlation between the X-ray flux of the  
 836 observed PWNe and the pulsars spin-down power and characteristic age. This causes the  
 837 correlation between the ratio of the  $\gamma$ -ray flux to the X-ray flux and the pulsar properties. We  
 838 also represented the relations derived in Mattana et al. (2009) multiplied by  $\bar{R}$  for the whole  
 839 sample of sources and for the sources clearly identified with PWNe. The overall agreement  
 840 with these relations is relatively good.

841 In the plot showing the LAT to X-ray energy flux ratio as a function of the pulsar  
 842 characteristic age, four upper limits are well below the correlation relations derived by  
 843 Mattana et al. (2009). These outliers are, in increasing spin down power, HESS J1833–105,  
 844 HESS J1554–550, HESS J1849–000 and HESS J1718–385. HESS J1833–105 and  
 845 HESS J1718–385 are also included in Mattana et al. (2009), unlike HESS J1554–550 and  
 846 HESS J1849–000. Table 10 shows that the GeV over TeV upper limit is in each case larger

847 than  $\bar{R}$ . Therefore, their small LAT/X-ray luminosity ratios do not come from an especially  
 848 small LAT flux but instead from an especially large X-ray flux relative to other sources with  
 849 a similar characteristic age.

850 These figures show that the *Fermi*-LAT mainly detects young and middle-aged PWNe  
 851 (1-30 kyr) around energetic pulsars with spin-down powers between  $10^{36}$  and  $10^{39}$  erg s $^{-1}$ .  
 852 One can see from these figures that the VHE sources older than 30 kyr are not detected by  
 853 the LAT, while Mayer et al. (2012) predict a higher flux in the LAT energy range than in  
 854 the VHE experiments energy range. However it should be noted that among these nine VHE  
 855 sources, at least 7 suffer one or several biases:

- 856 • Source misidentification: for example, HESS J1912+101 has recently been pro-  
 857 posed to be a shell-type SNR<sup>6</sup>, but some of the emission could originate in the  
 858 pulsar wind. Similarly, HESS J1702–420 and HESS J1646–458B cannot be  
 859 clearly associated as PWNe and deeper multi-wavelength observations are needed  
 860 to classify the emission.
- 861 • Potential characteristic age overestimation. See, for example, HESS J1809–193  
 862 (Sheidaei 2011).
- 863 • HESS J1026–582, HESS J1809–193, HESS J1831–098 and HESS J1849–000  
 864 are located in regions of strong diffuse emission where the LAT is less sensitive  
 865 to any potential emission.

866 Therefore, the lack of a population of old  $\gamma$ -ray-loud PWNe cannot be proven given the  
 867 current statistics and systematics associated with this analysis.

868 Finally, Figure 13 shows the  $\gamma$ -ray luminosity of the PWN as a function of the pul-  
 869 sar spin-down power assuming the distances listed in Table 7. The  $\gamma$ -ray luminosity is,  
 870 for all sources, computed by subtracting any potential emission from nearby LAT-detected  
 871 pulsars. The distance uncertainties are calculated assuming a 20% uncertainty on the disper-  
 872 sion measure (2PC). For most pulsars this yields a realistic uncertainty, for many however  
 873 it leads to a large factor, for instance a factor of 6 in Abdo et al. (2009f), between two  
 874 distance estimates. Among the detected sources, eight show a  $\gamma$ -ray efficiency below 1%  
 875 and five are consistent within uncertainties of having an efficiency between 1 and 10%.  
 876 Six upper limits on the LAT luminosity of VHE sources associated to a PWN powered

---

<sup>6</sup>This was proposed in a presentation at the AstroParticules et Cosmologie laboratory:  
<http://www.apc.univ-paris7.fr/~simsemikoz/CosmicRays/CosmicRays/Dec14/djannati-atai.pdf>

877 by an energetic pulsar ( $\dot{E} \geq 10^{36} \text{ erg s}^{-1}$ ) are well below an efficiency of 1%. They are  
 878 HESS J1418–09, HESS 1813–178, HESS J1833–105, HESS J1849–000, MGRO J2228+61  
 879 and VER J1930+188.

## 880 6. CONCLUSION

881 We looked for LAT counterparts to the VHE sources potentially associated to PWNe  
 882 using 45 months of *Fermi*-LAT observations. We detected 30 of the 58 sources at LAT  
 883 energies:

- 884 • 9 may be due to pulsar emission for energies above 10 GeV,
- 885 • 7 sources cannot be clearly associated to a PWN,
- 886 • 11 are PWNe candidates,
- 887 • 3 are clearly identified as PWNe: HESS J1825–137 and HESS J1514–591 (aka  
 888 MSH 15–52) already detected and HESS J1356–645 detected for the first time  
 889 in this analysis.

890 Among these 30 sources, 23 were also detected in 1FHL and 15 in Neronov & Semikoz  
 891 (2012). We analyzed their morphology and found that 8 of them are significantly extended.

892 Adding the Crab Nebula and Vela–X to the 3 clearly identified PWNe, 5 PWNe  
 893 are now detected at LAT energies. 11 sources are promising PWNe candidates such as  
 894 HESS J1420–607 and HESS J1119–614. These 16 sources are associated with young (with  
 895 an age between 1 and 30 kyr) and powerful pulsars with a spin down power between  $10^{36}$   
 896 and  $10^{39} \text{ erg s}^{-1}$  and typically have a conversion efficiency below 10%. No correlation has  
 897 been found between the LAT energy flux and the pulsar characteristic age. This work has  
 898 not shown any evidence for a shift of the PWN IC emission towards the LAT energy range  
 899 as a function of the characteristic age. However this can be due to large uncertainties on the  
 900 systems’ age. The correlation of the LAT to X-ray luminosities ratio with the pulsar char-  
 901 acteristic age and its spin-down power is consistent with the work of Mattana et al. (2009)  
 902 derived for the VHE to X-ray luminosities ratio.

903 The *Fermi* LAT Collaboration acknowledges generous ongoing support from a number  
 904 of agencies and institutes that have supported both the development and the operation of the  
 905 LAT as well as scientific data analysis. These include the National Aeronautics and Space  
 906 Administration and the Department of Energy in the United States, the Commissariat à

907 l’Energie Atomique and the Centre National de la Recherche Scientifique / Institut National  
908 de Physique Nucléaire et de Physique des Particules in France, the Agenzia Spaziale Italiana  
909 and the Istituto Nazionale di Fisica Nucleare in Italy, the Ministry of Education, Culture,  
910 Sports, Science and Technology (MEXT), High Energy Accelerator Research Organization  
911 (KEK) and Japan Aerospace Exploration Agency (JAXA) in Japan, and the K. A. Wallen-  
912 berg Foundation, the Swedish Research Council and the Swedish National Space Board in  
913 Sweden.

914 Additional support for science analysis during the operations phase is gratefully acknowl-  
915 edged from the Istituto Nazionale di Astrofisica in Italy and the Centre National d’Études  
916 Spatiales in France.

917 This research made use of `pywcsgrid2`, an open-source plotting package for Python<sup>7</sup>.  
918 The authors acknowledge the use of the TeV catalog website<sup>8</sup> provided by the University  
919 of Chicago. The authors acknowledge the use of the *Australia Telescope National Facility*  
920 pulsar catalog<sup>9</sup>.

---

<sup>7</sup>`pywcsgrid2` can be obtained from: <http://leejjoon.github.com/pywcsgrid2/>.

<sup>8</sup>The TeV catalog can be obtained from: <http://tevcat.uchicago.edu/>

<sup>9</sup>The ATNF catalog can be obtained from: <http://www.atnf.csiro.au/people/pulsar/psrcat/>

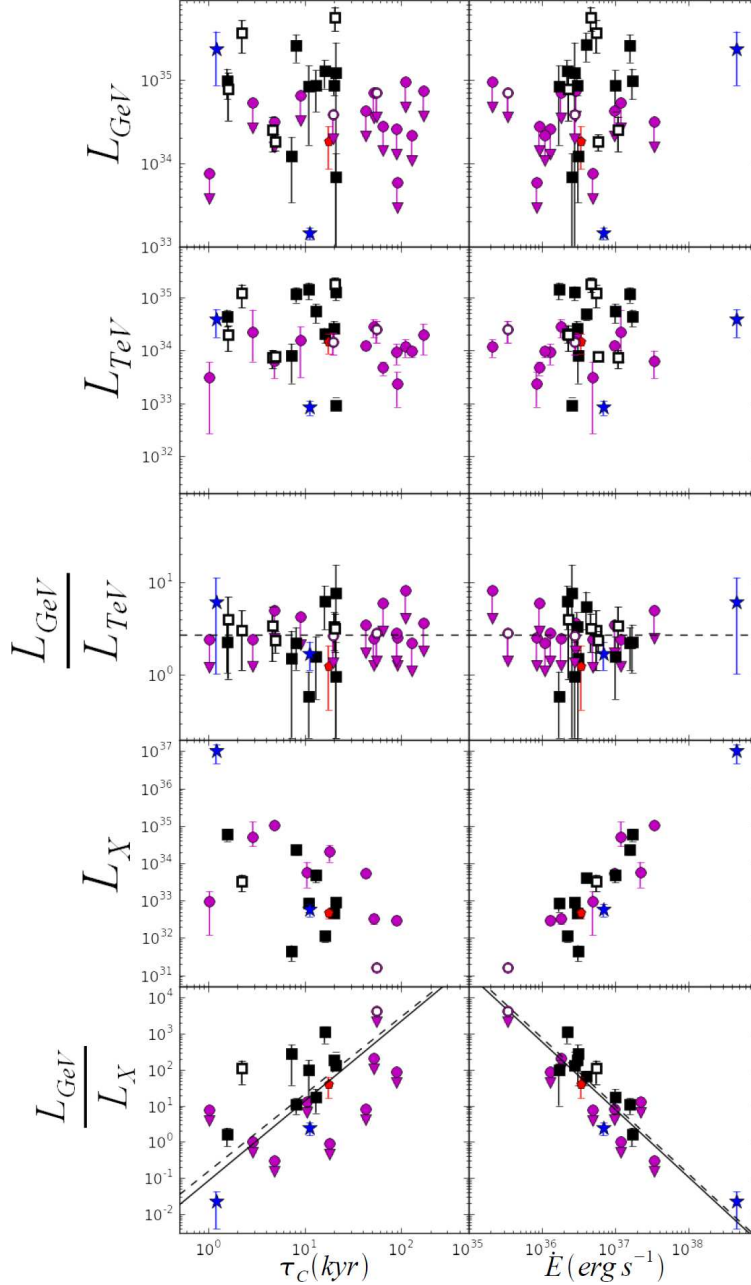


Fig. 12.— From top to bottom: LAT luminosity, VHE luminosity, ratio of LAT to VHE luminosity, X-ray luminosity, and the ratio of LAT to X-ray luminosity as a function of the pulsar characteristic age (left) and the pulsar spin-down power (right). The X-ray, LAT, and VHE fluxes are integrated in the 2 keV to 10 keV, 10 GeV to 316 GeV, 10 TeV to 30 TeV energy ranges respectively. Full markers correspond to sources with a clear PWN association at VHE energies while hollow markers correspond to sources for which the association is less clear. The black squares (■) represent the sources detected at LAT energies, the magenta circles (●) show the upper limits, the red pentagon (⬠) is HESS J1708–443 showing pulsar behavior in the LAT energy range and the blue stars (★) represent the Crab nebula and Vela-X not studied in this work. The LAT luminosity corresponds to Table 10 and was computed after removing any potential emission from LAT-detected pulsars. The dashed and solid lines are explained in Section 5.

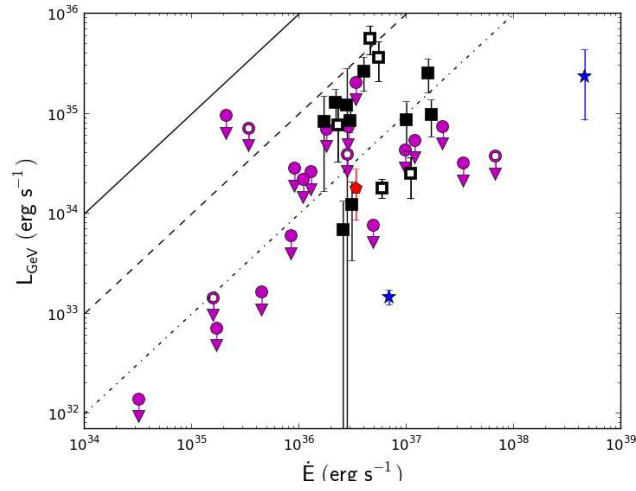


Fig. 13.— LAT luminosity as a function of the pulsar’s spin down power. The symbols are defined in Figure 12. The LAT luminosity was computed after removing any potential emission from LAT-detected pulsars. The upper limit on HESS J1818–154 is excluded from the plot because of its low value of  $\dot{E}$ .

## REFERENCES

- 921
- 922 Abdo, A. A., et al. 2013, ArXiv : 1305.4385
- 923 —. 2007, ApJ, 664, L91
- 924 —. 2009a, Science, 325, 840
- 925 —. 2009b, ApJ, 695, L72
- 926 —. 2009c, ApJ, 706, 1331
- 927 —. 2009d, ApJ, 696, 1084
- 928 —. 2009e, ApJ, 700, L127
- 929 —. 2009f, ApJ, 700, 1059
- 930 —. 2010a, ApJ, 714, 927
- 931 —. 2010b, ApJ, 708, 1254
- 932 —. 2010c, ApJ, 713, 146
- 933 —. 2010d, ApJ, 711, 64
- 934 —. 2010e, ApJS, 187, 460
- 935 Abramowski, A., et al. 2012, A&A, 537, A114
- 936 Acciari, V. A., et al. 2010, ApJ, 719, L69
- 937 Acero, F., et al. 2012, ArXiv:1201.0481
- 938 Ackermann, M., et al. 2011, ApJ, 726, 35
- 939 —. 2012, ApJS, 203, 4
- 940 Aharonian, F., et al. 2005a, Science, 307, 1938
- 941 —. 2005b, A&A, 435, L17
- 942 —. 2005c, A&A, 439, 1013
- 943 —. 2005d, A&A, 432, L25
- 944 —. 2006a, A&A, 456, 245

- 945 —. 2006b, *A&A*, 460, 365
- 946 —. 2006c, *A&A*, 457, 899
- 947 —. 2006d, *ApJ*, 636, 777
- 948 —. 2007, *A&A*, 472, 489
- 949 —. 2008a, *A&A*, 484, 435
- 950 —. 2008b, *A&A*, 483, 509
- 951 —. 2008c, *A&A*, 477, 353
- 952 —. 2009, *A&A*, 499, 723
- 953 Ajello, M., et al. 2012, *ApJ*, 744, 80
- 954 Albert, J., et al. 2006a, *ApJ*, 637, L41
- 955 —. 2006b, *ApJ*, 643, L53
- 956 Aleksić, J., et al. 2012, *Astroparticle Physics*, 35, 435
- 957 Aliu, E. 2011, in *International Cosmic Ray Conference, Vol. 7, International Cosmic Ray*  
958 *Conference*, 227
- 959 Atkins, R., et al. 2003, *ApJ*, 595, 803
- 960 Atwood, W. B., et al. 2009, *ApJ*, 697, 1071
- 961 Balbo, M., et al. 2010, *A&A*, 520, A111
- 962 Bartoli, B., et al. 2012, *ApJ*, 745, L22
- 963 Brogan, C. L., et al. 2005, *ApJ*, 629, L105
- 964 Brun, F., et al. 2011, *ArXiv:1104.5003*
- 965 Buehler, R., et al. 2012, *ApJ*, 749, 26
- 966 Camilo, F., et al. 2000, *ApJ*, 541, 367
- 967 —. 2006, *ApJ*, 637, 456
- 968 —. 2001, *ApJ*, 557, L51

- 969 —. 2004, *ApJ*, 611, L25
- 970 Caswell, J. L., McClure-Griffiths, N. M., & Cheung, M. C. M. 2004, *MNRAS*, 352, 1405
- 971 Chaves, R. C. G., Renaud, M., Lemoine-Goumard, M., & Goret, P. 2008, in American Insti-  
972 tute of Physics Conference Series, Vol. 1085, American Institute of Physics Conference  
973 Series, ed. F. A. Aharonian, W. Hofmann, & F. Rieger, 372–375
- 974 Coe, M. J., et al. 2012, *ArXiv:1202.3164*
- 975 Cordes, J. M., & Lazio, T. J. W. 2002, *ArXiv Astrophysics e-prints*
- 976 D’Amico, N., et al. 2001, *ApJ*, 552, L45
- 977 de Jager, O. C., & Djannati-Ataï, A. 2009, in *Astrophysics and Space Science Library*, Vol.  
978 357, *Astrophysics and Space Science Library*
- 979 de Jager, O. C., et al. 2009, *ArXiv:0906.2644*
- 980 de los Reyes, R., Zajczyk, A., Chaves, R. C. G., & for the H.E.S.S. collaboration. 2012,  
981 *ArXiv:1205.0719*
- 982 Djannati-Ataï, A., de Jager, O. C., Terrier, R., & et al. 2008, in *International Cosmic Ray*  
983 *Conference*, Vol. 2, *International Cosmic Ray Conference*, 823–826
- 984 Dodson, R., Legge, D., Reynolds, J. E., & McCulloch, P. M. 2003, *ApJ*, 596, 1137
- 985 Domainko, W., & Ohm, S. 2012, *A&A*, 545, A94
- 986 Eger, P. 2011, in *International Cosmic Ray Conference*, Vol. 7, *International Cosmic Ray*  
987 *Conference*, 44
- 988 Fang, J., & Zhang, L. 2010, *ApJ*, 718, 467
- 989 Funk, S., et al. 2007a, *ApJ*, 662, 517
- 990 —. 2007b, *A&A*, 470, 249
- 991 Gabici, S., Aharonian, F. A., & Casanova, S. 2009, *MNRAS*, 396, 1629
- 992 Gast, H., et al. 2012, *ArXiv:1204.5860*
- 993 Gonzalez, M., & Safi-Harb, S. 2003, *ApJ*, 591, L143
- 994 Górski, K. M., et al. 2005, *ApJ*, 622, 759

- 995 Gotthelf, E. V., & Halpern, J. P. 2008, *ApJ*, 681, 515
- 996 —. 2009, *ApJ*, 700, L158
- 997 Gotthelf, E. V., Halpern, J. P., Terrier, R., & Mattana, F. 2011, *ApJ*, 729, L16
- 998 Grondin, M.-H., Fermi-LAT collaboration, & Pulsar Timing Consortium. submitted, *ApJ*
- 999 Grondin, M.-H., et al. 2011, *ApJ*, 738, 42
- 1000 Guillemot, L., et al. 2012, *ApJ*, 744, 33
- 1001 Gvaramadze, V. V. 2001, *A&A*, 374, 259
- 1002 Hall, T. A., et al. 2003, *ApJ*, 583, 853
- 1003 Hartman, R. C., et al. 1999, *ApJS*, 123, 79
- 1004 H.E.S.S. Collaboration et al. 2011a, *A&A*, 531, A81
- 1005 —. 2011b, *A&A*, 528, A143
- 1006 —. 2011c, *A&A*, 525, A45
- 1007 —. 2011d, *A&A*, 533, A103
- 1008 —. 2011e, *A&A*, 525, A46
- 1009 —. 2012a, *A&A*, 541, A5
- 1010 —. 2012b, *A&A*, 548, A46
- 1011 Hessels, J. W. T., et al. 2004, *ApJ*, 612, 389
- 1012 —. 2008, *ApJ*, 682, L41
- 1013 Hinton, J. A., & Hofmann, W. 2009, *ARA&A*, 47, 523
- 1014 Hofverberg, P. 2011, in *International Cosmic Ray Conference*, Vol. 7, *International Cosmic*  
1015 *Ray Conference*, 247
- 1016 Hofverberg, P., Chaves, R. C. G., Méhault, J., de Naurois, M., & for the H.E.S.S. Collabo-  
1017 *ration*. 2011, *ArXiv:1112.2901*
- 1018 Hoppe, S. 2008, in *International Cosmic Ray Conference*, Vol. 2, *International Cosmic Ray*  
1019 *Conference*, 579–582

- 1020 Huang, R. H. H., et al. 2012, *ApJ*, 760, 92
- 1021 James, F., & Roos, M. 1975, *Comput. Phys. Commun.*, 10, 343
- 1022 Johnston, S., Manchester, R. N., Lyne, A. G., Kaspi, V. M., & D’Amico, N. 1995, *A&A*,  
1023 293, 795
- 1024 Kanai, Y. 2007, phd thesis
- 1025 Kargaltsev, O., & Pavlov, G. G. 2010, *ArXiv:1002.0885*, 1248, 25
- 1026 Keith, M. J., et al. 2008, *MNRAS*, 389, 1881
- 1027 Kerr, M. 2011, *ArXiv:1101.6072*
- 1028 Kishishita, T., Bamba, A., Uchiyama, Y., Tanaka, Y., & Takahashi, T. 2012, *ApJ*, 750, 162
- 1029 Komin, N., et al. 2012, *ArXiv:1201.0639*
- 1030 Kothes, R., Uyaniker, B., & Pineault, S. 2001, *ApJ*, 560, 236
- 1031 Kramer, M., et al. 2003, *MNRAS*, 342, 1299
- 1032 Lamb, R. C., & Macomb, D. J. 1997, *ApJ*, 488, 872
- 1033 Lande, J., et al. 2012, *ApJ*, 756, 5
- 1034 Leahy, D. A., Tian, W., & Wang, Q. D. 2008, *AJ*, 136, 1477
- 1035 Lemièrre, A., Slane, P., Gaensler, B. M., & Murray, S. 2009, *ApJ*, 706, 1269
- 1036 Lemoine-Goumard, M., Ferrara, E., Grondin, M.-H., Martin, P., & Renaud, M. 2011a,  
1037 *Mem. Soc. Astron. Italiana*, 82, 739
- 1038 Lemoine-Goumard, M., et al. 2011b, *A&A*, 533, A102
- 1039 Lorimer, D. R., et al. 2006, *MNRAS*, 372, 777
- 1040 Lucke, P. B. 1978, *A&A*, 64, 367
- 1041 Luque-Escamilla, P. L., et al. 2011, *A&A*, 532, A92
- 1042 Manchester, R. N., Hobbs, G. B., Teoh, A., & Hobbs, M. 2005a, *VizieR Online Data Catalog*,  
1043 7245, 0
- 1044 —. 2005b, *AJ*, 129, 1993

- 1045 Manchester, R. N., et al. 2001, *MNRAS*, 328, 17
- 1046 Mattana, F., et al. 2009, *ApJ*, 694, 12
- 1047 Mayer, M. 2010, Diplomarbeit : Erlangen Centre for Astroparticle Physics Physikalisches  
1048 Institut 2 Lehrstuhl für Physik Friedrich-Alexander-Universität Erlangen-Nürnberg
- 1049 Mayer, M., Brucker, J., Jung, I., Valerius, K., & Stegmann, C. 2012, *ArXiv:1202.1455*
- 1050 McArthur, S. f. 2011, *ArXiv:1111.2591*, eConf C110509
- 1051 Mignani, R. P., et al. 2012, *A&A*, 543, A130
- 1052 Mukherjee, R., & Halpern, J. P. 2005, *ApJ*, 629, 1017
- 1053 Neronov, A., & Semikoz, D. V. 2012, *Phys. Rev. D*, 85, 083008
- 1054 Ng, C.-Y., Roberts, M. S. E., & Romani, R. W. 2005, *ApJ*, 627, 904
- 1055 Nolan, P. L., et al. 2012, *ApJS*, 199, 31
- 1056 Paneque, D., et al. 2013, *ArXiv* : 1304.4153
- 1057 Parent, D., et al. 2011, *ApJ*, 743, 170
- 1058 Pineault, S., Landecker, T. L., Madore, B., & Gaumont-Guay, S. 1993, *AJ*, 105, 1060
- 1059 Pletsch, H. J., et al. 2012, *ApJ*, 755, L20
- 1060 Ray, P. S., et al. 2011, *ApJS*, 194, 17
- 1061 Renaud, M., Goret, P., & Chaves, R. C. G. 2008, in *American Institute of Physics Con-*  
1062 *ference Series*, Vol. 1085, *American Institute of Physics Conference Series*, ed. F. A.  
1063 Aharonian, W. Hofmann, & F. Rieger, 281–284
- 1064 Roberts, M. S. E., Romani, R. W., & Johnston, S. 2001, *ApJ*, 561, L187
- 1065 Roberts, M. S. E., Romani, R. W., Johnston, S., & Green, A. J. 1999, *ApJ*, 515, 712
- 1066 Rousseau, R., et al. 2012, *A&A*, 544, A3
- 1067 Rowell, G., Horns, D., Fukui, Y., & Moriguchi, Y. 2008, in *American Institute of Physics*  
1068 *Conference Series*, Vol. 1085, *American Institute of Physics Conference Series*, ed.  
1069 F. A. Aharonian, W. Hofmann, & F. Rieger, 241–244
- 1070 Ruiz, M. T., & May, J. 1986, *ApJ*, 309, 667

- 1071 Ryter, C., Cesarsky, C. J., & Audouze, J. 1975, *ApJ*, 198, 103
- 1072 Safi-Harb, S., & Kumar, H. S. 2008, *ApJ*, 684, 532
- 1073 Sakai, M., Yajima, Y., & Matsumoto, H. 2011, *PASJ*, 63, 879
- 1074 Saz Parkinson, P. M., et al. 2010, *ApJ*, 725, 571
- 1075 Seward, F. D., Kearns, K. E., & Rhode, K. L. 1996, *ApJ*, 471, 887
- 1076 Sguera, V., et al. 2009, *ApJ*, 697, 1194
- 1077 Sheidaei, F. 2011, in *International Cosmic Ray Conference*, Vol. 7, *International Cosmic Ray*  
1078 *Conference*, 243
- 1079 Slane, P., et al. 2010, *ApJ*, 720, 266
- 1080 Spitkovsky, A. 2008, *ApJ*, 682, L5
- 1081 Sun, M., Wang, Z.-R., & Chen, Y. 1999, *ApJ*, 511, 274
- 1082 Tam, P. H. T., Wagner, S. J., Tibolla, O., & Chaves, R. C. G. 2010, *A&A*, 518, A8
- 1083 Tamura, K., Kawai, N., Yoshida, A., & Brinkmann, W. 1996, *PASJ*, 48, L33
- 1084 Temim, T., Slane, P., Gaensler, B. M., Hughes, J. P., & Van Der Swaluw, E. 2009, *ApJ*, 691,  
1085 895
- 1086 Terrier, R., et al. 2008, in *American Institute of Physics Conference Series*, Vol. 1085, *Amer-*  
1087 *ican Institute of Physics Conference Series*, ed. F. A. Aharonian, W. Hofmann, &  
1088 F. Rieger, 312–315
- 1089 Tibolla, O. 2011, in *International Cosmic Ray Conference*, Vol. 6, *International Cosmic Ray*  
1090 *Conference*
- 1091 Tibolla, O., Komin, N., Kosack, K., & Naumann-Godo, M. 2008, in *American Institute of*  
1092 *Physics Conference Series*, Vol. 1085, *American Institute of Physics Conference Series*,  
1093 ed. F. A. Aharonian, W. Hofmann, & F. Rieger, 249–252
- 1094 Tibolla, O., et al. 2012, in *American Institute of Physics Conference Series*, Vol. 1505,  
1095 *American Institute of Physics Conference Series*, ed. F. A. Aharonian, W. Hofmann,  
1096 & F. M. Rieger, 349–353
- 1097 Trimble, V. 1973, *PASP*, 85, 579

- 1098 Uchiyama, Y. 2011, ArXiv:1104.1197
- 1099 Van Etten, A., & Romani, R. W. 2010, ApJ, 711, 1168
- 1100 Verbiest, J. P. W., Weisberg, J. M., Chael, A. A., Lee, K. J., & Lorimer, D. R. 2012, ApJ,  
1101 755, 39
- 1102 Weekes, T. C., et al. 2002, Astroparticle Physics, 17, 221
- 1103 Weinstein, A. 2009, ArXiv:0912.4492
- 1104 Weltevrede, P., et al. 2010, ApJ, 708, 1426
- 1105 Wilks, S. 1938, Annals of Mathematical Statistics, 9, 60
- 1106 Wu, J. H. K., et al. 2011, ApJ, 740, L12
- 1107 Yadigaroglu, I.-A., & Romani, R. W. 1997, ApJ, 476, 347